

DOI: 10.1002/ ((please add manuscript number))

Article type: REVIEW

Recent Advances and Opportunities of Eco-Friendly Ternary Copper Halides: A New Superstar in Optoelectronic Applications

Zhuangzhuang Ma, Xinzhen Ji, Shuailing Lin, Xu Chen, Di Wu, Xinjian Li, Yu Zhang, Chongxin Shan, Zhifeng Shi*, and Xiaosheng Fang*

Dr. Z. Z. Ma, Dr. X. Z. Ji, Dr. S. L. Lin, Dr. X. Chen, Dr. D. Wu, Prof. X. J. Li, Prof. C. X. Shan and Prof. Z. F. Shi

Key Laboratory of Materials Physics of Ministry of Education

School of Physics and Microelectronics

Zhengzhou University

Daxue Road 75, Zhengzhou 450052, P. R. China

E-mail: shizf@zzu.edu.cn

Prof. X. S. Fang

Department of Materials Science, Institute of Optoelectronics, State Key Laboratory of Molecular Engineering of Polymers

Fudan University

Shanghai 200438, P. R. China

E-mail: xshfang@fudan.edu.cn (X. S. Fang)

This article has been accepted for publication and undergone full peer review but has not been through the copyediting, typesetting, pagination and proofreading process, which may lead to differences between this version and the [Version of Record](https://onlinelibrary.wiley.com/doi/10.1002/adma.202300731). Please cite this article as [doi: 10.1002/adma.202300731](https://doi.org/10.1002/adma.202300731).

This article is protected by copyright. All rights reserved.

Accepted Article

Prof. Y. Zhang

State Key Laboratory on Integrated Optoelectronics

College of Electronic Science and Engineering

Jilin University

Changchun 130012, P. R. China

Abstract

Recently, the newly-emerging lead-free metal-halide materials with less toxicity and superior optoelectronic properties have received wide attention as the safer and potentially more robust alternatives to lead-based perovskite counterparts. Among them, ternary copper halides (TCHs) have become a vital group due to their unique features, including abundant structural diversity, ease of synthesis, unprecedented optoelectronic properties, high abundance, and low cost. Although the recent efforts in this field have made certain progresses, some scientific and technological issues still remain unresolved. Herein, a comprehensive and up-to-date overview of recent progress on the fundamental characteristics of TCH materials and their versatile applications is presented, which contains topics such as: i) crystal and electronic structure features and synthesis strategies; ii) mechanisms of self-trapped excitons, luminescence regulation, and environmental stability; and iii) their burgeoning optoelectronic devices of phosphor-converted white light-emitting diodes (WLEDs), electroluminescent LEDs, anti-counterfeiting, X-ray scintillators, photodetectors, sensors, and memristors. Finally, the current challenges together with future perspectives on the development of TCH materials and applications are also critically described, which is considered to be critical for accelerating the commercialization of these rapidly evolving technologies.

Keywords: ternary copper halides, lead-free perovskites, optoelectronic properties, stability

This article is protected by copyright. All rights reserved.

1. Introduction

Lead-halide perovskites entered into momentous prominence in 2009 when their unprecedented optoelectronic characteristics were exploited.^[1–3] Primitively employed as absorbers in photovoltaic devices, they were demonstrated to own excellent charge carrier transport capacities, which sprung them into a mass of solar cell fields.^[4–7] After about a decade of research and development, the peak certified power conversion efficiency of single-cell perovskite photovoltaic device has exceeded 25%, which is comparable with commercial crystalline silicon-based solar cells.^[8] In addition, even much more conspicuous developments for light-emitting diodes (LEDs) composed of perovskite emitting layers are observed.^[9–16] Since the first demonstration of perovskite LEDs by Friend's group in 2014,^[13] the external quantum efficiency (EQE) of perovskite LEDs raised rapidly from an initial value of 0.1% to over 28% in 2022.^[17] The reason for such remarkable device performances can be ascribed to the exceptional optoelectronic properties of perovskites, including excellent light absorption coefficients, suitable and tunable bandgap, narrow emission linewidths, long carrier diffusion length, and balanced electron and hole mobilities.^[18–22] In addition, with the increasing recognition of material properties and device working mechanisms, perovskites are also demonstrated to be promising candidates for other optoelectronic devices, including photodetectors, X-ray imaging, sensors, and memristors.^[23–25]

Despite the impressive progresses and prosperous potencies of lead-based perovskites, the lead (Pb) toxicity and intrinsic instability may be obstacles for practical commercial application.^[25–28] Pb and its compounds are known to be alarming harmful substances that accumulate in living organisms and are defined as a carcinogen that can cause many health diseases in all ages even when exposed to the minimal doses.^[29] Due to the lack of a general consensus of allowed Pb contents for consumers and universally distasteful public opinion, it is necessary to gradually replace Pb with other relatively harmless elements.^[30] Moreover, the commercial deployment of perovskite optoelectronic devices is hampered by their instability to ambient humidity, oxygen, thermal, and light irradiation.^[31–34] Hence, exploring lead-free halide perovskites without sacrificing optoelectronic characteristics and excellent stability are urgently needed and certainly a worthwhile subject. Early efforts were made to replace toxic Pb by Sn and Ge with similar electronic configuration. However, the resulting Sn- and Ge-halide perovskites usually suffer from unsatisfactory stability due to the fast oxidation of Sn²⁺ and Ge²⁺ to +4 valent state under ambient conditions.^[35–37] Lately, trivalent Bi³⁺ and Sb³⁺ were also studied, but the photoluminescence quantum yield (PLQY) of the as-prepared A₃Bi₂X₉ and A₃Sb₂X₉ (A = Cs,

This article is protected by copyright. All rights reserved.

CH_3NH_3 (MA), or NH_2CHNH_2 (FA); $\text{X} = \text{Cl, Br, I}$) was much lower than that of lead-halide counterparts.^[25] Most recently, ternary copper halides (TCHs) are flourishing as a fascinating substitute to lead-halide perovskites because of their several intrinsic traits: (i) abundant resources in nature, (ii) superior environmental stability, (iii) abundant structural diversity, (iv) excellent optoelectronic properties, and (v) high luminescent efficiencies comparable with those of most lead-halide perovskites.^[38–42] Although no longer strictly “perovskite”, copper halide and cesium halide hold a number of similar features to the perovskite family, and this field is usually taken as derived from the general field of perovskites.^[26] Excitingly, some of the resulting TCH materials have made sensational breakthroughs in the manufacture of optoelectronic devices.^[43–45] However, a systematic overview on TCH materials, focusing on their fundamental properties, optoelectronic applications, and potential limitations, has not yet been fully presented.

In this review, we aim to deliver a comprehensive description of the properties and device applications of TCH materials, as schematically shown in **Figure 1**. We start with the general introduction of TCH materials in relation to their crystal and electronic structures, and the synthesis strategies. Then, we discuss the PL mechanisms of self-trapped excitons (STEs) related emission in TCH materials and the emission regulation under various physical or chemical effects, as well as their environmental stability issues. Further, we summarized the recent progresses of their optoelectronic devices, including phosphor-converted WLEDs, electroluminescent LEDs, anti-counterfeiting, X-ray scintillators, photodetectors, sensors, and memristors. In the last part, we outline the main challenges and development prospects currently faced by TCHs for further advancing sustainable research in this field.

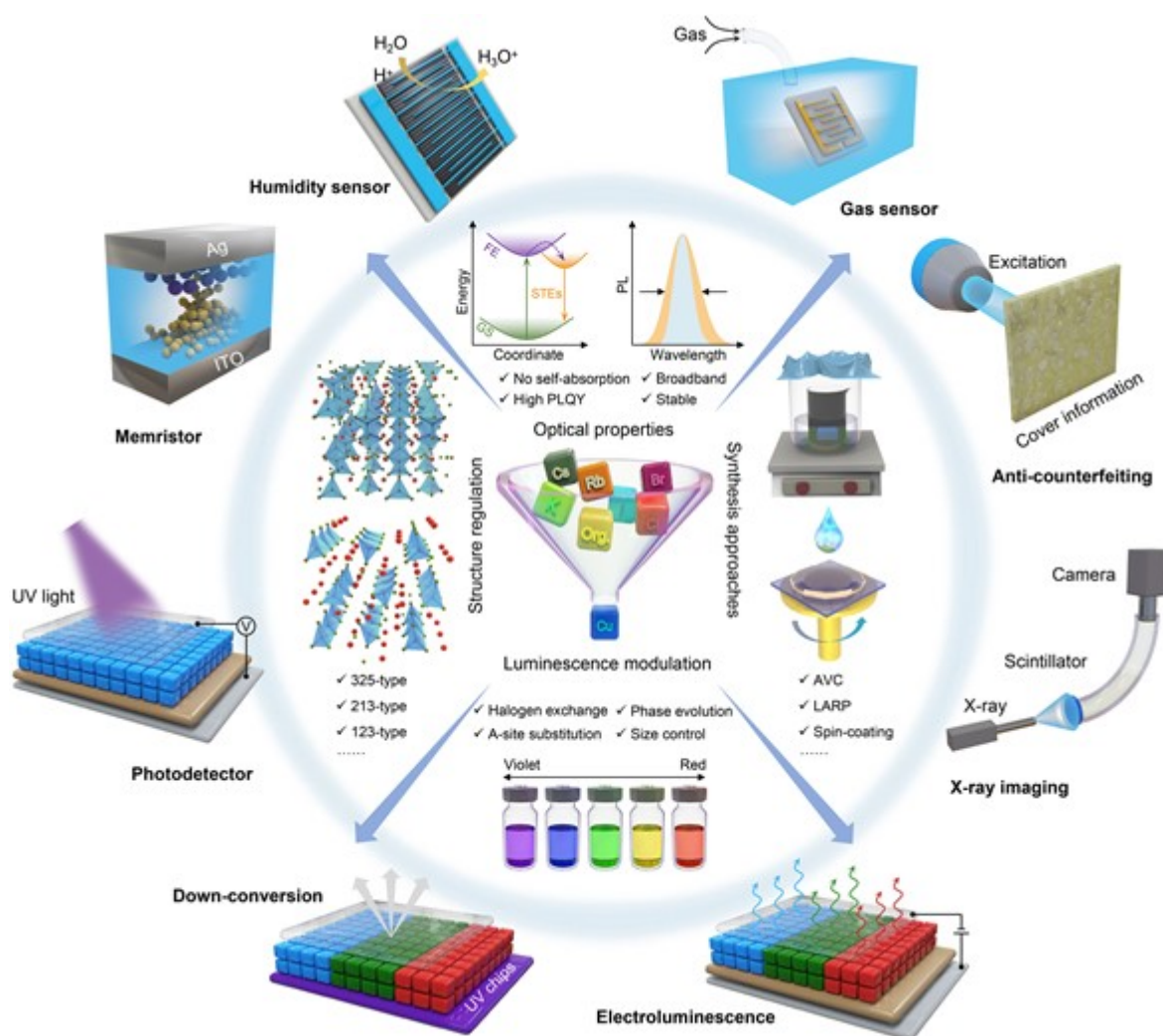


Figure 1. Summary diagram of the review, including structure, synthesis, properties, and optoelectronics applications of TCH materials.

2. Structural Diversity of TCHs

In the development of TCHs, the crystal structure cognition based on chemical composition is considered to be fundamental to understand the inherent structural characteristics of materials.^[23] The abundant structural diversity of TCHs is the result of the possible various ratios of copper and halide elements, as well as the possible multiple coordination modes between them, and a variety of available inorganic and organic modules of the A-site.^[26] Moreover, the diverse compositional combinations and various connection types between the adjacent Cu halide polyhedrons provide a large degree of variation with complete isolation and face-, corner-, and edge-sharing.^[27] The

This article is protected by copyright. All rights reserved.

combination of multiple possibilities results in a large dimensional modulation (2D, 1D and 0D) of such materials in crystal structure with adjustable electronic properties.^[24] In this section, the versatile crystal and electronic structural properties of TCH materials will be introduced, including all-inorganic and organic-inorganic hybrid systems.

2.1. Crystal Structure

2.1.1. All-Inorganic System

We began to turn our attention to the crystal structure of all-inorganic $A_3Cu_2X_5$ ($A = Rb, Cs; X = Cl, Br, I$). The basic unit of $A_3Cu_2X_5$ is a $[Cu_2X_5]^{3-}$ dimer, which constitutes a $[CuI_4]^{3-}$ tetrahedra and an edge-connecting $[CuI_3]^{2-}$ triangle (**Figure 2a**). Each $[Cu_2X_5]^{3-}$ dimer is characterized by the separation of A^+ ions, thus resulting in a 0D crystal structure with the orthorhombic system (space group, *Pnma*).^[46] Experimentally, Hosono et al. elucidated the crystal structure of $Cs_3Cu_2I_5$ single crystal,^[38] which was well verified by single-crystal X-ray diffraction results. For 1D TCH, the ACu_2X_3 -type structure can crystallized the orthorhombic space group of *Cmcm*,^[46] in which two spatially-oriented $[CuI_4]^{3-}$ tetrahedra units are alternately connected to form an infinite unit chain of composition of $[Cu_2I_6]^{4-}$ separated by A^+ ions (Figure 2b).^[47–50] Bolink et al. proved that the continuous movement of the Bragg's reflection peak is linearly related to the halogen compositions, thereby confirming the formation of highly purified compounds. The unit cell volumes obtained by Le Bail fitting exhibit a linear extension from 633 Å³ (Cl) to 840 Å³ (I), following Vegard's law, which is attributed to an increase in ionic radius from Cl^- to I^- .^[51] Compared with the ACu_2X_3 type with a wide 1D chain by two Cu^+ ions, the A_2CuX_3 phase with *Pnma* symmetry also possesses the 1D structure with only one Cu^+ ion by sharing a vertex,^[52–55] as presented in Figure 2c. Moreover, Hosono and co-workers recently discovered a novel 1D "538" type $Cs_5Cu_3Cl_6I_2$ based on a mixed-halide strategy, which turns to be another alternative to obtain 1D Cu-based halides.^[56] The $Cs_5Cu_3Cl_6I_2$ appertains to the orthorhombic system with space group of *Cmcm*, consisting of 1D $[Cu_3Cl_6I_2]_n^{5n-}$ chains and charge-balanced Cs^+ ions (Figure 2d). Note that the 1D zigzag chain of $[Cu_3Cl_6I_2]_n^{5n-}$ is composed of a single $[CuCl_2I_2]^{3-}$ unit and an alternately connected $[CuCl_2I_2]_2^{6-}$ unit, in which only I^- ions are served to bridge these units. Meanwhile, the 1D zigzag structure of "538" phase occurs only in the Cl–I mixtures, while only the solid solution of the *Pnma* space group was observed for the Cl–Br and Br–I mixtures, which may be related to the large discrepancy in ionic radius and electronegativity between the Cl^- and I^- anions.^[57–59] Because all the above TCHs have univalent Cu^+ ion on the B site, their

This article is protected by copyright. All rights reserved.

highest coordination number is four, which is caused by the small ion radius and high $3d^{10}$ energy level of Cu.

The TCHs with divalent Cu^{2+} ion on the B site also contain rich phase groups, such as 214- and 113-type,^[60,61] mostly composed of extended $[\text{Cu-X}]$ octahedron caused by the Jahn-Teller distortions. The Cs_2CuX_4 adopts the orthorhombic phase with space group of *Pnma* (Figure 2e), while $\text{Cs}_2\text{CuCl}_3\text{Br}$ owns a tetragonal crystal system, which is attributed to the distortion of $[\text{CuCl}_6]^{4-}$ octahedrons caused by the incorporation of Br atoms.^[60] Figure 2f shows the crystal structure of CsCuX_3 compounds, in which Cu^{2+} coordinates with six X^- to form $[\text{Cu-X}]$ octahedrons connected by corner and face sharing, constituting spatially isolated 1D coplaner chains and 3D networks through vertex-sharing.^[61] Due to the large number of components of alkali copper halides, further study of the relationship between the chemical composition and structural characteristic of the compounds is of great significance for the better understanding of these materials.

2.1.2. Organic-Inorganic Hybrid System

Except for all-inorganic systems, the use of organic ligands at the A site usually produces 0D molecular structures, characterized by the fact that the copper-halide polyhedrons are entirely surrounded or separated by organic cations, forming highly ordered periodical structures.^[62–67] In a sense, they can be viewed as core-shell structures, with the negatively charged polyhedrons as the core and organic-inorganic composite cations as the shell.^[68–70] For instance, Liu's group reported the organic-inorganic hybrid MA_2CuCl_3 ($\text{MA} = \text{CH}_3\text{NH}_3$), which crystallizes in the monoclinic phase with *P2₁/n* space group and characterizes a 0D structure.^[71] In such structure, each $[\text{Cu}_2\text{Cl}_6]^{4-}$ dimer is spatially isolated by large bandgap organic framework of MA^+ , and the corresponding crystal structure diagram is displayed in Figure 2g. By introducing the primary amine (PEA, phenylethylamine) into the structure of copper iodine complexes, Wang et al. explored a new 0D organic-inorganic hybrid TCH with a general formula of $\text{PEA}_4\text{Cu}_4\text{I}_4$.^[66] As can be seen from the crystal structure in Figure 2h, this compound belongs to a monoclinic system with a space group of *P2₁/c*, and the crystallographic units consist of four PEA ligands, four Cu ions, and four iodide ions. In the $[\text{Cu}_4\text{I}_4]^{4-}$ units, each Cu^+ ion is coordinated with three I^- anions and the PEA ligand points out of the $[\text{Cu}_4\text{I}_4]^{4-}$ unit via the Cu–N bond, while each I^- anion links three adjacent Cu^+ ions. The average distances of Cu–Cu are in the range of 2.630–2.704 Å, significantly lower than the total of van der Waals radii (2.80 Å), indicating that the shortening of Cu–Cu distance may be caused by the pressing of the large I^- anion. Subsequently, Fang et al. chose three various PEAs with the similar chemical

This article is protected by copyright. All rights reserved.

formula (PEA, (R)-(+)- α -PEA, (S)-(-)- α -PEA, and β -PEA) to synthesize a series of organic-inorganic hybrid TCHs with 0D structures.^[62] The resulting ((R)-(+)- α -PEA)₄Cu₄I₄ and ((S)-(-)- α -PEA)₄Cu₄I₄ belong to the orthorhombic space group of $P2_12_12_1$, since (R)-(+)- α -PEA and (S)-(-)- α -PEA are only difference in chirality, while (β -PEA)₄Cu₄I₄ owns a monoclinic structure with a space group of Cc . Figure 2i presents the crystal structure of (PTMA)₃Cu₃I₆ (PTMA, phenyltrimethylammonium), where each edge- and face-sharing [Cu₃I₆]³⁻ units are completely separated by PTMA⁺ anions, resulting in a highly-ordered 0D structure.^[72] In addition to the above mentioned materials, organic-inorganic hybrid TCH systems containing other types of derivatives, such as TEA₂Cu₂Br₄ (TEA, tetraethylammonium), (TBA)CuX₂ (TBA, tetrabutylammonium cation; X = Cl, Br), (DTA)₂Cu₂I₄ (DTA, dodecyl trimethyl ammonium), (Gua)₃Cu₂I₅ (Gua, guanidine), [(C₃H₇)₄N]₂Cu₂I₄ ((C₃H₇)₄N, tetrapropylammonium), [KC₂]₂[Cu₄I₆] (C = 12-crown-4 ether), (C₁₆H₃₆N)CuI₂, and (C₄H₉)₄NCuCl₂, have been discovered.^[63,64,68,69,73,74] The rich selection of organic cations with different sizes, shapes and electronic properties could produce remarkable structural diversity and offer flexibility for the adjustment of various chemical components, which provide more possibilities for the discovery and design of new TCH structures.^[75–78]

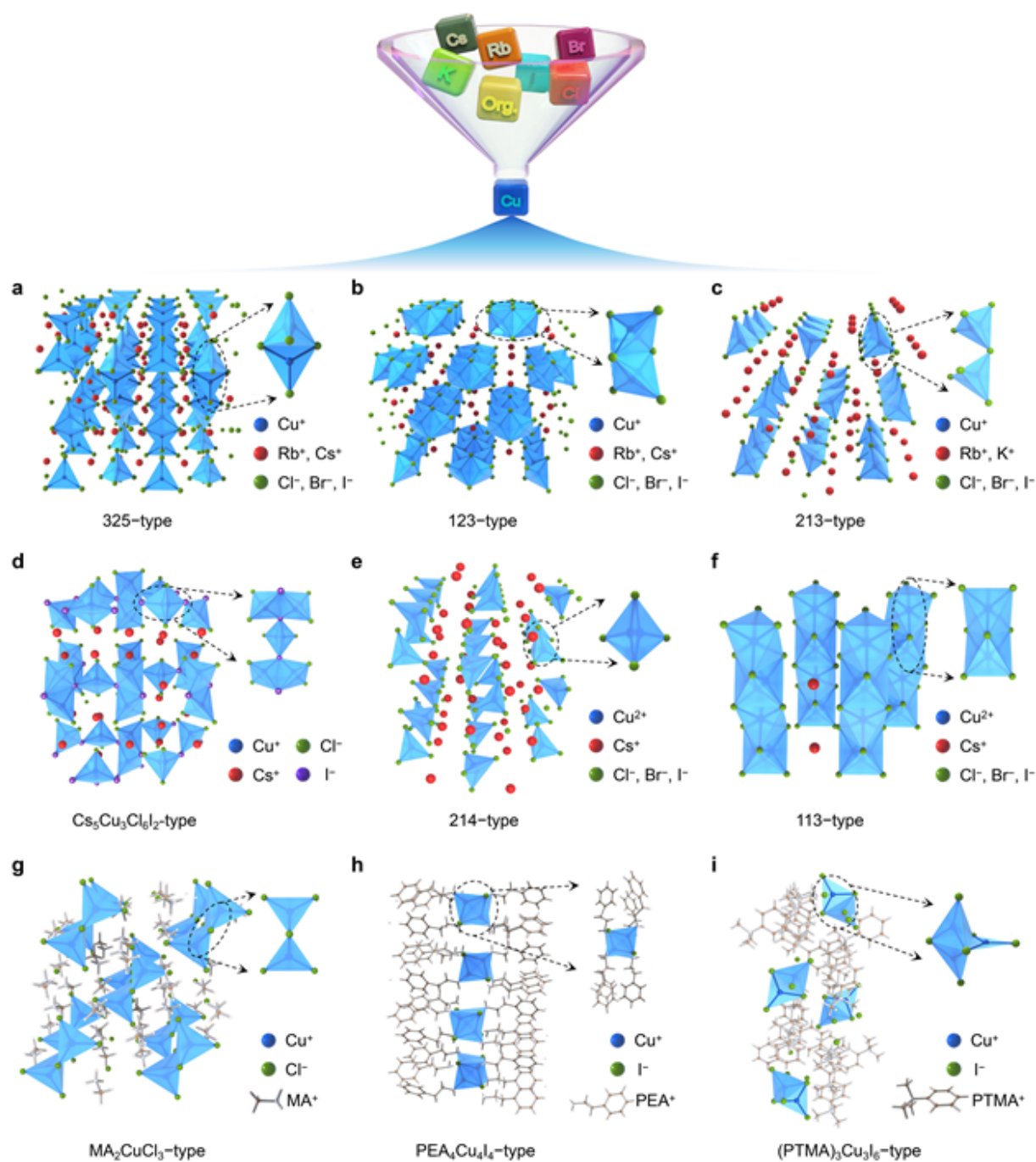


Figure 2. Schematic illustration of crystal structures of the representative TCHs, including all-inorganic and organic-inorganic hybrid systems. a) $A_3Cu_2X_5$ type ($A = Rb, Cs$; $X = Cl, Br, I$). b) ACu_2X_3 type. c) A_2CuX_3 type. d) $Cs_5Cu_3Cl_6I_2$ type. e) A_2CuX_4 type. f) $ACuX_3$ type. g) MA_2CuCl_3

This article is protected by copyright. All rights reserved.

type (MA = CH₃NH₃). h) PEA₄Cu₄I₄ type (PEA = C₆H₅CH₂CH₂NH₃). i) (PTMA)₃Cu₃I₆ type (PTMA = C₁₂H₂₀N).

2.2. Electronic Band Structure

Electronic band structure plays an important role for TCHs to index their optoelectronic properties and potential applications.^[79–81] At present, the band structure, projected density state density (PDOS), defect tolerance, and many other electronic properties of TCHs have been studied with a great deal of work.^[82–87] For instance, Xing and colleagues studied the PDOS and electronic charge density of Cs₃Cu₂I₅ and CsCu₂I₃ based on density functional theory (DFT) calculations.^[85] They found that both CsCu₂I₃ and Cs₃Cu₂I₅ have a direct bandgap at the Γ point, with the calculated bandgap values of 2.88 and 3.07 eV, respectively. Moreover, both valence band maximum (VBM) and conduction band minimum (CBM) of CsCu₂I₃ and Cs₃Cu₂I₅ are originated from the mixed Cu *3d* and I *5p* orbitals (Figure 3a,b). However, Cs⁺ ions do not contribute to VBM or CBM, as evidenced by the isosurface plots of wave function $|\Psi|^2$ of VBM and CBM. Notably, the VBM of Cs₃Cu₂I₅ is flatter than that of CsCu₂I₃, signifying larger hole effective masses as well as stronger quantum confinement, thereby resulting in more difficulty for excitons to dissociate and diffuse in the crystal lattice.^[85] In the electronic band structures, the curvature of bands is related to electron and hole effective masses that directly affect the carrier mobility. Our group demonstrated that the Cu *s*-contributed conduction band curvature of CsCu₂I₃ is slightly dispersive than the Cu *d*-derived valence band, which produces comparable effective masses of electron (0.22 m_0 along the $\Gamma \rightarrow S$ direction) and hole (0.55 m_0 along the $\Gamma \rightarrow S$ direction).^[88] Such comparable low carrier effective mass implies rapid exciton diffusion or carrier transport along the 1D pathway of CsCu₂I₃. We calculated the 3D electron density difference in the *a*–*b* plane of CsCu₂I₃,^[89] revealing that the accumulations and depletions of electrons are mainly on the Cu–I bonds, which indicates a 1D electronic structure distribution. According to the electron localization function calculated from different perspectives, the electron density of {110} crystal plane is larger than that of {010}, which explains the large dark current of {110} crystal plane observed experimentally. Further, they reasonably verified that the photoexcited electron is localized in the 1D chains created by [CuI₄]³⁻ polyhedrons, resulting in the rapid charge mobility along the [001] direction.

Recently, Tang et al. reported the band structures of Rb₂CuBr₃ that shows Cu *3d*- and Br *4p*-contributed VBM, and the Cu *4s*-, Br *4p*-, and Br *4s*-derived CBM, both of which have no relation with Rb⁺ ions (Figure 3c,d).^[90] Due to the inherent low-dimensional electronic structures caused by

This article is protected by copyright. All rights reserved.

1D crystal structure, Rb_2CuBr_3 shows much flatter band dispersion (especially for VBM) than that of 3D materials (e.g., CsPbBr_3). This property would allow the generated excitons in Rb_2CuBr_3 strongly confined to each $[\text{CuBr}_4]_n^{3n+}$ ribbon, which results in a large exciton binding energy and enables a high luminescent efficiency under photoexcitation. Similar to Rb_2CuBr_3 and other alkali copper halides, $\text{Cs}_5\text{Cu}_3\text{Cl}_6\text{I}_2$ features the VBM consisted of Cu $3d$ and halide p orbitals and CBM consisted of Cu $4s$ and halide p orbitals (Figure 3e,f), as reported by Hosono et al.^[56] The symmetry study of the electronic wave function certified that CBM and VBM at the Γ point are of s and p symmetries, respectively, reflecting an allowable electron transition at the Γ point. According to the band structure, the valence band of $\text{Cs}_5\text{Cu}_3\text{Cl}_6\text{I}_2$ is rather flat, different from the dispersive energy band structure of CuCl and CuI , which is attributed to the low-dimensional electronic dimensionality of $\text{Cs}_5\text{Cu}_3\text{Cl}_6\text{I}_2$. The relatively long Cu–I bond length (2.749Å) compared to the 2.641Å in CuI further reduces the overlaps of electronic wave function, leading to the large hole effective masses. Thus, photoexcited holes could be fleetly localized and immobilized by interacting with the lattice at the iodide anion position.^[56]

Compared with the all-inorganic TCHs, organic-inorganic hybrid systems face more complex electronic structures because organic cations could directly or indirectly affect the electronic band.^[91–94] For instance, Zhang et al. elaborated the band structure and PDOS of a novel organic-inorganic $(\text{C}_{16}\text{H}_{36}\text{N})\text{CuI}_2$ by the DFT calculations.^[64] They revealed that the VBM is contributed by the hybridization between I $5p$ and Cu $3d$ orbitals, while the CBM is mainly constructed by the $\text{C}_{16}\text{H}_{36}\text{N}^+$ organic component, resulting in a direct bandgap of 3.25 eV at the Γ point. Besides, the conduction band is more dispersed than the valence band, thus the holes are mainly located on the $[\text{Cu}_2\text{I}_4]^{2-}$ dimer, and the electrons are more delocalized, which slows the rate of electron-hole recombination and leads to a long exciton lifetime. Zou et al. demonstrated that the organic cation of $[(\text{C}_3\text{H}_7)_4\text{N}]^+$ plays an important role in $[(\text{C}_3\text{H}_7)_4\text{N}]_2\text{Cu}_2\text{I}_4$, which could be regarded as a confining agent that promotes the formation of excitons with varied charges.^[68] Different from the direct bandgap of TCHs discussed above, $(\text{C}_8\text{H}_{24}\text{N}_4)\text{Cu}_2\text{Cl}_6 \cdot 4\text{H}_2\text{O}$ is characterized by the existence of indirect and direct bandgap; but due to the participation of phonons to guarantee the conservation of momentum, the VBM of the indirect and direct gaps are quite near and the indirect transition probability is small.^[93] Specifically, the difference between the Y point (indirect gap: $Y \rightarrow \Gamma$) and Γ point (direct gap: $\Gamma \rightarrow \Gamma$) is only 9.5 meV in VBM and the PDOS around Γ and Y is close, thus the direct transition is dominant in this

structure. Moreover, the VBM appears flat because the $[\text{Cu}_2\text{Cl}_6]^{4-}$ dimers are isolated by large organic cations, which manifests strong hole localization and large hole effective mass.

Any deviation from the periodic lattice will lead to a crystal imperfection, that is, defect, which may form a localized electronic state (defect energy level).^[95–100] In most cases, defects are regarded as an adverse effect, usually trapping charge carriers in the bandgap region and limiting their mobility, with serious repercussion on the photoelectric properties of materials.^[101–107] Therefore, studying the role of defects, especially for inherent point defects, is crucial. In 2022, Yin et al. comprehensively calculated the defect formation energies along with transition energy levels of all possible intrinsic point defects in $\text{Cs}_3\text{Cu}_2\text{I}_5$,^[79] including 11 antisite substitutions (Cs_{I1} , Cs_{I2} , Cs_{I3} , Cs_{I4} , Cu_{I1} , Cu_{I2} , Cu_{I3} , Cu_{I4} , I_{Cs1} , I_{Cs2} , and I_{Cu}), seven vacancies (V_{Cs1} , V_{Cs2} , V_{Cu} , V_{I1} , V_{I2} , V_{I3} , and V_{I4}), three cation substitutions (Cu_{Cs1} , Cs_{Cu} , and Cu_{Cs2}), and three interstitials (Cs_i , Cu_i , and I_i). They pointed out that the dominant defects, such as Cu_{Cs1} , Cu_{Cs2} , V_{Cs1} , V_{Cs2} , V_{Cu} , I_{Cs1} , I_{Cs2} , and I_{Cu} , possess low formation energies, regardless of whether they were in Cu-poor or Cu-rich condition, as shown in Figure 3g. The transition levels of the defect represent the defect tolerance; in other words, the deeper the transition levels, the lower the defect tolerance. Figure 3h,i present the calculated transition energy levels of the dominant point defects in $\text{Cs}_3\text{Cu}_2\text{I}_5$, indicating that the above point defects are all shallow with transition energies less than 0.1 eV above the VBM. In short, these researches suggest that $\text{Cs}_3\text{Cu}_2\text{I}_5$ possesses a unique defect-tolerant property, which can broaden the path of radiative recombination and thermal relaxation, explaining the high-efficiency luminescence properties of $\text{Cs}_3\text{Cu}_2\text{I}_5$. Lately, Huang et al. demonstrated that the formation energy of V_{I} is smaller than that of V_{Cs} and V_{Cu} in CsCu_2I_3 , confirming that the V_{I} is the most likely vacancy defect.^[84] The results of PDOS indicate that there is an obvious defect state located in the bandgap of V_{I} , which is significantly different from V_{Cs} and V_{Cu} . Thus, V_{I} is possibly the origin of the trap state, explaining the abnormal emission spectrum experimentally observed in CsCu_2I_3 . Based on the above discussion, one can observe that the essential electronic band structures of TCHs have been clarified via DFT calculations. However, in the previous studies, the calculation of internal electronic dimensionality, defect distribution, bandgap type, and exciton behaviors still remain undetailed, which naturally prompts further research on the electronic structure of TCHs in the future.

This article is protected by copyright. All rights reserved.

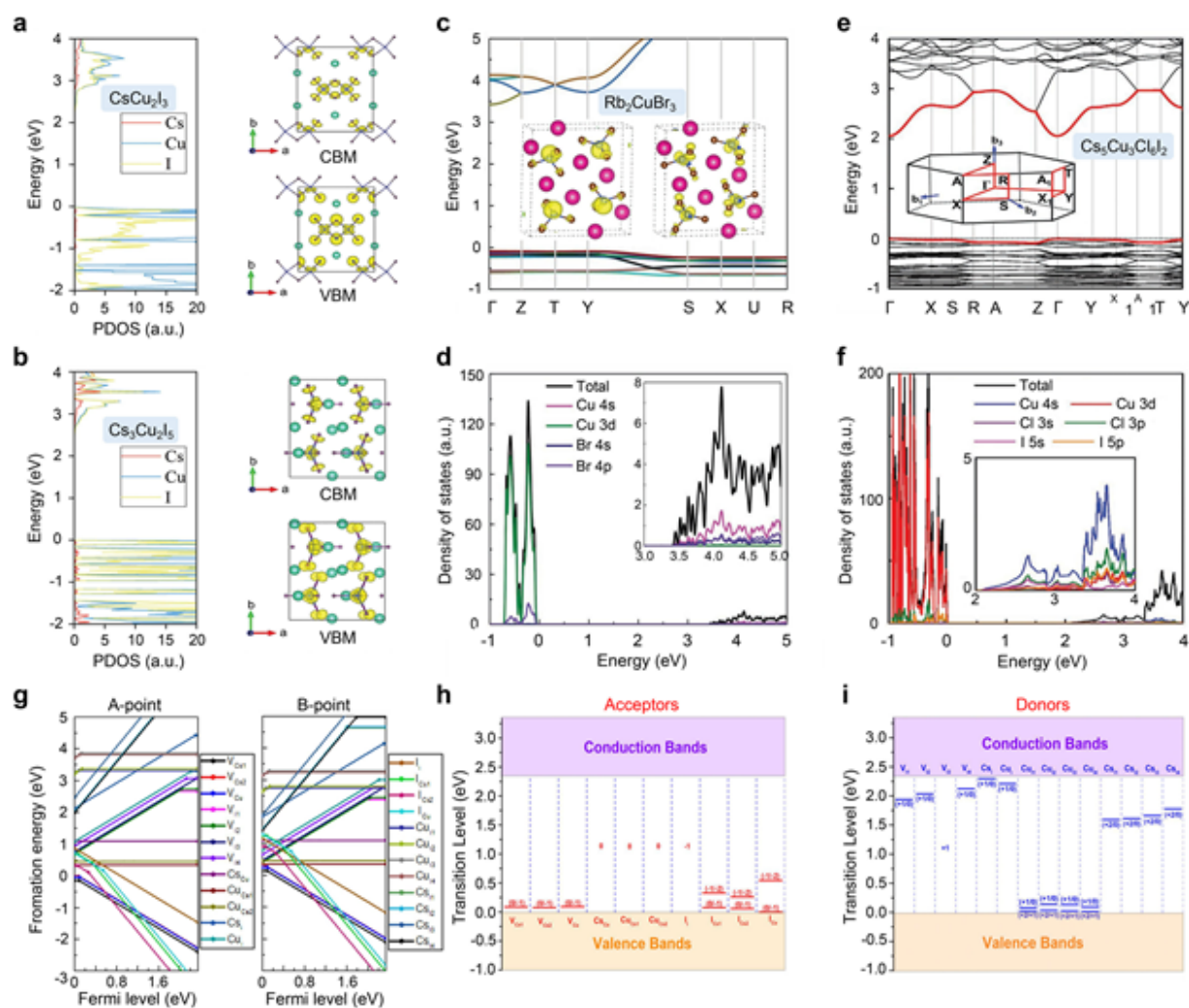


Figure 3. Electronic band structure of TCHs. PDOS and electronic charge density for the CBM and VBM of CsCu₂I₃ (a) and Cs₃Cu₂I₅ (b). (a,b) Reproduced with permission.^[85] Copyright 2022, Wiley-VCH. c) Calculated electronic band structure and d) PDOS of Rb₂CuBr₃. The insets in (c) show the CBM and VBM of Rb₂CuBr₃. (c,d) Reproduced with permission.^[90] Copyright 2019, Wiley-VCH. e) Calculated electronic band structure and f) PDOS of Cs₅Cu₃Cl₆I₂. (e,f) Reproduced with permission.^[56] Copyright 2020, Wiley-VCH. g) Calculated formation energies of the intrinsic point defects in Cs₃Cu₂I₅. Calculated transition energy levels of (h) acceptors and (i) donors in Cs₃Cu₂I₅. (g-i) Reproduced with permission.^[79] Copyright 2022, American Chemical Society.

3. Synthesis Approaches of TCHs

This article is protected by copyright. All rights reserved.

TCH materials have received much attention because of the low-cost, abundance and nontoxicity of copper-related raw material, and wide range of material types, including single crystals (SCs), nanocrystals (NCs), microcrystal, and films, which offer great potential for a variety of optoelectronic applications.^[108–118] In this section, we comprehensively summarize and discuss their synthesis methods and growth processes, and the illustration of main synthesis techniques is shown in **Figure 4**.

3.1. Synthesis of TCH SCs

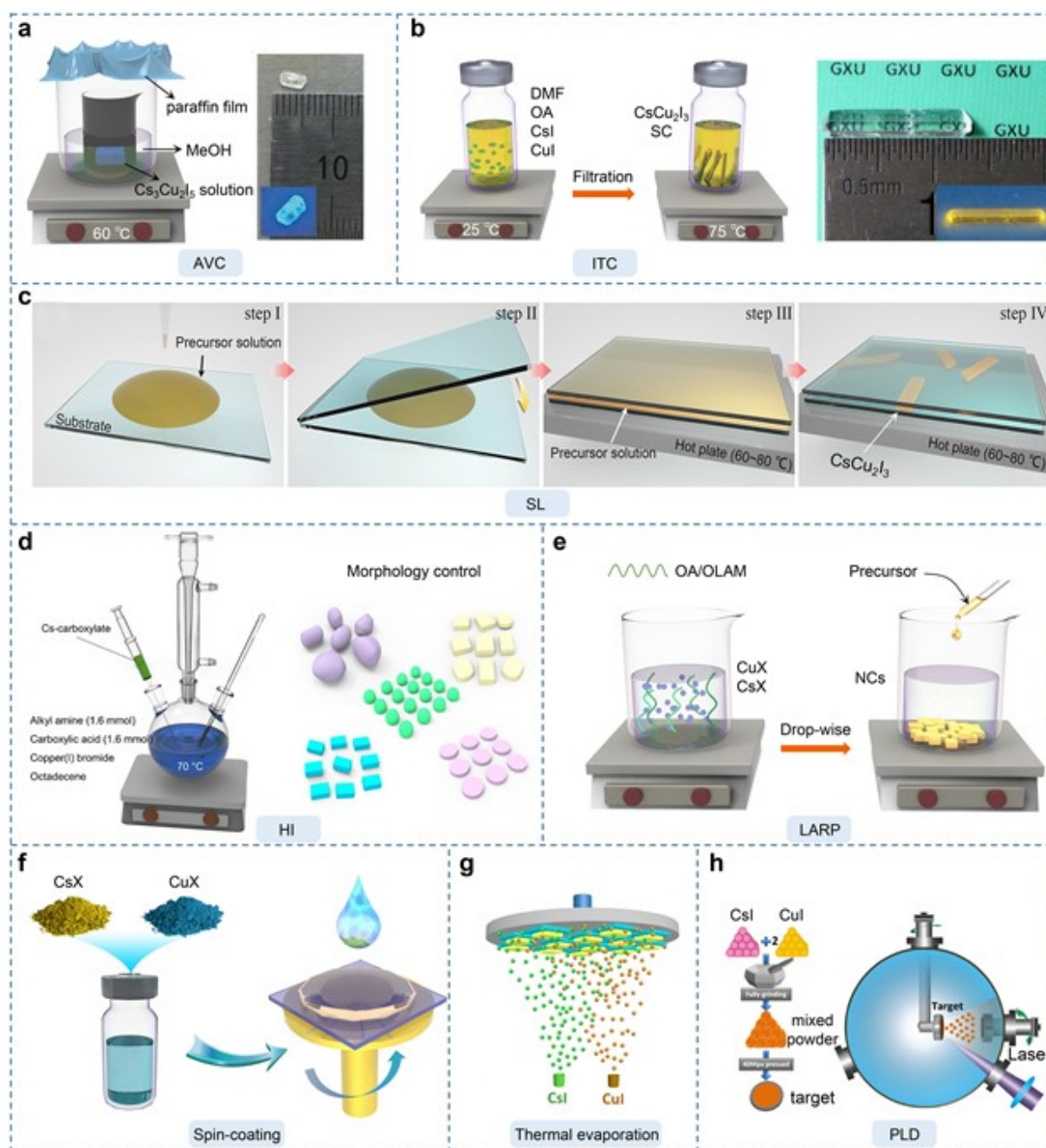


Figure 4. Synthetic diagrams of TCHs. a) Antisolvent vapor-assisted crystallization (AVC) for the synthesis of $\text{Cs}_3\text{Cu}_2\text{I}_5$ SCs. The right pane is a photograph of $\text{Cs}_3\text{Cu}_2\text{I}_5$ SC under ambient light and 254 nm UV light irradiation. (a) Reproduced with permission.^[38] Copyright 2018, Wiley-VCH. b) Inverse temperature crystallization (ITC) for the synthesis of CsCu_2I_3 SCs. The right pane is a photograph of CsCu_2I_3 SC under sun light and 365 nm UV light irradiation. (b) Reproduced with permission.^[126]

This article is protected by copyright. All rights reserved.

Copyright 2021, Elsevier. c) Space-limited (SL) growth for the synthesis of CsCu_2I_3 SCTF. (c) Reproduced with permission.^[107] Copyright 2021, American Chemical Society. d) Hot-injection (HI) approach for the synthesis of $\text{Cs}_3\text{Cu}_2\text{X}_5$ NCs. (d) Reproduced with permission.^[105] Copyright 2021, American Chemical Society. e) Ligand-assisted reprecipitation (LARP) approach for the preparation of $\text{Cs}_3\text{Cu}_2\text{X}_5$ NCs. f) Spin-coating approach for the preparation of CsCu_2I_3 films. g) Thermal evaporation approach for the preparation of $\text{Cs}_3\text{Cu}_2\text{I}_5$ films. (g) Reproduced with permission.^[164] Copyright 2022, American Chemical Society. h) Pulsed-laser deposition (PLD) for the synthesis of CsCu_2I_3 films. (h) Reproduced with permission.^[170] Copyright 2022, Elsevier.

3.1.1. Antisolvent Vapor-Assisted Crystallization

TCH SCs have the advantages of long carrier lifetime, low defect density, and high carrier mobility, which is conducive to the achievement of high-performance optoelectronic devices.^[119–127] Up to now, TCH SCs have been successfully synthesized by using various methods. Antisolvent vapor-assisted crystallization (AVC) approach is based on the various solubility of raw materials in different solvents to synthesis SCs.^[127] In AVC technique, the crystal growth mechanism depends on a sharp decrease in the solubility of the required products and final precipitation. The effectiveness of such method relies on several key parameters, such as nature of antisolvent, solvent and antisolvent volume ratios, and antisolvent diffusion time and rate.^[81] In 2018, Hosono et al. initiatively presented the synthesis of $\text{Cs}_3\text{Cu}_2\text{I}_5$ SCs via the AVC method.^[38] First, the mixtures of CsI and CuI with a molar ratio of 3:2 dissolved in a mixed solvent of *N,N*-dimethylformamide (DMF) and dimethylsulphoxide (DMSO) were stirring at 60 °C for 4 h to form the precursor. Then, the methanol is slowly dropped into the precursor until the brown precipitates appear in the precursor, at which point a supersaturated solution was formed. Finally, a beaker containing a supersaturation solution and methanol was placed on a hot plate at 60 °C to grow crystals, as presented in Figure 4a. The as-prepared $\text{Cs}_3\text{Cu}_2\text{I}_5$ SCs exhibit irregular shape with a size of 5 mm and good crystallization characteristics (Figure 4a, right pane). Utilizing the same synthetic method, Lin and co-workers synthesized a rod-shaped CsCu_2I_3 SC, which was achieved by simply changing the ratios of CuI and CsI in the precursor.^[81] The synthesized CsCu_2I_3 SCs have a size of 10 mm × 1.5 mm, being transparent and colorless under sun light but showing shining white emission under ultraviolet (UV) light. In the organic-inorganic hybrid domains, Fang and colleagues reported a new class of PEA-based copper halides SCs using the similar AVC method.^[62] Three kinds of crystals, ((S)-(-)- α -PEA)₄Cu₄I₄, ((R)-(+)- α -PEA)₄Cu₄I₄, and (β -PEA)₄Cu₄I₄ were prepared using DMF as the solvent along with isopropyl alcohol as the

This article is protected by copyright. All rights reserved.

antisolvent. In this experiment, the limpid orange solution was placed in a beaker covered with the fenestrate parafilm. Hence, the solvent is gradually evaporated to grow SC on the bottom of the beaker. It is noteworthy that the AVC technique is highly efficient for growing hybrid TCH SCs, which enables universality and extensibility through an apparent reduction in preparation period and complicity.^[81] However, it still faces the challenge in synthesizing large-size SCs, which also suppresses its associated optoelectronic devices to some extent. Therefore, exploring highly controllable and more efficient AVC approach for the synthesis of large-size and high-quality SCs is worth studying.

3.1.2. Slow Cooling Crystallization

The slow cooling crystallization (SCC) approach is a conventional and broadly technique to synthesize SCs, which is performed by precisely reducing the temperature of the preferred seed solution to induce supersaturation of the solute.^[63,72,91,128–132] After being first used in the synthesis of Rb_2CuBr_3 SCs by the Tang and co-workers, the SCC approach was intensively employed for the growth and research of TCH SCs.^[90] In 2022, Yao et al. reported $5 \times 5 \times 2 \text{ mm}^3$ $\text{Cs}_3\text{Cu}_2\text{I}_5$ SCs for γ -ray detector applications,^[129] which grew from a completely dissolved solution with stoichiometric CsI and CuI dissolved in a mixed acid ($\text{HI}/\text{H}_3\text{PO}_2 = 4:1$). The solution was heated at $63 \text{ }^\circ\text{C}$ and kept constant for 3 days, followed by cooling down to $60 \text{ }^\circ\text{C}$ with a rate of $0.5 \text{ }^\circ\text{C}$ per day. After cooling slowly for 20 days, large and transparent crystals were grown in the solution. Besides, Zou and colleagues reported the synthesis of colorless and transparent millimeter-sized organic-inorganic hybrid $(\text{MA})_4\text{Cu}_2\text{Br}_6$ SCs with sizes up to $12 \text{ mm} \times 2.5 \text{ mm}$.^[91] Note that the $(\text{MA})_4\text{Cu}_2\text{Br}_6$ SCs have efficient luminescence with no self-absorption, and the air stability is also impressive. With the similar method, Zhang et al. prepared a series of hybrid TCH SCs, including $(\text{C}_{16}\text{H}_{36}\text{N})\text{CuI}_2$, $(\text{TBA})\text{CuX}_2$, $(\text{TPA})\text{CuI}_2$, and $(\text{PTMA})_3\text{Cu}_3\text{I}_6$, all of which exhibit highly efficient luminescence properties and are suitable as candidates for down-conversion luminescent devices.^[64,72,73] Recently, Zang et al. developed a pressure-assisted precursor solution cooling strategy to synthesize $\text{Cs}_3\text{Cu}_2\text{I}_5$ and CsCu_2I_3 SCs, which have significantly improved crystallinity and morphology compared to the pressure-free control method.^[122] The key step of pressure-assisted method is the use of the poly(tetrafluoroethylene) lining, which could lead to the formation of crystal nuclei with a corresponding critical nucleation radius. Both pressure-assisted CsCu_2I_3 and $\text{Cs}_3\text{Cu}_2\text{I}_5$ SCs exhibit large sizes of $16 \times 3 \text{ mm}$ and $7 \times 6 \text{ mm}$, respectively. Moreover, both SCs were demonstrated to have superior ambient stability but were ethanol-sensitive. On the contrary, using an inverse temperature

This article is protected by copyright. All rights reserved.

crystallization (ITC) method,^[126] Mo et al. grew stable, centimeter-sized CsCu₂I₃ SCs with length as long as 13 mm as well as good electrical properties (Figure 4b). The synthesis period required 72 h and the obtained CsCu₂I₃ SCs are characterized by a low trap density ($2.95 \times 10^{10} \text{ cm}^{-3}$) and a large carrier mobility ($18.61 \text{ cm}^2 \text{ V}^{-1} \text{ s}^{-1}$), suggesting a promising potential for further optoelectronic devices. Although the ITC strategy shows great merits in the growth of bulk SCs for device fabrication, the long synthesis period may be a restriction in the large-scale fabrication of SCs.

3.1.3. Space-Limited Crystallization Strategy

For optoelectronic devices with vertical architecture structure, single-crystal-thin-films (SCTFs) have more advantages than bulk SCs.^[107,133,134] Inspired by the preparation of SCs that use templates to limit the crystals growth along a certain direction, researchers have proposed a space-limited (SL) crystallization method for the preparation of SCTFs. As an example, Xu et al. reported the planar growth of high-quality CsCu₂I₃ SCTFs on diverse substrates through a SL method.^[107] As illustrated in Figure 4c, they first dripped the pre-prepared precursor (CuI and CsI) onto a clean and flat substrate, then covered the precursor with another same substrate to form sandwich structures. Subsequently, the sandwiched structure was heated at 80 °C, until the precursor solvent was completely evaporated to facilitate the precipitation of CsCu₂I₃ nanostructures under supersaturation. After several hours of growth, many ribbon-like CsCu₂I₃ nanoribbons with lengths of more than 100 μm and widths of several microns to tens of microns were obtained. They also demonstrated that the type of substrates (rigid/flexible, insulating/semiconductor or crystalline/amorphous) owns little effect on the morphology of the synthesized products. The same group also reported modified microchannel-assisted SL methods for the fabrication of the identical SCs but through distinct growth mechanisms.^[133] In this case, the precursor solution was dripped on the microchannel array prepared on polyethylene terephthalate, in which the precursor solution was limited to a narrow channel in a sandwich structure. Due to the capillary effect, the precursor solution could be voluntarily sucked into the microchannel to form an expanded filament array, where the solution would be facilely evaporated to produce CsCu₂I₃ products. When the precursor solution was continuously supplied and the coverslip was removed from the bottom substrates, ultra-long ordered and large-area CsCu₂I₃ microwire (MW) arrays were finally formed along the microchannels. Analogously, Li and co-workers synthesized high-quality Cs₃Cu₂I₅ MW arrays for polarization-sensitive deep-UV photodetectors.^[134] Confinement in the form of limited space in a polydimethylsiloxane (PDMS) template was imported to synthesize single-crystal MW arrays at an inclination angle of about 20° to

This article is protected by copyright. All rights reserved.

ensure complete reaction. Such SL crystallization technique has a concise process and an order of magnitude faster growth rate compared with the classical synthesis methods reported previously, which becomes a relatively universal approach for growing good-quality, size-controlled SCTFs.^[133] However, the sizes and qualities of SCTFs significantly rely on the uniformity of the heating fields and roughness of substrate, which may inadvertently introduce some impurities and defects by changes in the synthetic environment, thus limiting their large-scale development.

3.2. Synthesis of TCH NCs

3.2.1. Hot-Injection Method

With the rapid development of TCH optoelectronic devices, TCH nanocrystals (NCs) recently have attracted considerable research attention as promising materials in optoelectronics applications due to their high PLQY reaching about 100%, and tunable optoelectronic properties by the morphology, composition, size, and dimensionality.^[135–153] In general, hot-injection (HI) approach is the most commonly employed to synthesize colloidal NCs in majority of TCHs currently.^[136,140,145] The HI method is based on the rapid injection of precursor solution into another mixture solution with high boiling point solvents and organic ligands,^[105] which is conducted at high temperature, vacuum, and inert atmosphere, as shown in Figure 4d. In 2019, Han and colleagues reported the colloidal synthesis of all-inorganic Cs₃Cu₂I₅ NCs and CsCu₂I₃ nanorods (NRs) by adopting a HI route and certified that synthesis temperature is the determining factor of the ultimate products.^[139] They found that, at high reaction temperature (about 110 °C), rod-like CsCu₂I₃ NRs with a length of more than 1 μm could be obtained; while at low reaction temperature (about 70 °C), the final product was spherical Cs₃Cu₂I₅ NCs with a diameter of 20 ± 2.5 nm. Almost simultaneously, White and colleagues described the synthesis of composition- and shape-controlled CsCu₂I₃ NRs and Cs₃Cu₂I₅ nanoplates (NPs), and adjusted their functions by temperature control along with ligand concentrations and precursors.^[138] In this experiment, Cs-oleate was rapidly injected into the hot precursor including CuI, oleic acid (OA), 1-octadecene (ODE), and oleylamine (OLA) under an inert atmosphere. The Cs₃Cu₂I₅ NPs were synthesized at 110 °C, while the CsCu₂I₃ NRs were grown at 160 °C. The OLA/OA ligand proportions were regarded exclusively as reconnaissance investigations for better obtaining pure phase products. Later, several groups used similar HI pathways to prepare a family of Cs₃Cu₂X₅ (X = Cl, Br, I) NCs with diverse chemical compositions and morphology properties. For instance, Quan's team reported the preparation of Cs₃Cu₂X₅ NCs by swiftly injection of OLA-X precursor dissolved in ODE into a mixture of Cs-precursor, cupric acetate and OA at 120 °C, following by cooling these

This article is protected by copyright. All rights reserved.

reactants down to room temperature (RT) by cold water bath.^[145] The as-synthesized Cs₃Cu₂I₅ and Cs₃Cu₂Br₅ NCs exhibit rod-like shapes with a size of 21 × 14 nm and 21 × 11 nm, respectively, while the Cs₃Cu₂Cl₅ show a cubic-like morphology with an average edge length of 13 nm. Lian and colleagues using a modified HI method to synthesize stable and highly-luminescent Cs₃Cu₂I₅ NCs, in which the addition of indium iodide (InI₃) to the Cu-precursor plays a key function in controlling the sizes of NCs.^[153] They found that the sizes of Cs₃Cu₂I₅ NCs decrease as the increase of the amount of InI₃, while the In³⁺ ions are not doped into the lattice of Cs₃Cu₂I₅. This approach could also be employed to synthesize Cs₃Cu₂Cl₅ NCs and Cs₃Cu₂Br₅ NCs, which show well-defined quasi-spherical and hexagonal morphologies, respectively. Moreover, Park's group reported a modified HI approach for controlling the size and increasing the yield of Cs₃Cu₂X₅ NCs by using the metal iodide additives to regulate the chemical potential and thermodynamic equilibrium.^[100] The optimized synthesis involves the molar ratio of CuI and MnI₂ in precursor solutions (CuI:MnI₂ = 4:4) and the injection of a metal iodide solution at 160 °C under Ar atmosphere. The final NCs obtained after centrifugation have a monodisperse nanocube shape, with a size of 10.82 nm. Overall, the HI technique has reached maturity to synthesize nearly monodisperse TCH NCs, and the size and morphology of NCs could be controlled by changing the resultant time and temperature, and the type of ligand. However, HI route was commonly applied at air-free atmosphere and high reaction temperature, which may restrain their large-scale production.^[146]

3.2.2. Ligand-Assisted Recrystallization Approach

Compared with high-temperature HI, ligand-assisted reprecipitation (LARP) method is more convenient and low-cost by virtue of their low temperature synthesis and undemanding synthesis condition.^[108,146] The LARP strategy could be described as first dissolving the precursor salts in polar solvents (e.g., DMSO and DMF), followed by dropping the above solution into a mixture of nonpolar solvents (e.g., toluene and hexane) and organic ligands to precipitate NCs, as shown in Figure 4e. The preparation of Cs₂CuX₄ quantum dots (QDs) via LARP could date back to 2018 by Zhao's group.^[60] In a typical LARP reaction, CsBr and CuX₂ were first dissolved in DMSO and DMF, respectively, and then two types of solutions were fully mixed to form a precursor solution. Then, the precursor solution was quickly dropped into the strongly stirred antisolvent (octane) with the OA ligands and n-octylamine. Complete crystallization of the product was achieved in a few seconds at RT and a blue-green colloidal solution was gained. Notably, the size and bandgap tunability of these QDs were also demonstrated by precursor ratios and halide components. In 2019, Halpert and co-worker adopted the

This article is protected by copyright. All rights reserved.

ligand-free antisolvent recrystallization method to synthesize $\text{Cs}_3\text{Cu}_2\text{X}_5$ NCs under ambient conditions.^[146] The precursor solution could be formed after dissolving CsX and CuX in DMSO at RT, and then dropped into antisolvent toluene under vigorous stirring. The obtained $\text{Cs}_3\text{Cu}_2\text{X}_5$ NCs present the spherical-like shapes with a size of 2.68 ± 0.80 nm and show tunable optical properties. Subsequently, White and colleagues presented the synthesis of colloidal Rb_2CuX_3 ($\text{X} = \text{Cl}, \text{Br}$) by LARP strategy.^[108] In this work, both Rb_2CuCl_3 and Rb_2CuBr_3 exhibit nanoplate-like faceted shapes with a size of ≈ 7 nm and an excellent thermal stability. Although considered as a facile technique to prepare the TCH NCs, the LARP method holds no huge superiority in the fabrication of optoelectronic devices, because the characteristics of the products are often inhomogeneous and the PLQY of products is mostly lower than that of counterparts synthesized by HI method. Hence, the synthesis technique of LARP for TCH NCs need further development.

Controlling the shape and size of NCs is an ideal pathway to modulate their optical and electrical properties, thus synthesizing NCs with specific properties can be used in different types of optoelectronic devices.^[144] Compared with the well-developed lead-based perovskite NCs, the tuning window of size and shape of TCH NCs is narrower and the synthesis route is confined to the LARP or HI approaches. However, considering the prosperity of NC preparation in TCHs and the fact that the study on TCHs is still in its infancy, the realization of controllable high-quality TCH NCs in the next few years is worth expecting.

3.3. Synthesis of TCH Films

3.3.1. Spin-Coating Method

There is no doubt that the preparation process of functional films would signally affect the performance of optoelectronic devices.^[154–168] The most common approach to synthesize TCH films is the solution spin-coating technique (Figure 4f), in which the pre-prepared precursor is evenly spin-coated on the substrates and then annealing treatment is performed to enable fast volatilization of solvent.^[88,95] Herein, accurate control of annealing processes would markedly affect the quality of the films. In 2018, Hosono's team synthesized the $\text{Cs}_3\text{Cu}_2\text{I}_5$ films using the one-step spin-coating method similar to that for traditional perovskite films.^[38] The precursor consisting of CuI and CsI dissolved in DMSO was spin-coated on glass substrates. After an annealing at 100 °C for 1 h, a bright luminescent $\text{Cs}_3\text{Cu}_2\text{I}_5$ film was obtained. Based on the classical spin-coating approach, many modified techniques have been developed in the preparation of TCH films. For instance, antisolvent engineering is usually

employed to promote crystallization and improve film quality. Du et al. reported the highly uniform $\text{Cs}_3\text{Cu}_2\text{I}_5$ films without any holes synthesized by using methyl acetate as antisolvent during the deposition.^[156] They uncovered that the increased vapor pressure and decreased boiling point caused by methyl acetate antisolvent lead to rapid crystallization of the $\text{Cs}_3\text{Cu}_2\text{I}_5$, which achieves an improved morphology with a relative low surface roughness of 17.5 nm. Our group further studied the effects of toluene antisolvent dripping time on the microstructure and crystallinity of CsCu_2I_3 films.^[88] In a typical procedure, for the initial stage, the premature introduction of toluene will lead to a lot of pinholes, due to the precursor is far from supersaturated. While a late dripping of toluene has less effect on the nucleation and growth of the CsCu_2I_3 , leading to the deterioration of morphology and poor coverage of CsCu_2I_3 films, which is attributed to the wet films starting to dry and the occurrence of infaust crystallization. Only when the dripping time is appropriate, the precursor is befittingly concentrated by the evaporation of surplus solvents and eventually forms a dense and uniform morphology. Therefore, the antisolvent needs to be dripped during a certain window for obtaining high-quality CsCu_2I_3 films.

On top of that, recent works have been hammered at regulate the crystallization kinetic and stabilize the crystal phase by introducing some multifunctional additives.^[96] Generally, these processing additives could be directly added into the precursor solution or incorporated into the antisolvent as the post-treatment agent. In comparison with the latter, the additives used in precursor solution not only support the nucleation and growth of films, but also have a significant effect on the defect passivation. Wang's group developed a novel organic additive strategy for synthesizing mixed-phase Cs–Cu–I films by adding organic (poly-ethylene glycol sorbitan monooleate, Tween) additive into the precursor.^[96] They discovered that the chemical coordination between the Cs^+ and ether bond in Tween could retard the nucleation and growth of grains in the spin-coating process, thereby enhancing the crystallinity of the films. Moreover, the non-ionic surfactant Tween could suppress the sub-gap state induced by surface dangling bonds, which leads to reduced defects and improved PLQY. Lately, our group adopted a carbazole-containing poly(9-vinylcarbazole) (PVK) as an organic additive to modify the CsCu_2I_3 films.^[95] The control CsCu_2I_3 films without PVK modification suffer from infaust morphology with a farfetched appearance, a low film coverage, and a mass of pinholes. While, PVK with carbazole group forms a strong interaction with the uncoordinated Cu^+ of CsCu_2I_3 at the grain boundaries, which visibly retarded the crystallization period, thus producing a pinhole-free CsCu_2I_3 film with decreased defects. The same group also successfully fabricated a deep-blue

This article is protected by copyright. All rights reserved.

K_2CuBr_3 film by adding the poly(methyl methacrylate) (PMMA) additive into the antisolvent.^[168] The K_2CuBr_3 films with PMMA treatment exhibit better crystallinity, fewer traps, smaller grain size compared with the control sample. The authors attributed the favorable influences of additive to the multipurpose group on PMMA polymer. Besides, PMMA as the protective barriers physically covered the K_2CuBr_3 surface, thus favoring the resistance against moisture, heat, and UV light.

It should be stressed that, although solution spin-coating methods could successfully produce TCH films, realizing high-performance levels comparable to those of record-breaking devices remains a challenge.^[163,166] Therefore, to further enhance the quality of the TCH films for optoelectronic devices and accelerate the feasibility of commercialization, the following two aspects need to be considered. On the one hand, a fundamental understanding of the inherent film crystallization mechanisms is a prerequisite for accurately regulating the crystallization kinetics of material and improving the film quality. Different from the conventional perovskite materials, TCH systems possess the disparate formation behaviors owing to their various material natures. Therefore, exploring the potential film crystallization kinetics that give rise to guide for the crystal growth regulation should be paid more attention. Seen in this light, much more technologies in regard to the scientific in-situ characterizations are expected. On the other hand, the defects in TCH films that determine the optoelectronic properties could be controlled via the passivation engineering of additives that regulate nucleation and growth in the precursor solution or antisolvent.^[96] Therefore, additive passivation engineering is an effective means to reduce the crystal defects via the interaction between the passivator and uncoordinated atoms of the materials, which should hold extending in future research. Lessons learned from perovskite systems, utilizing machine-learning synthesis and high-throughput technique may be an effective pathway to quickly diagnosticate the trap types in various TCH systems and promote the experimental efficiency of finding target additives.

3.3.2. Thermal Evaporation Deposition

The thermal evaporation deposition refers to the physical and chemical process in which raw materials are heated, evaporated and deposited on the substrate in a vacuum environment (Figure 4g).^[102,104,106,154,164] This technique owns many intrinsic advantages over solution-processed method, such as good morphology, accurate control of deposition rate and films thickness, and large-area compatibility.^[117,157] In 2020, Wu and colleagues developed a vacuum dual-source evaporation deposition method to deposit $\text{Cs}_3\text{Cu}_2\text{I}_5$ films, which exhibit a compact and smooth surface with RMS roughness of ≈ 3.6 nm.^[104] Analogously, our group carefully studied the effects of post-annealing

This article is protected by copyright. All rights reserved.

process on $\text{Cs}_3\text{Cu}_2\text{I}_5$ films and investigated their growth dynamics.^[102] It is found that the $\text{Cs}_3\text{Cu}_2\text{I}_5$ films without annealing treatment were not smooth in appearance and many small grains exist on the film surface. While, after an annealing at 100 °C, these undesirable small grains were effectually decreased, which may be attributed to the grain consolidation caused by high-temperature annealing. When the annealing temperature rises to 120 °C, the incorporation of neighbouring grains was further accelerated, and finally a dense and flat $\text{Cs}_3\text{Cu}_2\text{I}_5$ film with few grain boundaries was acquired. Gu et al. deposited heterophase $\text{CsCu}_2\text{I}_3/\text{Cs}_3\text{Cu}_2\text{I}_5$ films by controlling the evaporation rate and component proportion of CsI and CuI sources in the vacuum system.^[106] The resulting $\text{CsCu}_2\text{I}_3/\text{Cs}_3\text{Cu}_2\text{I}_5$ composite films have a dense and fully covered dual-phase morphology, in which the nanorod structure is distributed as CsCu_2I_3 and the other phase with a nanoblock structure is $\text{Cs}_3\text{Cu}_2\text{I}_5$. Overall, the current researches mainly focus on optimising evaporation deposition process to yield uniform, continuous and dense TCH films, which is the prerequisite for high-performance optoelectronic devices. Therefore, an in-depth understanding of the evaporation processes, mechanisms, and influencing factors in the films deposition is crucial to the success of the technique control and design.

3.3.3. Pulsed-Laser Deposition

Another deposition technique that could address the challenge of precisely controlling the deposition rate of the materials is pulsed-laser deposition (PLD).^[166,169,170] PLD is similar to TE technique, that is, precursors are rapidly projected from the source to the substrate in vacuum, but the energy needed to evaporate them is provided by the UV laser irradiation rather than the traditional heat source.^[166] Zhang et al. reported a controllable and convenient PLD method to produce the CsCu_2I_3 films.^[170] As shown in Figure 4h, CuI and CsI raw materials were first mixed in a molar ratio of 2:1, then completely ground in the mortar and pressed into cylindrical targets under a pressure of 40 MPa. Before films growth, the substrate (here refers to Si) was treated with Ar^+ and annealed to further wipe off the oxidation layer. The CsCu_2I_3 film with a growth rate of 4–6 Å/s and a thickness of 800 nm was deposited by UV pulsed laser with a pulse repetition frequency of 5 Hz and a laser energy of 250 mJ/pulse. By controlling the substrate temperature to 200 °C, CsCu_2I_3 films with high crystallinity and few defects were obtained without any buffer layer. The same team also synthesized high-quality $\text{Cs}_3\text{Cu}_2\text{I}_5$ films using the PLD technique with optimized parameters such as heating condition, laser frequency and energy.^[166] However, the use of UV laser involves a complex process, in which the ablated particles have considerable energy and can sputter materials (particularly volatile materials) from the surface of substrate. As a result, the original stoichiometric target may be out of

This article is protected by copyright. All rights reserved.

balance, resulting in an impure film consisting essentially of only one raw material. As the gradual maturity of PLD technique for deposition of TCH films, it is expected that a good deal of stirring breakthroughs can be made in the short run.

4. Luminescence Properties of TCHs

Attaining a clear understanding of the nature of photo-excitation and origin of PL in TCHs is momentous and fundamental for improving device efficiencies.^[171–185] Currently, most explored TCHs were reported to show wide full-width at half-maximum (FWHM), large Stokes shifts and long exciton lifetimes, which could be ascribed to the self-trapped excitons (STEs)-related emission.^[26,30] The major optical properties of representative TCHs have been summarized in **Table 1**. In this section, we will describe the fundamental features of STEs and their luminescence regulation in TCH systems.

4.1. Broadband Emission from STEs

The STEs emission has been widely existed in oxides, metal halides, perovskites, and likewise in TCHs, in which the electron–phonon interactions are strong enough that the photoinduced electron and hole result in elastic lattice deformation.^[30] Once electron and hole are excited, they will be self-trapped fleetly due to the self-trapped states are more stable than the states in which they would move, leading to the lattice distortion of the excited state.^[24] Those excitons with intense exciton–phonon interaction is called “self-trapped excitons” or STEs for abbreviation. It is generally believed that STEs are responsible for the majority of the largely Stokes-shifted broadband emission experimentally measured in TCHs. **Figure 5a** exhibits the PL and absorption spectra of typical $\text{Cs}_3\text{Cu}_2\text{I}_5$ and CsCu_2I_3 materials with STE emission at RT.^[35] Both $\text{Cs}_3\text{Cu}_2\text{I}_5$ and CsCu_2I_3 features wide FWHM of 85 and 115 nm, with large Stokes shifts of 139 and 228 nm, respectively. Zhang and colleagues investigated the wavelength-dependent emission spectra and PL excitation of $\text{Cs}_3\text{Cu}_2\text{I}_5$.^[177] When the monitored emission wavelength changes from 390 to 510 nm, the normalized PL excitation spectra show the same waveforms. Similarly, the PL spectra also exhibit the identical shapes as well when the excitation wavelength varies from 260 to 310 nm. These observations suggest that the broadband blue PL of $\text{Cs}_3\text{Cu}_2\text{I}_5$ arises from the uniform excitation and recombination mechanism. Saporov and colleagues further studied the excitation power-dependent emission spectra of $\text{Cs}_3\text{Cu}_2\text{X}_5$ ($X = \text{Br}, \text{I}$) and found that the PL intensity presents a linear dependence with excitation power,^[43] as shown in Figure 5b, suggesting that the PL rightfully stems from STEs instead of the perpetual defects. This is due to the fact that when the excitation power incremental rises, the PL intensity induced by

intrinsic defects would rapidly attain saturation rather than continuing to increase. Therefore, the STEs emission is intrinsically different from the permanent defects because the disparate sources of PL, although both stem from the lattice defects. Karunadasa et al. elaborated the difference between exciton self-trapping and trapping at permanent defects.^[32] Detailedly, the ground-state of STEs maintains a faultless lattice structure, the transient lattice distortions occur only in the excited state (top of Figure 5c). This differs from the permanent defects, where the lattice distortion exists prior to the light excitation (middle of Figure 5c). Moreover, there is another peculiar external STEs induced by permanent defects or doped ion (bottom of Figure 5c), in which the classical example is $\text{TlCl}_{0.98}\text{Br}_{0.02}$ with the bromides as the defects.

The femtosecond transient absorption (TA) spectroscopy provides a direct evidence for STEs emission in TCHs. Han and colleagues systematically investigated the charge-carrier dynamics of $\text{Cs}_3\text{Cu}_2\text{I}_5$ NCs by TA technology.^[139] As seen in Figure 5d, a broadband pump-induced absorption (PIA) plateau across the probe region (400–700 nm) with energy below that of exciton was detected, which is characteristic of STEs. Further kinetic traces of PIA probed at different wavelengths (450, 550, and 650 nm) exhibit an identical rise time of ≈ 300 fs (inset of Figure 5e), indicating that the broadband PIA of $\text{Cs}_3\text{Cu}_2\text{I}_5$ NCs roots in a single excited STE state. Moreover, the PIA decay curves dominate the slow decay processes over a time window of 1 ns, which is consistent with the microsecond long lifetime of $\text{Cs}_3\text{Cu}_2\text{I}_5$ NCs. Following this, Oum's group reported the direct exploration of excitons self-trapped processes in CsCu_2I_3 by femtosecond TA spectroscopy.^[185] They demonstrated that the edge absorption double-peak spectra are caused by the 130 meV spin-orbit splitting of the Cu *d* electron. Further studies demonstrated that the time constant of the thermally-relaxed free excitons is about 12 ps and the energy barrier is not less than 60 meV. In their study, each process could be obtained through modeling and global dynamic analysis, which may be the mighty experimental descriptions of STEs currently.

Recently, Tang et al. accurately depicted the STEs mechanism and emission kinetics by constructing a configuration-coordinate model (Figure 5f), in which the abscissa axis represents the nuclear coordinate of the luminescence center and the ordinate axis expresses the energy states.^[30] In the STEs process, the excitons would lose some energy, called the self-trapping energy (E_{st}), because the photoexcited excitons undergo the carrier-phonon coupling, inner transformation, and relaxation process. The STEs-related emission is featured by the broadband emission ($\text{FWHM} \geq 60$ nm), which is attributed to the strong interaction between exciton and phonon that results in lattice distortion.

This article is protected by copyright. All rights reserved.

While in the process of lattice distortion, the ground state energy (E_{gs}) and lattice distortion energy (E_d) are increased. Therefore, the final emission energy could be expressed as $E_{PL} = E_g - E_b - E_{st} - E_d$, which is the reason for the large Stokes shifts in STEs-related emission (Figure 5f).

Studying the temperature-dependent PL behaviors of semiconductor is quite helpful for us to understand the photophysics of materials.^[24,34] To gain more insight into the STEs dynamics and exciton-phonon interaction, our group explored the temperature-dependent PL characteristics of the CsCu₂I₃ films.^[88] As presented in Figure 5g, a decrease of PL intensity and a blue shift of emission peak position can be observed with the rise of temperature, which are attributed to the thermally activated non-radiative recombination and lattice expansion, respectively. The exciton binding energy (E_b) of CsCu₂I₃ film could be obtained by fitting the curve relation between the integrated PL intensities and reciprocal temperature using the following formula:^[24]

$$I(T) = \frac{I_0}{1 + A \exp\left(-\frac{E_b}{k_B T}\right)} \quad (1)$$

where k_B is the Boltzmann constant and I_0 is the integrated PL intensity at 0 K. The fitting result of E_b is 202.5 ± 9.7 meV (Figure 5h), which is much higher than the conventional materials with band-edge emission nature.^[10] The large E_b is caused by the 1D electronic structure of CsCu₂I₃. Furthermore, the exciton-phonon coupling of CsCu₂I₃ is revealed by the Huang–Rhys factor (S) and the phonon frequency ($\hbar\omega_{\text{phonon}}$), which could be derived by the following equation:^[24]

$$\text{FWHM}(T) = 2.36\sqrt{S}\hbar\omega_{\text{phonon}}\sqrt{\coth\frac{\hbar\omega_{\text{phonon}}}{2k_B T}} \quad (2)$$

Through fitting the temperature-dependent FWHM curve, as seen in Figure 5i, S factor and $\hbar\omega_{\text{phonon}}$ were extracted as 38.4 and 17.8 meV, respectively. In classic solid-state theory, S can be viewed as the strength of the electron-phonon coupling, which is classified into weak coupling ($S \leq 1$), moderate coupling ($1 < S < 5$), and strong coupling ($S \geq 5$).^[24] Note that the S value of CsCu₂I₃ is far larger than that of most conventional luminescence materials, such as CdSe, ZnSe, and CsPbBr₃.^[90] The strong electron-phonon interaction signifies that CsCu₂I₃ owns a soft crystal nature with large lattice relaxation, which offers a befitting condition for STEs emission. However, the excessive S value results in the intersection of ground state and excited state curves in configuration coordinates, which

This article is protected by copyright. All rights reserved.

results in a non-radiative recombination pathway for exciton dissipation through the release of phonons.^[30] Therefore, the ideal value of S cannot be too large or too small for the efficient STE TCH materials. In addition, Zhang and co-workers investigated the time-resolved PL decays of $\text{Cs}_3\text{Cu}_2\text{Cl}_5$ ranging from 20 to 300 K.^[177] They found that the PL lifetime increases with the rate of $2.7 \mu\text{s}/^\circ\text{C}$ as the decrease in temperature, and all decay curves maintain a monoexponential mode, which indicates that the dynamic of the non-radiative and radiative channels is almost unchanged.

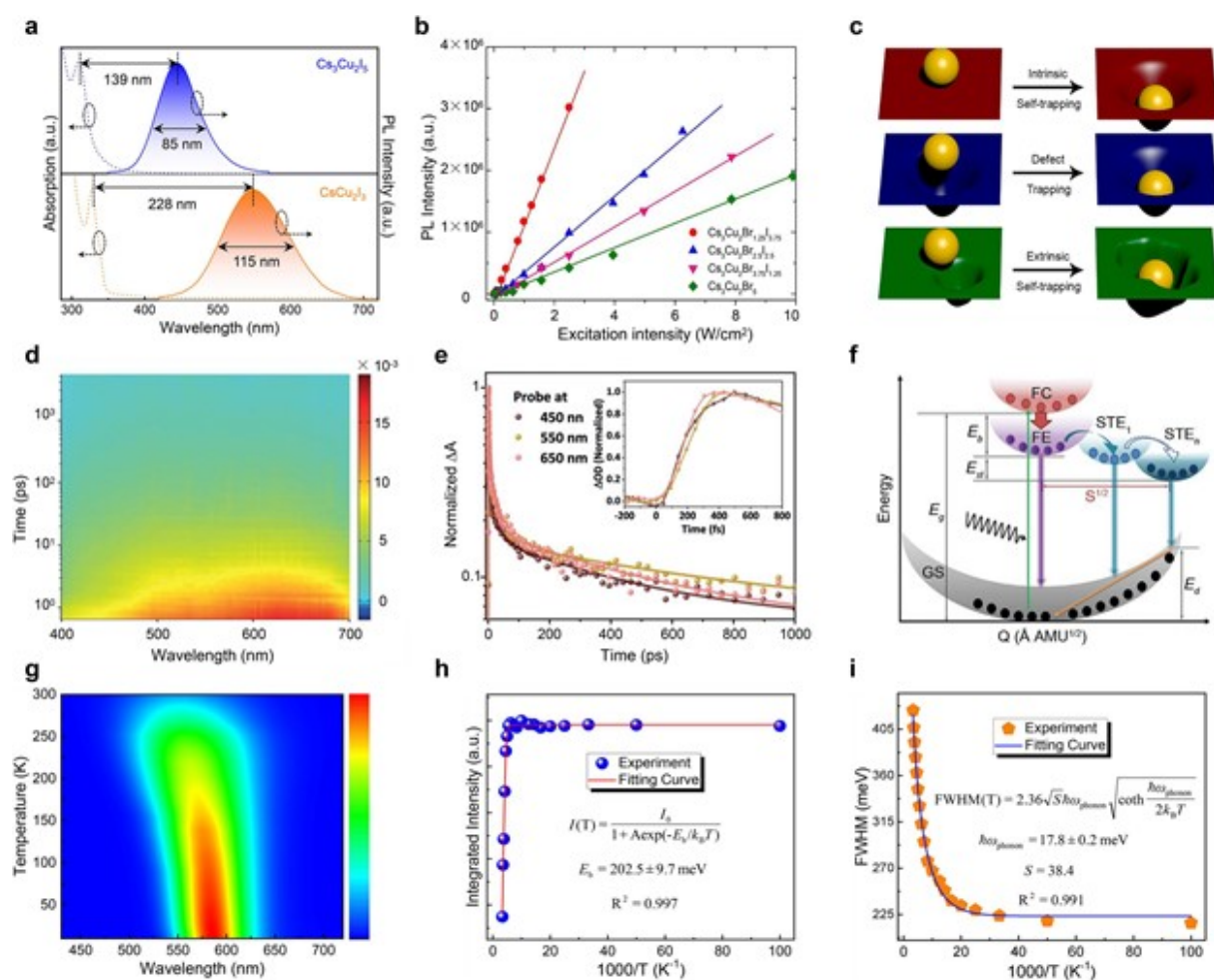


Figure 5. Broadband emission of TCHs observed in the experiment. a) PL and absorption spectra of $\text{Cs}_3\text{Cu}_2\text{I}_5$ and CsCu_2I_3 . (a) Reproduced with permission.^[35] Copyright 2021, Wiley-VCH. b) PL intensity versus excitation power density of $\text{Cs}_3\text{Cu}_2\text{X}_5$ ($X = \text{Br}, \text{I}$). (b) Reproduced with permission.^[43] Copyright 2019, American Chemical Society. c) Schematic diagram of intrinsic STEs (top), defects (intermediate), and external STEs (bottom). (c) Reproduced with permission.^[32] Copyright 2018, American Chemical Society. d) Pseudocolor TA plot and e) TA kinetics of the $\text{Cs}_3\text{Cu}_2\text{I}_5$ NCs. (d,e)

This article is protected by copyright. All rights reserved.

Reproduced with permission.^[139] Copyright 2019, Wiley-VCH. f) Schematic diagram of the photophysical process for the STEs-related PL. (f) Reproduced with permission.^[30] Copyright 2022, Wiley-VCH. g) Pseudocolor mapping of temperature-dependent PL spectra of the CsCu₂I₃ films. h) Integrated PL intensity and i) FWHM of the CsCu₂I₃ as a function of reciprocal temperature. (g–i) Reproduced with permission.^[88] Copyright 2020, American Chemical Society.

4.2. Theoretical Understanding of STEs

To in-depth understand the photophysical mechanisms of broadband emission in TCHs, we reviewed the relevant theoretical calculations in this section.^[47,82,177,186,187] Du et al. investigated the formation of STEs of CsCu₂X₃ by first-principles calculations with hybrid PBE0 functional.^[47] They demonstrated that the STE emission energy of CsCu₂Cl₃, CsCu₂Br₃, and CsCu₂I₃ decreased gradually with the increase of the electronegativity of halogen ions. The calculations reveal that the type of STEs that could reliably exist in CsCu₂X₃ are different for distinct halogen atoms. The STEs emissions of CsCu₂Br₃ and CsCu₂I₃ originate from the radiative transition of the lowest energy level of STEs, while the characteristics of CsCu₂Cl₃ are metastable levels, which are consistent with the experimental results. Our team theoretically authenticated the lattice deformation mode related to the STEs and definitely calculated the STEs-related quantities in both CsCu₂I₃ and Cs₃Cu₂I₅.^[35] As seen in **Figure 6a,b**, the formation process of STEs in CsCu₂I₃ and Cs₃Cu₂I₅ can be clearly deciphered, in which the excitons localization are accompanied by the structural deformation. More precisely, the calculated bond length of Cu1-Cu2 was minished from 2.50 to 2.34 Å for Cs₃Cu₂I₅, while that for CsCu₂I₃ was shortened from 3.07 to 2.74 Å. Meanwhile, the I1-Cu1-I2 angles were enhanced from 108.6° to 128.6° for CsCu₂I₃, and 120.1° to 142.8° for Cs₃Cu₂I₅. Nevertheless, the I3-Cu2-I4 angles were shortened from 123.2° to 117.4° for CsCu₂I₃, and 108.6° to 98.2° for Cs₃Cu₂I₅. Furthermore, the calculated STE energy results show good agreement with the experimentally obtained values, which provide a deeply understanding of the STEs luminescence. Zhang et al. calculated the PDOS of Cs₃Cu₂I₅ with pristine and distorted structures,^[177] and found that extra peaks were examined above host valence band of the distorted structure compared with the pristine structure (Figure 6c). From the real space charge distributions of the VBM, the charge localization in the distorted structure is more significant than that in the pristine structure (Figure 6d). This shows that the couplings between Cu 3d_{z²} orbitals are much stronger in the distorted structure, which can be attributed to the shrunken volume of [Cu₂X₅]³⁻ species (Figure 6e). Lin and colleagues³ proposed that the STEs recombination also follows the parity-forbidden transition.^[82] As shown in Figure 6f, the three recombination

This article is protected by copyright. All rights reserved.

pathways for STEs include transitions from I $5p$ to Cu $4s$, from I $5p$ to Cu $3d$, and from Cu $4s$ to I $5p$. Due to the nature of large hole effective mass, the formed STEs may be dominated by I $5p$ and Cu $3d$, and the allowed STEs are the Cu $4s$ –I $5p$ and I $5p$ –Cu $3d$, while other forbidden transitions are dark states.

Although the formation of STE is considered as the origin of large Stokes-shifted broadband emission, the relationship between STE and high luminescence efficiency is still unknown. Taking $\text{Cs}_3\text{Cu}_2\text{I}_5$ as an instance, Walsh and colleagues discussed the photochemical properties of $\text{Cs}_3\text{Cu}_2\text{I}_5$ from the first-principles calculations,^[187] and revealed that the low energy barrier for exciton self-trapping is responsible for the efficient emission in $\text{Cs}_3\text{Cu}_2\text{I}_5$. They constructed the potential energy surface of ground, excited singlet, and excited triplet states in $\text{Cs}_3\text{Cu}_2\text{I}_5$, as shown in Figure 6g. The energy barrier between excited singlet-state and excited triplet-state transition is a crucial factor that determines the dynamics of exciton self-trapping and the STEs luminescence efficiency. The calculated exciton self-trapped barrier has a low value of 0.09 eV, while the exciton de-trapping barrier is 0.48 eV, indicating that most of the photogenerated excitons produce photon emission through a vertical transition from excited triplet state to ground state, rather than triplet excitons dissociating into the free carriers. The local geometric structure of $[\text{Cu}_2\text{I}_5]^{3-}$ cluster in the excited triplet-state and ground-state is presented in Figure 6h. The authors further plotted the changes in quantum yield and reaction rate as a function of charge carrier concentration at 300 K. As displayed in Figure 6i, the quantum yield is estimated to be $\approx 100\%$ in the low carrier concentration area, which manifests that most carriers experience exciton self-trapped process before recombination through the band-edge transition. Therefore, $\text{Cs}_3\text{Cu}_2\text{I}_5$ is a highly-efficient blue emitter for the low excitation power density.

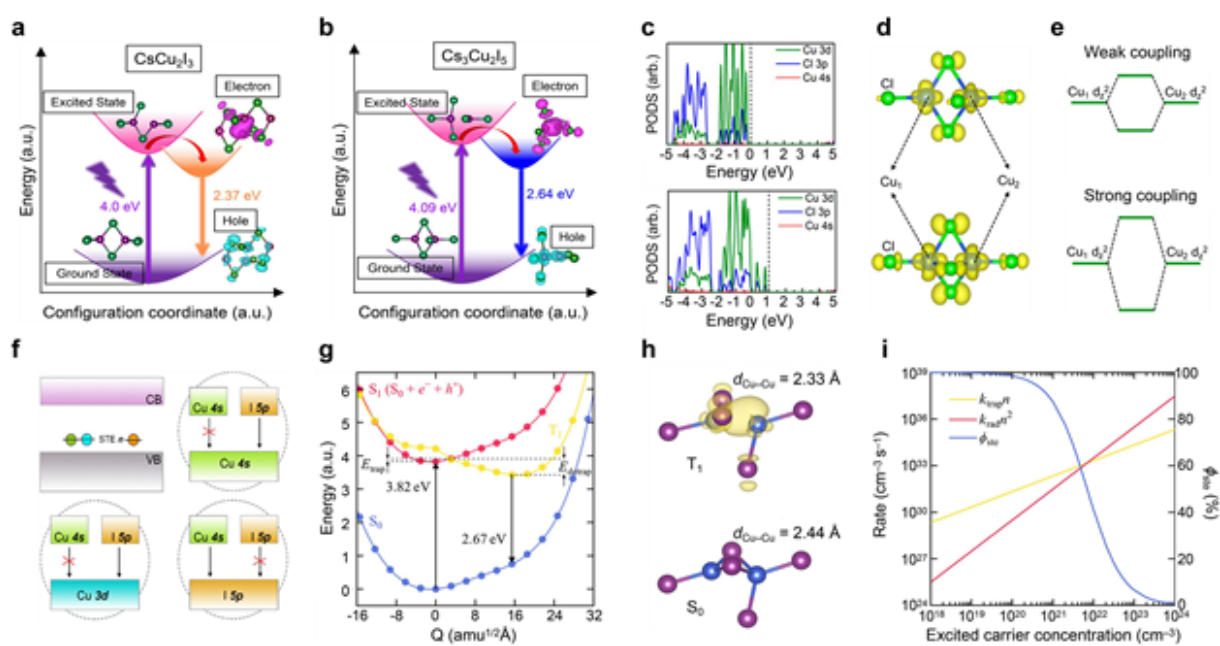


Figure 6. Theoretical calculations of STEs emission in TCHs. a,b) The configuration coordinate diagrams of STE processes of CsCu_2I_3 and $\text{Cs}_3\text{Cu}_2\text{I}_5$, respectively. (a,b) Reproduced with permission.^[35] Copyright 2021, Wiley-VCH. c) PDOS of pristine (top) and distorted (bottom) structures of $\text{Cs}_3\text{Cu}_2\text{Cl}_5$. d) Charge distributions of the VBM for pristine (top) and distorted (bottom) structure of $\text{Cs}_3\text{Cu}_2\text{Cl}_5$, with the band coupling shown in panels e). (c–e) Reproduced with permission.^[177] Copyright 2020, American Chemical Society. f) Multiple STE luminescence processes. Parity selection rule results in a part of STE to be forbidden, called dark STE states. (f) Reproduced with permission.^[82] Copyright 2020, American Chemical Society. g) Potential energy surface of ground, excited singlet, and excited triplet states within $\text{Cs}_3\text{Cu}_2\text{I}_5$. h) Atomic structures of the $[\text{Cu}_2\text{I}_5]^{3-}$ cluster in the excited singlet state and ground state. i) Photoexcited carrier concentration-dependent radiative transition rate, self-trapped rate, and quantum yield of STEs. (g–i) Reproduced with permission.^[187] Copyright 2021, American Chemical Society.

5. Luminescence Regulation of TCHs

Although TCHs emerge exciting luminescence properties, PL regulation or optimization is still critical for these materials to reach commercialization.^[188–195] Generally speaking, the PL properties could be easily adjusted by changing the chemical composition, phase control, doping, pressure effect, and polarization dependence.^[196–200] In this section, we will discuss some representative studies on luminescence regulation of TCHs in the past several years.

This article is protected by copyright. All rights reserved.

5.1. Composition Engineering

The previous discussions predict the tunability of luminescence properties in TCHs because the feasibility of chemical composition strategy. Similar to that of lead-based perovskites, the bandgap control and color tuning of TCHs can also be easily regulated by halogen substitution.^[145,146] **Figure 7a–c** show the absorption, PL excitation, PL, and time-resolved PL decay spectra of Cs₃Cu₂X₅ NCs. The bandgap values of Cs₃Cu₂I₅, Cs₃Cu₂Br₅, and Cs₃Cu₂Cl₅ were derived to be 4.40, 4.33, and 4.43 eV respectively, calculated by the Tauc plot method. Note that the emission peak of Cs₃Cu₂X₅ exhibits a clear blue shift as the halide composition varies from Cl to Br, and to I (Figure 7b), which is opposite to the red shift of luminescent halide-containing perovskites. Such a blue shift is ascribed to the synergistic effect of the apparent bandgap changes along with the lattice distortion energy and self-trapping energy.^[145] In addition, the PL lifetimes of Cs₃Cu₂I₅, Cs₃Cu₂Br₅, and Cs₃Cu₂Cl₅ NCs are measured to be 1.56, 14.12, and 135.97 μs, respectively, all of which sustain an analogous monoexponential decay (Figure 7c). Due to the different lattice distortion energies of halide ions and Cu ion bonds, the self-trapped depth abides by the law of Cl > Br > I, which account for the faster decay of Cs₃Cu₂I₅. Among the three types of NCs containing different halogens, the PLQY of Cs₃Cu₂Cl₅ is the highest (48.7%), while the PLQYs of Cs₃Cu₂Br₅ and Cs₃Cu₂I₅ are 16.9% and 29.2%, respectively, which are lower than their bulk materials reported previously.^[38,43] Roccanova co-workers also demonstrated the highly-efficient blue Cs₃Cu₂Br_{5-x}I_x materials via mixed halogen strategy.^[43] The resulting Cs₃Cu₂Br_{5-x}I_x exhibits emission peak changing from 443 to 456 nm with the Commission Internationale de L'Eclairage (CIE) color coordinate shifting from (0.15, 0.048) to (0.15, 0.067). Contrary to the blue shift of Cs₃Cu₂X₅ emission with the increase of anion radii, the PL peak of single halide CsCu₂X₃ presents a continued red shift with a rise in the Stokes shifts.^[48] Note that the PL shift of mixed halide CsCu₂Br_{1.5}I_{1.5} and CsCu₂Cl_{1.5}Br_{1.5} does not follow a linear tendency, and their peak positions are more red-shifted than those of single-halide compounds, similar to MAPb(I/Br)₃ system. These aberrations are attributed to the presence of large structural distortion derived from different halogen elements, which can influence the self-trapping depth in the bandgap, leading to a red shift of PL peak.

The substitution of metal Rb or K ion with small ion radius for Cs ion leads to the formation of efficient violet-emitting Rb₂CuX₃ and K₂CuX₃ (X = Br and Cl), which is seen as an additional tactic for luminescence regulation.^[52,90,201,202] For example, the Rb₂CuBr₃ SCs reported by Tang's team exhibit a PL position located at 385 nm with a near-unity PLQY of 98.6% and a large Stokes shift of

This article is protected by copyright. All rights reserved.

85 nm.^[90] Creason co-workers investigated the optical properties of Rb_2CuBr_3 and Rb_2CuCl_3 ,^[54] which show strong violet emission at 385 and 395 nm with PLQYs of 64% and 85%, and FWHMs of 54 and 52 nm, respectively. Moreover, they also discovered a phonon-assisted anti-Stokes PL characteristic in Rb_2CuCl_3 , and an optical cooling efficiency of up to 32% is estimated taking advantage of this unique property, which is due to the relatively low trap-state density and the high PLQY of Rb_2CuCl_3 . Similarly, the PL spectra of K_2CuCl_3 and K_2CuBr_3 show narrow emission peaks located at 392 and 388 nm with FWHMs of ≈ 54 nm,^[55] and the intense violet PL at RT is impressive with the PLQY values up to $\approx 97\%$. Interestingly, through a solvent-induced phase transition strategy, Halpert et al. realized the transformation from blue-emitting $\text{Rb}/\text{K}_2\text{CuBr}_3$ to red-emitting $\text{Rb}/\text{KCB-DMSO}$, which has a reversible characteristic.^[116] The resulting organic-inorganic hybrid $\text{Rb}/\text{KCB-DMSO}$ is the report of copper halide extended to the red light region, with PL peak at 670 nm for KCB-DMSO and 686 nm for RCB-DMSO , respectively.

Figure 7d summarizes the recent progress of PLQY for various TCHs. Despite component modulation has been developed to broaden their spectral coverage (Figure 7e,f), the PL spectrum of most materials only covers part of visible-light band, featuring broadband emission in violet, blue, green or yellow regions. That is to say, there are still some challenges in realizing red- and near-infrared-emitting TCHs. Moreover, the PLQY of TCHs are not particularly high, especially in the sky-blue and yellow regions, ranging from 10% to 60%, which may limit their specific applications.^[26,27] There are two main reasons that can be explained here. On the one hand, the intrinsic bulk/surface defects of TCHs can form defect recombination centers to increase the probability of non-radiative recombination, thus resulting in reduced PLQY. These defects mainly include halogen and A-site vacancy defects, copper and halogen substitution defects, metal copper impurities, etc., as reported by Yin et al.^[79] On the other hand, some TCHs possess an indirect bandgap nature,^[93] in which absorption and recombination incorporated both phonons and photons. In these materials, the phonon-mediated non-radiative process dominates the recombination pathway, so that they usually appear as “dark” STEs with low PLQY. Therefore, the defect understanding of TCHs and the non-radiative recombination processes should first be comprehensively and deeply studied. Further attempts should be focus on improving PLQY by defect passivation engineering, doping or alloying, and controlling the spatial distribution of composite. Moreover, the most advanced Recommendation BT 2020 (Rec. 2020) standard requires that the monochrome RGB primary colors should reach (0.71, 0.29), (0.17, 0.80) and (0.13, 0.05) for red, green and blue in CIE color

This article is protected by copyright. All rights reserved.

coordinates. However, the green- and red-emitting TCHs suffer from lower color purity than the desired values due to the inherent broadband characteristics (Figure 7g). Conversely, the broadband white-light emission is worth expecting in TCHs. Therefore, future work on the exploration of TCHs with narrow FWHM is urgently needed, which is of great significance to broaden their optoelectronic applications.

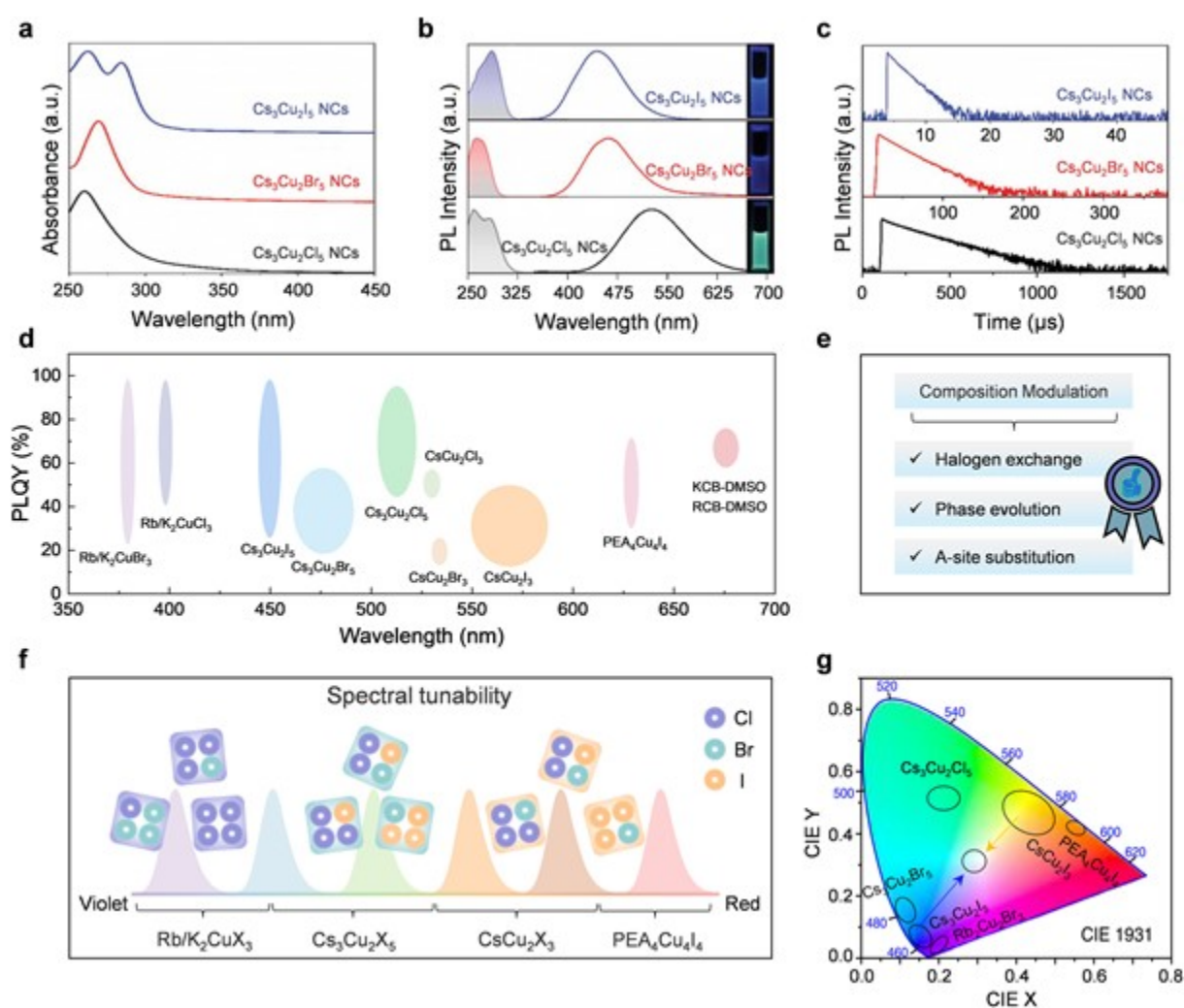


Figure 7. Composition-related optical properties of TCHs. a) UV-vis absorption spectra, b) PL excitation and PL spectra, and c) time-resolved PL decay curves of $\text{Cs}_3\text{Cu}_2\text{X}_5$ NCs. (a–c) Reproduced with permission.^[145] Copyright 2019, Wiley-VCH. d) Schematic summary of PLQY of TCHs. e) Strategies for composition-related PL regulation of TCHs. f) Schematic representation of spectral

This article is protected by copyright. All rights reserved.

tunability in TCHs achieved by composition engineering. g) CIE color distribution of different TCH systems.

5.2. Phase Control and Doping

Chemical transformation is an interesting phenomenon and an effective way for regulating the optical properties of materials.^[203–205] Shi's group observed the PL spectrum regulation of TCHs and achieved the reversible phase transition between yellow-emitting CsCu_2I_3 and blue-emitting $\text{Cs}_3\text{Cu}_2\text{I}_5$.^[203] Specifically, when CsI or CuI was added into the halide products, $\text{Cs}_3\text{Cu}_2\text{I}_5$ reacts with CuI to form CsCu_2I_3 ; CsCu_2I_3 can be converted to $\text{Cs}_3\text{Cu}_2\text{I}_5$ by reacting with CsI. The proposed chemical reaction processes could be written as: $\text{Cs}_3\text{Cu}_2\text{I}_5 + 4\text{CuI} \rightarrow 3\text{CsCu}_2\text{I}_3$ and $\text{CsCu}_2\text{I}_3 + 2\text{CsI} \rightarrow \text{Cs}_3\text{Cu}_2\text{I}_5$. Zhang et al. discussed the reversible chemical transformation between $\text{Cs}_3\text{Cu}_2\text{I}_5$ and CsCu_2I_3 accompanied by a change in their emission color triggered by ethanol or CsI (**Figure 8a**).^[178] They found that $\text{Cs}_3\text{Cu}_2\text{I}_5$ powder was completely converted to CsCu_2I_3 by ethanol washing, while CsCu_2I_3 powder was completely converted to $\text{Cs}_3\text{Cu}_2\text{I}_5$ by CsI triggering. Moreover, temperature is a pivotal factor in the transform process, in which high reaction temperature results in fast chemical transformation and molecular movement. Analogously, Tang et al. reported the relationship between PL modulation and phase transformation of Cs–Cu–I systems on the nanoscale.^[198] The colloidal $\text{Cs}_3\text{Cu}_2\text{I}_5$ NCs with bright blue emission can be transformed into the CsCu_2I_3 microrods with yellow emission by controlling the stagnation temperature at above 120 °C. Besides, the evolution of phase transition and emission color was clearly observed by adding polar ethanol solvent into the colloidal $\text{Cs}_3\text{Cu}_2\text{I}_5$ NCs solution, as illustrated in the vivid patterns in Figure 8b. The coexistence of $\text{Cs}_3\text{Cu}_2\text{I}_5$ and CsCu_2I_3 after stirring in ethanol was demonstrated by Zhu and co-workers.^[193] By controlling the optimal reaction time of 5 h in ethanol, $\text{Cs}_3\text{Cu}_2\text{I}_5$ is substantially transformed into CsCu_2I_3 (Figure 8c), which is confirmed by XRD and spectral results at different periods. $\text{Cs}_3\text{Cu}_2\text{I}_5$ is considered to be the “CsI-rich” structures, in which the dissolution of CsI leads to the transition from $\text{Cs}_3\text{Cu}_2\text{I}_5$ to CsCu_2I_3 . With the increase of polarity of the solvent and reaction time, more CsI is peeled from the $\text{Cs}_3\text{Cu}_2\text{I}_5$ and the conversion rate rises, indicating that the “CsI-peeling” processes are the reason for the above conversion (Figure 8d). Accordingly, accurate control of reaction condition could not only realize the fabrication of CsCu_2I_3 with a yield of 100%, but also achieve the white emission. However, the transformation process of different phases containing chlorohalogen (between $\text{Cs}_3\text{Cu}_2\text{Cl}_5$ and CsCu_2Cl_3) and bromohalogen (between $\text{Cs}_3\text{Cu}_2\text{Br}_5$ and CsCu_2Br_3) materials is scarcely explored, and the directly experimental verification has not been achieved.

This article is protected by copyright. All rights reserved.

Doping photoactive metal ion, such as Mn^{2+} , has been widely demonstrated as a resultful strategy to impart new optical and electronic characteristics of host without altering their crystal structure in many TCHs.^[206–209] This approach has been employed to tune the PL and improve the PLQY of TCHs. Du co-workers demonstrated a battery of new Mn^{2+} -doped $\text{Cs}_3\text{Cu}_2\text{I}_5$,^[209] which exhibit not only featured emission peak at 448 nm of intrinsic Cu^+ -related STEs but also a green PL peak at 550 nm from the ${}^4\text{T}_{1g} \rightarrow {}^6\text{A}_{1g}$ transition of Mn^{2+} . The energy transfer efficiency between Cu^+ and Mn^{2+} ions can reach 57% when the concentration of Mn^{2+} ions is 2 mol%. Interestingly, the emission intensity of Mn^{2+} and Cu^+ decrease with rising temperature from RT to 498 K, while the emission of Mn^{2+} is less sensitive to temperature than that of Cu^+ . Analogous result was also presented by Zeng's team that Mn^{2+} doping signally activates yellow emission in $\text{Cs}_3\text{Cu}_2\text{I}_5$,^[97] thus increasing the PLQY to 23.1% due to the energy transfer from $\text{Cs}_3\text{Cu}_2\text{I}_5$ or direct excitation of Mn^{2+} . Chen et al. reported that, by introducing alkali metal Na^+ ions in Mn^{2+} -doped $\text{Cs}_3\text{Cu}_2\text{I}_5$,^[186] simultaneously promoted double emission bands from STE and Mn^{2+} with an improved PLQY of 62.06% was observed (Figure 8e,f). Theoretical calculation shows that doping with alkali metals can cause lattice deformation and enhance the mutual effect between $[\text{MnI}_4]^{2-}$ and $[\text{CuI}_4]^{3-}$ tetrahedrons, which facilitates the $\text{STE} \rightarrow \text{Mn}^{2+}$ energy transfer. Figure 8g illustrates the energy transfer processes and PL enhancement mechanisms. In the whole PL generation, besides the blue emission produced by the intrinsic STE state (process I), there is also yellow emission that derives from the energy transfer from free exciton and STEs to the energy level of Mn^{2+} (processes II and III). On the one hand, Mn^{2+} doping causes the lattice deformation and facilitates the $\text{STE} \rightarrow \text{Mn}^{2+}$ energy transfer. On the other hand, the suppressed non-radiative recombination of the STEs also alleviates the competitive factor of the energy transfer, thus leading to the enhanced Mn^{2+} emission significantly. Doping with cations such as Cd^{2+} , Na^+ , Tl^+ , and In^{3+} has also been demonstrated to exhibit PL enhancement for $\text{Cs}_3\text{Cu}_2\text{I}_5$.^[176,186,197,209,210] For example, $\text{Cs}_3\text{Cu}_2\text{I}_5:\text{In}^{3+}$ possesses bright and tunable double emissions, and the PLQY of resulting $\text{Cs}_3\text{Cu}_2\text{I}_5:\text{In}^{3+}$ from 68.1% to 88.4%.^[210] The emission intensity of Na^+ -doped $\text{Cs}_3\text{Cu}_2\text{I}_5$ is improved by 17.4% compared to the pristine $\text{Cs}_3\text{Cu}_2\text{I}_5$, and the thermal stability is enhanced as well.^[206] However, the modulation effectiveness of doping strategy on the PL properties for other TCH systems (such as $\text{Cs}_3\text{Cu}_2\text{Cl}_5$, CsCu_2I_3 , and Rb_2CuBr_3) has not been realized experimentally, which needs further exploration in the future.

This article is protected by copyright. All rights reserved.

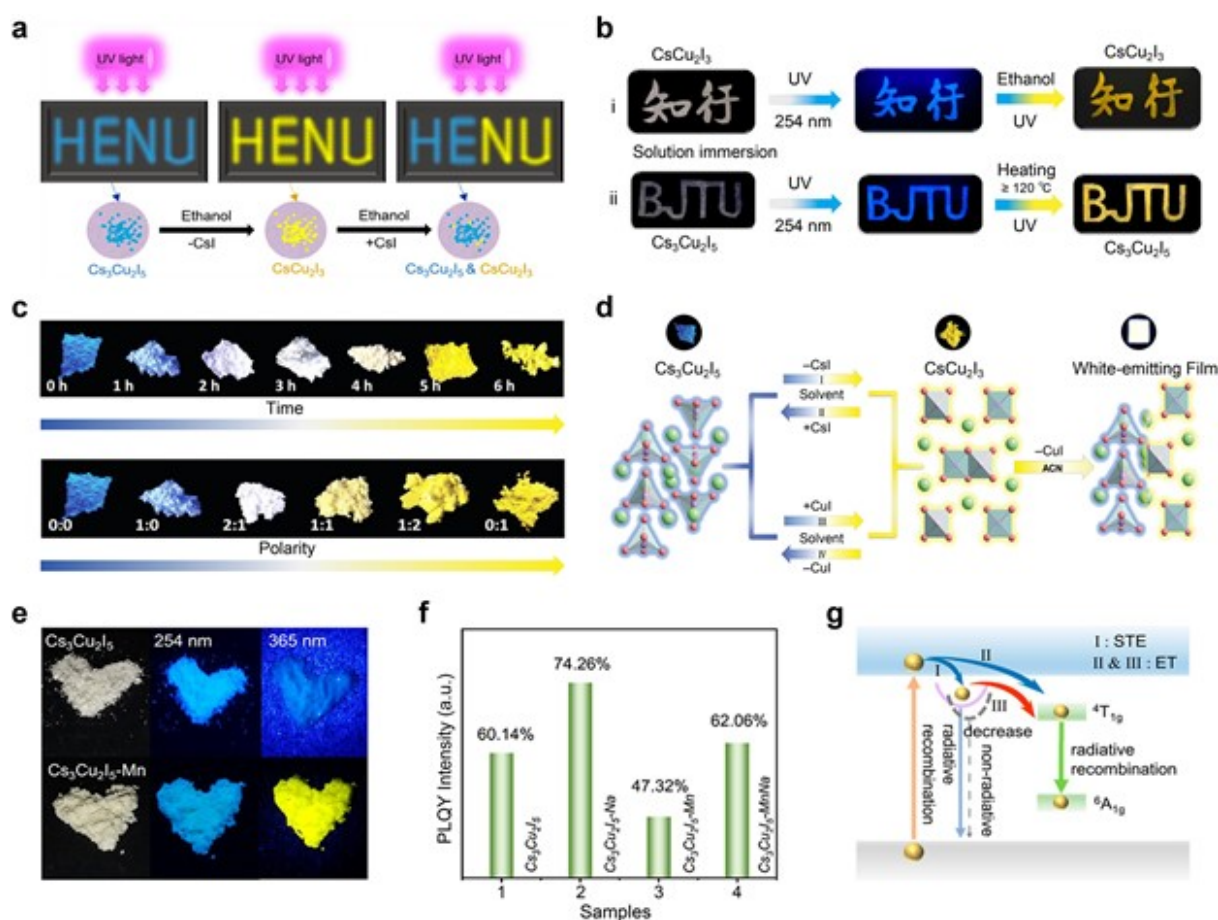


Figure 8. Tunable optical properties via phase control and doping. a) Recoverable emission color change between blue $\text{Cs}_3\text{Cu}_2\text{I}_5$ and yellow CsCu_2I_3 . (a) Reproduced with permission.^[178] Copyright 2021, American Chemical Society. b) Emission photographs of the $\text{Cs}_3\text{Cu}_2\text{I}_5$ NCs-coated paper treated with ethanol and heated at high temperature. (b) Reproduced with permission.^[198] Copyright 2022, American Chemical Society. c) A series of photographs showing the reversible phase transition between $\text{Cs}_3\text{Cu}_2\text{I}_5$ and CsCu_2I_3 through ethanol reaction time and solvent polarity control. d) Schematic diagram of phase conversion processes. (c,d) Reproduced with permission.^[193] Copyright 2020, Royal Society of Chemistry. e) Photographs of $\text{Cs}_3\text{Cu}_2\text{I}_5$ and Mn^{2+} -doped $\text{Cs}_3\text{Cu}_2\text{I}_5$ under sunlight and UV light (254 and 365 nm). f) PLQY of doped and undoped $\text{Cs}_3\text{Cu}_2\text{I}_5$. g) Schematic diagram of the emission processes in Mn^{2+} -doped $\text{Cs}_3\text{Cu}_2\text{I}_5$. (e–g) Reproduced with permission.^[186] Copyright 2022, American Chemical Society.

5.3. Pressure Effect and Polarization Dependence

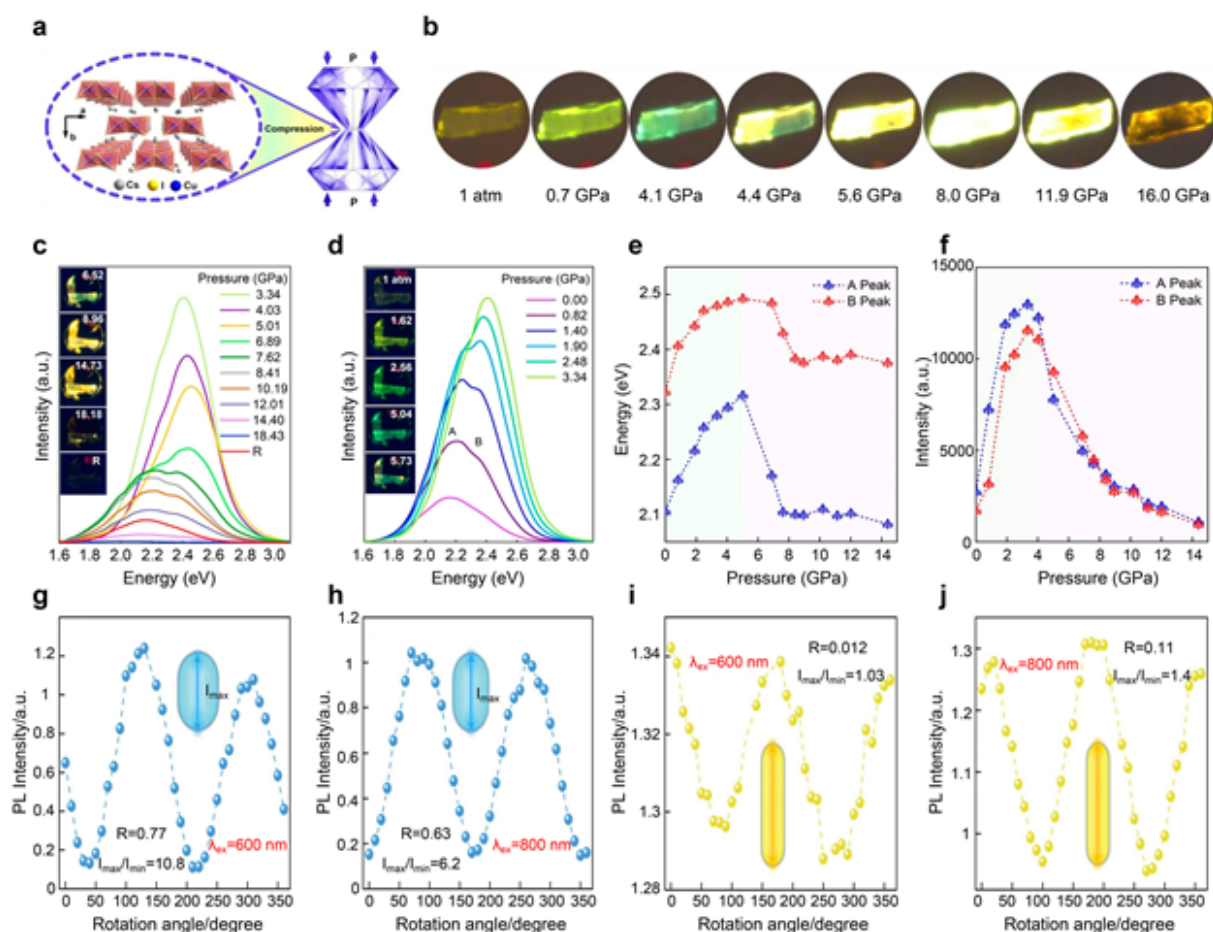
This article is protected by copyright. All rights reserved.

High pressure technique is a forceful means to modulate the lattice distortion and electronic structure of materials, which in turn changes their luminescence characteristics and ferrets the understanding of structure–property relationship at the atomic level.^[84,119,124] Quan and co-workers studied the optoelectronic characteristics of CsCu₂I₃ SCs with employed pressure up to 16.0 GPa utilizing the diamond anvil apparatus (**Figure 9a**).^[119] As displayed in Figure 9b, the PL micrographs of CsCu₂I₃ SCs inch by inch change from yellow to green as the pressure increases to 4.1 GPa, accompanied by a successive blue shift of the emission peak. At a critical pressure of 8.0 GPa, the PL intensity reaches the maximum. Further increasing the compression would result in the quenching of emission intensity. The structure deformation of tetrahedron is account for enhanced STE emission with different magnitudes, which is proved by high pressure angle-dispersive XRD and Raman. Huang and colleagues studied the variation of structure, electronic and optical properties under high pressure to reveal the emission chaos observed in CsCu₂I₃.^[84] The PL spectra of CsCu₂I₃ as a function of pressure are seen in Figure 9c–e. It was found that as the pressure enhances, two major emission peaks clearly exhibit blue shift and then tardily toward the long-wavelength band. Meanwhile, both peaks show an increased PL intensity from 0 to \approx 4.0 GPa, and then decreases under further compression (Figure 9f). The optical bandgap rises from 3.57 to 3.62 eV within a pressure range from 0 to \approx 4.0 GPa, and then reverses to below 3.30 eV at 14.0 GPa. These anomalous properties are ascribed to the structural phase transformation from the *pnma* to *cmcm* of CsCu₂I₃ under high pressure conditions. In short, a deeply research of the pressure-induced emission evolution behaviors of TCHs is critical to further understanding the structure–property relationship, which also provides a new insight for modulating their emission luminescence.

A method to decrease the energy dissipation in the future display and lighting materials is to adopt compound that emits polarized light, as this allows for the fabrication of high-performance devices with low energy dissipation.^[72,182,199] Therefore, understanding and discovering the polarization emission effect in TCHs is expected to break through the barriers of traditional materials with high polarization anisotropy ratio, because TCHs structure own the advantages of inherent asymmetry and distorted crystal structure of the unit cell. Our group reported polarization-sensitive emissions from 1D CsCu₂I₃ materials.^[182] According to the variation in the PL spectra of CsCu₂I₃ versus the polarization angles, at an angle of 0°, the emission intensity presents a peak value then declines inch by inch with a variation in the polarization angle and realizes the lowest at 90°. The calculated PL polarization ratio reaches 1.7, which rooted in the combined effect of 1D morphology and anisotropic

This article is protected by copyright. All rights reserved.

crystal structure. Based on the highly ordered self-assembly of $(\text{PTMA})_3\text{Cu}_3\text{I}_6$ clusters, Zhang and colleagues studied the polarization emission properties of long-strip $(\text{PTMA})_3\text{Cu}_3\text{I}_6$ microplates.^[72] They found that the PL intensity of the samples consumingly counts on the polarization angle, in which the maximum emission intensity (I_{max}) arises at the polarization angles of 0° and 180° , while the minimum emission intensity (I_{min}) appears at the polarization angles of 90° and 270° . Based on the emission dichroic ratio of $I_{\text{max}}/I_{\text{min}}$, the PL polarization ratio was estimated to be 1.78, indicating a highly-polarized PL character of the $(\text{PTMA})_3\text{Cu}_3\text{I}_6$ microplates. More recently, He and coworkers analyzed the multiphoton excited emission anisotropy of the $\text{Cs}_3\text{Cu}_2\text{I}_5$ and CsCu_2I_3 by rotating a polarizer.^[199] According to the multiphoton excited angle-dependent emission intensity (Figure 9g,h), the derived values of $I_{\text{max}}/I_{\text{min}}$ in $\text{Cs}_3\text{Cu}_2\text{I}_5$ were estimated to be 10.8 at 600 nm excitation (two-photon) and 6.2 at 800 nm excitation (three-photon). For CsCu_2I_3 , much smaller values of 1.03 (600 nm excitation) and 1.4 (800 nm excitation) were obtained, as shown in Figure 9i,j. This difference in anisotropy factors is due to the diversity in the internal structure asymmetry of CsCu_2I_3 and $\text{Cs}_3\text{Cu}_2\text{I}_5$.



This article is protected by copyright. All rights reserved.

Figure 9. PL modulation via pressure effect and polarization dependence. a) Diagram of diamond anvil cell for CsCu₂I₃ high-pressure experiment. b) Optical photographs of CsCu₂I₃ crystals under different pressure compression. (a,b) Reproduced with permission.^[119] Copyright 2020, American Chemical Society. c,d) PL spectra and PL micrographs of CsCu₂I₃ under various high pressures. e) Emission peak and f) intensity of CsCu₂I₃ versus pressure. (c–f) Reproduced with permission.^[84] Copyright 2021, American Chemical Society. g,i) Two-photon and h,j) three-photon excited PL intensity of Cs₃Cu₂I₅ and CsCu₂I₃ versus rotation angle. (g–j) Reproduced with permission.^[199] Copyright 2020, Royal Society of Chemistry.

Table 1. Summary of photophysical properties of representative TCH materials.

Formula	PLE Peak (nm)	PL Peak (nm)	PLQY (%)	FWHM (nm)	Stokes shift (nm)	Lifetime (μs)	Morphology	Ref.
CsCu ₂ Cl ₃	319	527	48	102	208	≈0.013	Powders	[48]
CsCu ₂ Cl _{1.5} Br _{1.5}	340	587	0.37	200	247	≈0.015	Powders	[48]
CsCu ₂ Br ₃	319	533	18.3	106	214	≈0.018	Powders	[48]
CsCu ₂ Br _{1.5} I _{1.5}	335	584	0.38	128	249	≈0.026	Powders	[48]
CsCu ₂ I ₃	334	576	3.23	126	242	≈0.062	Powders	[48]
CsCu ₂ I ₃	328	568	15.7	≈75	≈240	≈0.63	SCs	[81]
CsCu ₂ I ₃	315	560	8	≈107	≈245	0.149	Films	[158]
CsCu ₂ I ₃	≈328	≈585	6.5	≈126	≈257	–	SCs	[119]
CsCu ₂ I ₃	320	≈550	20.6	100	225	0.17	Films	[88]
CsCu ₂ I ₃	331	≈575	6	54	≈244	–	Powders	[184]
CsCu ₂ I ₃	≈330	575	12.1	119	245	–	Crystals	[203]
CsCu ₂ I ₃	321	561	11	≈120	≈240	0.104	NCs	[138]
CsCu ₂ I ₃	324	553	5	≈120	≈229	–	NCs	[139]
CsCu ₂ I ₃	≈360	575	11	111	215	0.12	NCs	[146]

This article is protected by copyright. All rights reserved.

Cs_2CuCl_4	–	388	51.8	68	–	–	NCs	[60]
Cs_2CuBr_4	–	393	37.5	74	–	–	NCs	[60]
$\text{Cs}_3\text{Cu}_2\text{Cl}_5$	≈ 280	516	78	≈ 100	≈ 236	–	Films	[51]
$\text{Cs}_3\text{Cu}_2\text{Cl}_5$	≈ 275	510	99	95	235	109	Films	[56]
$\text{Cs}_3\text{Cu}_2\text{Cl}_5$	≈ 280	521	≈ 100	104	241	110	NCs	[146]
$\text{Cs}_3\text{Cu}_2\text{Cl}_5$	≈ 285	527	48.7	≈ 100	242	135.97	NCs	[145]
$\text{Cs}_3\text{Cu}_2\text{Cl}_5$	282	520	46.2	106	238	95.79	NCs	[153]
$\text{Cs}_3\text{Cu}_2\text{Cl}_5$	320	515	91.3	195	195	112.4	Powders	[177]
$\text{Cs}_3\text{Cu}_2\text{Cl}_5$	310	510	≈ 100	92	200	≈ 0.002	Crystals	[194]
$\text{Cs}_3\text{Cu}_2\text{Cl}_5$	310	≈ 525	60	102	≈ 215	–	Powders	[184]
$\text{Cs}_3\text{Cu}_2(\text{Cl}_{0.75}\text{Br}_{0.25})_5$	≈ 280	516	10	≈ 90	≈ 236	–	Films	[51]
$\text{Cs}_3\text{Cu}_2(\text{Cl}_{0.5}\text{Br}_{0.5})_5$	≈ 260	470	3.6	≈ 90	≈ 210	–	Films	[51]
$\text{Cs}_3\text{Cu}_2(\text{Cl}_{0.25}\text{Br}_{0.75})_5$	≈ 275	464	3.2	≈ 90	≈ 189	–	Films	[51]
$\text{Cs}_3\text{Cu}_2\text{Br}_5$	≈ 260	455	14	≈ 80	≈ 195	–	Films	[51]
$\text{Cs}_3\text{Cu}_2\text{Br}_5$	293	≈ 460	10	73	167	–	Powders	[184]
$\text{Cs}_3\text{Cu}_2\text{Br}_5$	≈ 260	458	20	82	≈ 198	–	NCs	[146]
$\text{Cs}_3\text{Cu}_2\text{Br}_5$	267	495	3.9	101	228	16.36	NCs	[153]
$\text{Cs}_3\text{Cu}_2\text{Br}_5$	–	454	18.3	≈ 80	≈ 190	≈ 0.005	NCs	[139]
$\text{Cs}_3\text{Cu}_2\text{Br}_5$	≈ 264	461	16.9	≈ 80	197	14.12	NCs	[145]
$\text{Cs}_3\text{Cu}_2(\text{Br}_{0.75}\text{I}_{0.25})_5$	≈ 250	456	11	≈ 90	≈ 206	–	Films	[51]
$\text{Cs}_3\text{Cu}_2(\text{Br}_{0.5}\text{I}_{0.5})_5$	≈ 250	452	15	≈ 90	≈ 202	–	Films	[51]
$\text{Cs}_3\text{Cu}_2(\text{Br}_{0.25}\text{I}_{0.75})_5$	≈ 260	456	11	≈ 90	≈ 196	–	Films	[51]

This article is protected by copyright. All rights reserved.

$\text{Cs}_3\text{Cu}_2\text{Br}_{3.75}\text{I}_{1.25}$	293	456	53.8	85	162	–	Powders	[43]
$\text{Cs}_3\text{Cu}_2\text{Br}_{2.5}\text{I}_{2.5}$	294	453	55.2	89	159	–	Powders	[43]
$\text{Cs}_3\text{Cu}_2\text{Br}_{1.25}\text{I}_{3.75}$	300	447	60.4	93	147	–	Powders	[43]
$\text{Cs}_3\text{Cu}_2\text{I}_5$	≈310	442	42	≈80	≈132	–	Films	[51]
$\text{Cs}_3\text{Cu}_2\text{I}_5$	310	≈440	62	80	130	–	Powders	[184]
$\text{Cs}_3\text{Cu}_2\text{I}_5$	≈309	≈443	98.7	99	≈134	–	Powders	[43]
$\text{Cs}_3\text{Cu}_2\text{I}_5$	290	445	91.2	75	141	0.46	SCs	[38]
$\text{Cs}_3\text{Cu}_2\text{I}_5$	≈310	442	89	≈80	≈132	≈0.98	Crystals	[36]
$\text{Cs}_3\text{Cu}_2\text{I}_5$	330	443	≈100	85	103	0.99	SCs	[82]
$\text{Cs}_3\text{Cu}_2\text{I}_5$	290	445	62.1	75	141	0.46	Films	[38]
$\text{Cs}_3\text{Cu}_2\text{I}_5$	285	441	58	70	156	0.84	Films	[104]
$\text{Cs}_3\text{Cu}_2\text{I}_5$	≈297	445	87	≈63	≈148	–	NCs	[140]
$\text{Cs}_3\text{Cu}_2\text{I}_5$	284	445	73.7	80	161	1.92	NCs	[153]
$\text{Cs}_3\text{Cu}_2\text{I}_5$	297	441	67	≈80	≈144	1.2	NCs	[139]
$\text{Cs}_3\text{Cu}_2\text{I}_5$	≈295	443	30	80	148	–	NCs	[146]
$\text{Cs}_5\text{Cu}_3\text{Cl}_6\text{I}_2$	≈270	462	95	95	191	40	Films	[56]
$\text{Cs}_5\text{Cu}_3\text{Cl}_6\text{I}_2$	297	464	73.7	86	186	40	NCs	[57]
K_2CuCl_3	284	386	98.8	52	102	10.8	SCs	[130]
K_2CuCl_3	291	392	96.6	54	101	12.97	Powders	[55]
K_2CuCl_3	265	385	90	53	120	–	Powders	[56]
K_2CuBr_3	296	388	55	54	92	–	Powders	[55]
Rb_2CuCl_3	300	400	≈100	47	100	12.21	Powders	[54]

This article is protected by copyright. All rights reserved.

Rb ₂ CuCl ₃	286	397	99.4	50.2	111	11.3	SCs	[121]
Rb ₂ CuCl ₃	285	400	49	52	115	9.9	NCs	[108]
Rb ₂ CuBr ₃	300	385	98.6	≈55	85	41.4	Crystals	[90]
Rb ₂ CuBr ₃	295	386	64	54	91	–	Powders	[54]
Rb ₂ CuBr ₃	302	390	20	54	88	–	Powders	[184]
Rb ₂ CuBr ₃	292	387	100	50	95	46.7	NCs	[108]
KCB-DMSO	382	670	74.8	151	288	21	Powders	[116]
RCB-DMSO	396	686	74.5	166	290	19	Powders	[116]
MA ₂ CuCl ₃	310	≈570	97	≈175	200	50.45	SCs	[77]
PEA ₄ Cu ₄ I ₄	≈350	632	25.7	144.8	282	11	SCs	[62]
(Gua) ₃ Cu ₂ I ₅	324	481	96	125	156	1.98	SCs	[63]
(C ₈ H ₂₀ N) ₂ Cu ₂ Br ₄	305	468	99.7	≈70	145	56	SCs	[67]
(TBA)CuCl ₂	286	510	92.8	86	224	28.7	SCs	[73]
(TBA)CuBr ₂	289	498	80.5	102	209	232.1	SCs	[73]
(C ₄ H ₉) ₄ NCuCl ₂	282	508	82	86	226	28.9	SCs	[92]
(DTA) ₂ Cu ₂ I ₄	320	≈540	60	≈150	210	1.84	SCs	[69]
(PTMA) ₃ Cu ₃ I ₆	358	614	80.3	160	257	2.88	SCs	[72]

6. Stability of TCHs

Stability plays an important role for the future actual applications of TCHs. In general, the TCHs require to surmount miscellaneous environmental conditions (such as heat, UV light irradiation, oxygen, and moisture) by instituting the strategies to tailor synthesis methods and optimize device architectures.^[211–216] Despite most TCH materials present enhanced stability compared to the lead-based perovskites, the stability issue of TCHs is still an ongoing challenge due to their ionic properties similar to perovskites.^[140,142] Recently, many research groups have experimentally and theoretically

This article is protected by copyright. All rights reserved.

studied the influence of environmental conditions on the structural and optical characters of TCHs, and many methods including surface passivation and ion doping, have been developed to surmount the stability troubles of TCHs. In this section, we will introduce the previous reports about the inherent stability of various TCHs, and critically review the key strategies to enhance the stability of TCHs.

6.1. Inherent Stability

As discussed above, most TCHs are characterized by the low-dimensional crystal structure, giving rise to strong copper-halide ionic bond and stable structure configurations, which is superior to traditional lead-based perovskites.^[56] Some theoretical work has shown that the decomposition energy and diffusion barrier of intrinsic defect in TCHs are significantly higher than those in lead-halide counterparts, indicating that TCHs have improved thermodynamic and chemical stability.^[180] For instance, Han et al. found that the structure integrity of $\text{Cs}_3\text{Cu}_2\text{I}_5$ NCs could be maintained after exposure in ambient conditions for two months.^[139] Besides, they studied the thermal stability of $\text{Cs}_3\text{Cu}_2\text{I}_5$ NCs by thermo gravimetric analysis from 40 to 1000 °C under nitrogen environment. The results reveal that there is a slight weight loss at around 250 °C, which could be ascribed to the decomposition of organic ligands. Surprisingly, at a high temperature of 600 °C, a large weight loss occurs, clearly confirming an excellent thermal stability of $\text{Cs}_3\text{Cu}_2\text{I}_5$ NCs. Our group demonstrated that the $\text{Cs}_3\text{Cu}_2\text{I}_5$ NCs exhibit outstanding environmental stability without any protection and encapsulation against moisture and oxygen in air ambient (293 K, 40% humidity) for 35 days.^[140] Theoretical calculation shows that no negative frequency in the phonon bands were observed, which verifies the kinetic stability of $\text{Cs}_3\text{Cu}_2\text{I}_5$. Moreover, the calculated low potential energy fluctuation and positive enthalpy manifest the favourable thermodynamic stability of such materials. Note that unlike lead-halide perovskite with diversified halide vacancies as the inherent defects, Cu vacancy (V_{Cu}) owns the lowest defect formation energy in $\text{Cs}_3\text{Cu}_2\text{I}_5$, thus the non-diffusion of V_{Cu} in $[\text{Cu}_2\text{I}_5]^{3-}$ clusters may support to the powerful stability of $\text{Cs}_3\text{Cu}_2\text{I}_5$. In another work, after ten successive heating/cooling PL test, the PL intensity of $\text{Cs}_3\text{Cu}_2\text{I}_5$ films could be maintained effectually (**Figure 10a**), with unchanged spectral shape and peak position, much better than the conventional lead-halide perovskites.^[180] Also, the $\text{Cs}_3\text{Cu}_2\text{I}_5$ films have been demonstrated to possess neat ambient stability without requiring any encapsulation, which is confirmed by the good structural integrity of $\text{Cs}_3\text{Cu}_2\text{I}_5$ films after 28-day storage (**Figure 10b**). Analogously, for yellow-emitting CsCu_2I_3 films, a teeny emission attenuation was produced after aggressive thermal cycling test (20–100–20 °C), showing a

This article is protected by copyright. All rights reserved.

superior tolerance against PL quenching (Figure 10c).^[88] After a 100-day storage in atmospheric environment, the original PL intensity of CsCu₂I₃ films could be nearly reserved with only a tiny attenuation of ≈4% (Figure 10d). The inherent excellent stability of TCHs discussed above endows them with great perspectives in optoelectronic fields, which would be discussed in the next section. Nowadays, the research on the stability of TCHs mainly focuses on the single-halogen systems, thus the migration of halides is not as serious as that of mixed halide perovskites. However, the spectral stability of TCHs under working condition still needs further investigations, especially in the external electric fields, strong irradiation, and moisture environments.

6.2. Strategies to Improve Stability

Although the stability of the TCHs is reported to be better than the Pb-halide counterparts, they are still do not meet commercial requirements.^[26] Hence, many strategies have been explored to improve the stability of TCHs through chemical and physical methods. As an example, the chlorine-containing Cs₃Cu₂Cl₅ NCs suffer stability trouble due to the oxidation of Cu⁺ to Cu²⁺. Zang et al. proposed a facile SiO_x coating strategy to synthesize monodisperse Cs₃Cu₂Cl₅@SiO_x NCs, which show dramatically enhanced stability against destruction by thermal and water.^[141] More specifically, under a continuous heating at 80 °C, the PL intensity of Cs₃Cu₂Cl₅@SiO_x NCs maintains 57% of the initial value after 18 days, while only 10% of the primordial value maintains for the pristine NCs. When adding water to the NCs, an emission decay of 45% for Cs₃Cu₂Cl₅@SiO_x NCs was observed after 100 min. In contrast, the emission performance of pristine NCs decays to 17% of their initial value even with a much shorter soak time of 60 min. Further studies show that the decomposition and oxidation are considered to be the dominating reason for the PL quenching. On the contrary, due to the protective effect of SiO_x shell, the decomposition and oxidation in Cs₃Cu₂Cl₅@SiO_x NCs are inhibited, leading to a significantly improved stability. Similarly, Cao et al. encapsulated Cs₃Cu₂I₅ NCs by SiO₂ through extra water treatments to crystalize Janus nanostructures.^[142] Figure 10e shows the transmission electron microscopy image of the resulting Janus Cs₃Cu₂I₅@SiO₂ NCs, in which Cs₃Cu₂I₅ and SiO₂ possess the average sizes of 15 and 12.5 nm, respectively. In the thermal stability evaluation, the PL intensity of control Cs₃Cu₂I₅ NCs reduces sharply to 28% from 30 to 100 °C, and only 87% of initial value recovered when cooling to 30 °C. For Janus Cs₃Cu₂I₅@SiO₂ NCs, above 50% of their initial PL intensity remains at 100 °C, and the intensity can revive to 124% after cooling process. Such excellent thermal tolerance can be reached in five heating/cooling cycles (Figure 10f,g),

which may be attributed to the self-structuring healing given by the decoration of SiO₂ during the heating process.

Doping could improve the short-range ordering of the lattice and strengthen the combination with the halogen, which has demonstrated to be a resultful method to improve the stability of materials.^[97] Such doping enhancement mechanism could also be available for TCHs. Chen and colleagues reported that the Cd-doped Cs₃Cu₂I₅ can maintain over 80% and 70% the initial PL intensity in ambient condition and under UV light irradiation at least 15 days, respectively.^[207] Similar stability improvements also exist on Mn-doped Cs₃Cu₂I₅, as revealed by Zeng's report.^[97] From their observation, 71% of the radioluminescence (RL) intensity could be remained for Mn-doped Cs₃Cu₂I₅, while the undoped counterpart shows a noticeable emission decay of 92.5% at 433 K (Figure 10h). Even after five cycles temperature measurement for 25 h, the RL performance of Mn-doped Cs₃Cu₂I₅ can be sustained effectively, as shown in Figure 10i. Moreover, more than 95% and 86% of the original RL intensities were remained after an accumulated X-ray radiation dose of ≈2590 Gy at RT and 333 K, respectively, which represents the strongest thermal stability among the lead-free metal halides (Figure 10j). In addition, they stored the samples in air ambient without protection for 2 months, and observed that the crystal structure and RL spectra have almost no change (Figure 10k), showing a robust environmental stability. The enhanced stability may be due to the stronger chemical bonding between Cu⁺ and I⁻ ion after Mn doping, which voluntarily help to stabilize I⁻ anion and Cu⁺ cation by inhibiting the migration of these ions and suppress Cu⁺ from oxidizing into Cu²⁺. All these evidences suggest that doping can support the improved stability of TCHs, which is superior to their undoped counterparts. Thus, we believe that an interesting research direction will be the development of effective doping strategies of TCHs for enhanced stability.

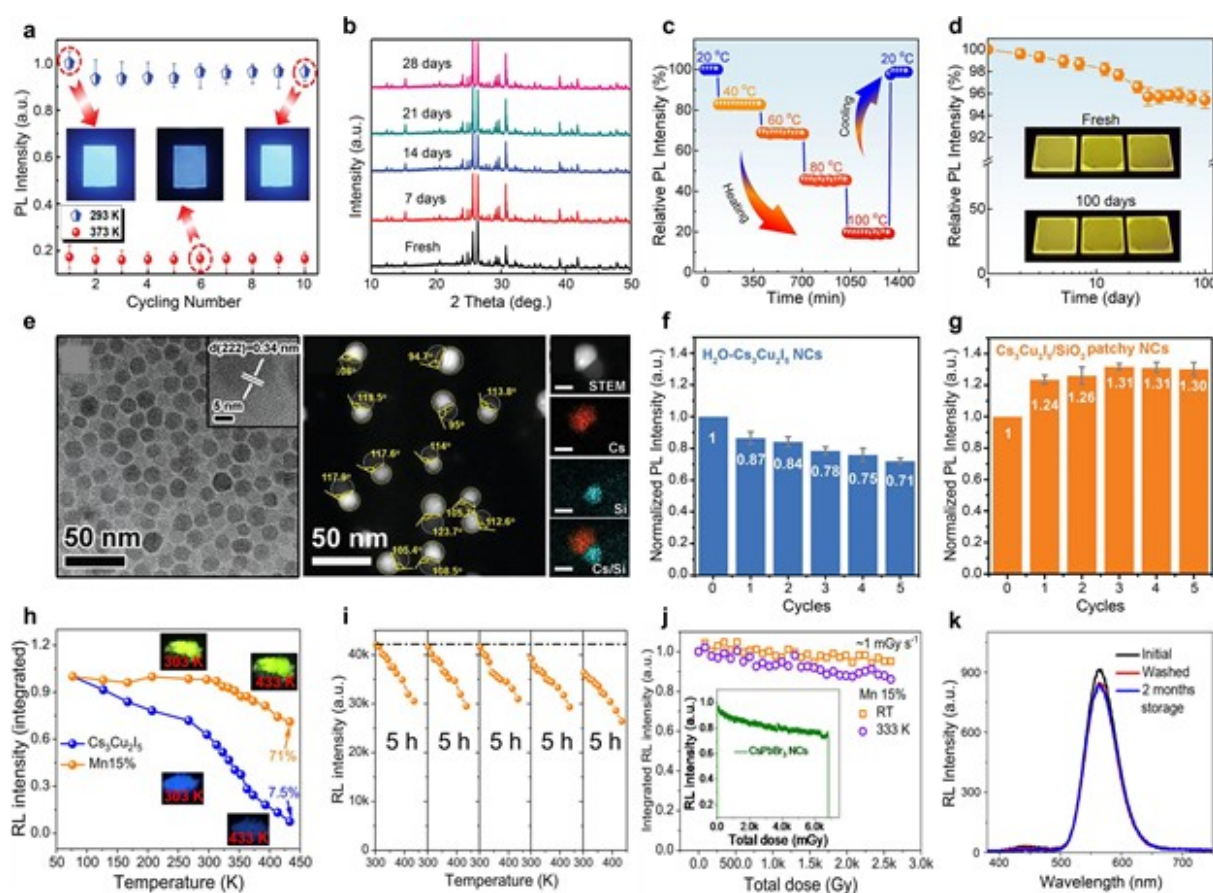


Figure 10. Stability analysis of TCHs. a) Thermal stability measurements of $\text{Cs}_3\text{Cu}_2\text{I}_5$ films. b) XRD variation of $\text{Cs}_3\text{Cu}_2\text{I}_5$ films at different storage time in atmospheric environment. (a,b) Reproduced with permission.^[180] Copyright 2020, Royal Society of Chemistry. c) Thermal stability measurements of CsCu_2I_3 films. d) Emission intensity variation of CsCu_2I_3 films at different storage time. (c,d) Reproduced with permission.^[88] Copyright 2020, American Chemical Society. e) TEM images and elemental mapping distribution of $\text{Cs}_3\text{Cu}_2\text{I}_5/\text{SiO}_2$ NCs. PL intensity of f) water-treated $\text{Cs}_3\text{Cu}_2\text{I}_5$ NCs and g) $\text{Cs}_3\text{Cu}_2\text{I}_5/\text{SiO}_2$ patchy NCs in five heating/cooling cycles. (e–g) Reproduced with permission.^[142] Copyright 2022, Wiley-VCH. h) RL intensity of $\text{Cs}_3\text{Cu}_2\text{I}_5$ and Mn^{2+} -doped $\text{Cs}_3\text{Cu}_2\text{I}_5$ at different temperature. i) Heating/cooling cycles and j) long-term stability at RT and 333 K. k) RL spectra of as-prepared, washed and irradiated Mn^{2+} -doped sample (15%). (h–k) Reproduced with permission.^[97] Copyright 2021, Springer Nature.

7. Optoelectronic Applications of TCHs

This article is protected by copyright. All rights reserved.

As we discussed in above sections, a broad range of TCHs demonstrate attractive characters for optoelectronic devices.^[217–234] Although the most efficient devices still employ lead-containing perovskites, the issue of lead-toxic is driving the development of novel TCHs. In this section, we will discuss the potential optoelectronic devices based on the newly-emerging TCHs, focusing on the phosphor-converted WLEDs, electroluminescent LEDs, anti-counterfeiting, X-ray scintillators, photodetectors, sensors, and memristors. We aim to highlight the current challenges and propose feasible approaches for future development.

7.1. Phosphor-Converted WLEDs

The phosphor-converted WLEDs remain to be a leading position in solid-state lighting industries because of their high luminous efficiency, long operating time, and simple fabrication.^[29] A proverbial and commercial technique of WLEDs configuration is to combine the LED chips with the down-conversion phosphors, as shown in **Figure 11a**. Benefitting from their broadband emission, good stability, and superior PLQY, flourishing TCHs own mighty competitive strength in the field of phosphor-converted WLEDs. In 2018, Hosono and co-workers achieved a brightly white emission through mixing blue-emitting $\text{Cs}_3\text{Cu}_2\text{I}_5$ and commercial yellow-emitting phosphors under UV chip excitation.^[38] By varying the mixing ratio, the CIE color coordinate could be linearly regulated from (0.15, 0.09) to (0.44, 0.48), as shown in Figure 11b,c. Compared to $\text{Cs}_3\text{Cu}_2\text{I}_5$, CsCu_2I_3 exhibits a wider emission range covering 430–780 nm with a larger Stokes shift, highlighting its potential as single-component white-light emitter. Besides, single-component white phosphors could simplify the device configuration and avert color alteration observed in multi-component phosphors. Using CsCu_2I_3 SCs as the white phosphors reported by Lin et al., a single-component WLED with a CIE color coordinate of (0.345, 0.364) and a correlated color temperature(CCT) of 5035 K was demonstrated.^[81] Moreover, the proposed WLEDs present a prominent operation stability in atmospheric environment, with only a $\approx 5\%$ luminous efficiency decay after a continuous operation for 750 min. Unfortunately, such single-component white phosphors suffer from a poor color-rendering index (CRI) that stands for the capacity of lighting source to reveal the color of object truly, which limit their applications in high-end lighting places. To enhance the CRI and reach a standard white-light emission, our group developed a novel two-component strategy by integrating the blue-emitting $\text{Cs}_3\text{Cu}_2\text{I}_5$ and yellow-emitting CsCu_2I_3 .^[35] The $\text{CsCu}_2\text{I}_3@ \text{Cs}_3\text{Cu}_2\text{I}_5$ composites with direct white-light emission were prepared by a facile one-step solution method. By controlling the proportion of $\text{Cs}_3\text{Cu}_2\text{I}_5$ and CsCu_2I_3 component, adjustable white light from cold- to warm-white emission with a CIE coordinate ranging

This article is protected by copyright. All rights reserved.

from (0.39, 0.43) to (0.25, 0.24) can be easily achieved (Figure 11d). Because both CsCu_2I_3 and $\text{Cs}_3\text{Cu}_2\text{I}_5$ are featured by the broadband emission, the hybrid emission spectrum is enough to cover a broad range, thus generating a record CRI of 91.6 (Figure 11e), which helps to create a healthy and comfortable lighting atmosphere, and meets the requirements of high-end color-critical applications, such as surgery, art galleries, jewelry, and photography. Therefore, such component regulation tactics of the cesium copper iodine compounds offers a controllable and practical strategy for realizing white light tuning, making it possible to meet daily variations in sunlight.^[122,193,195,204]

Despite the great progress in TCHs-based WLEDs, they are still in the initial stage with far more works anticipated to further enhance their performance. **Table 2** summarizes the device performance parameters of WLEDs from TCH emitters. One can observe a phenomenon that the luminous efficiency of such WLEDs is not always offered in the reported literatures. Generally, the luminous efficiency of WLEDs depends largely on the synergistic effect of the optical characters of phosphors and the selection of excitation source.^[29] Yet, most TCH materials own the optimal excitation wavelengths less than 360 nm, which cannot match the the primary output wavelength ranges of 390–450 nm for commercial $\text{Ga}_{1-x}\text{In}_x\text{N}$ excitation light source with high output efficiency.^[30] For the short-wavelength III-nitride chips with wavelength below 365 nm, their light output efficiency is reversely small, thus resulting in large efficiency losses. Therefore, future works can be directed toward the near-UV or blue-light-excitable TCH materials while maintaining high PLQYs. To effectively resolve this issue, computation-assisted combinatorial chemistry must be exploited and designed to seek dependable doping or alloying strategy of TCHs, perhaps various light absorption behavior with low excitation energy could be realized. In addition, the operation stability of TCH-based WLEDs has been significantly improved, but it is still much inferior to the stability of commercial WLEDs (100000 h; at 90% lumen maintenance).^[31] So, further stabilizing down-conversion TCH phosphors and preventing their decomposition, especially for the thermal-induced PL degradation, are highly required. In this regard, developing efficient thermal dissipation device configurations combined with commercial encapsulation technology will increase the working lifetime of the TCH-based WLEDs.

Visible Light Communication (VLC) based on WLEDs is of possible practices in next-generation data communications due to its security, high energy efficiency, unregulated communication spectrum, and no radio frequency interferences.^[128] This is an emerging technology that employs WLEDs as light source for data transmission (Figure 11f). With tremendous advances of TCH materials in white

lightings, they are deemed as appropriate candidates for VLC applications. Recently, Zang et al. applied WLEDs from mixed $\text{Cs}_3\text{Cu}_2\text{Cl}_5$ and red phosphors in the VLC applications, in which the -3dB bandwidth of about 420 kHz and the data rate of 2.65 Mbit/s were achieved.^[122] To widen the bandwidth and improve the communication transmission rate of VLC, they used a $\text{CsCu}_2\text{I}_3@/\text{Cs}_3\text{Cu}_2\text{I}_5$ composite with high PLQY and short PL decay as the white sources in VLC. As a result, the communication data rate and -3 dB bandwidth of the VLC improve to 87.7 Mbit/s and 10.1 MHz , respectively (Figure 11g). Moreover, a high signal-to-noise ratio of more than 16 dB above the -3 dB bandwidth was obtained (Figure 11h). Figure 11i exhibits the resulting bit loading profiles, in which subcarriers in the low frequency region can be loaded up to 7 bit/s/Hz , which means the potential applications of TCH-based WLED in VLC.

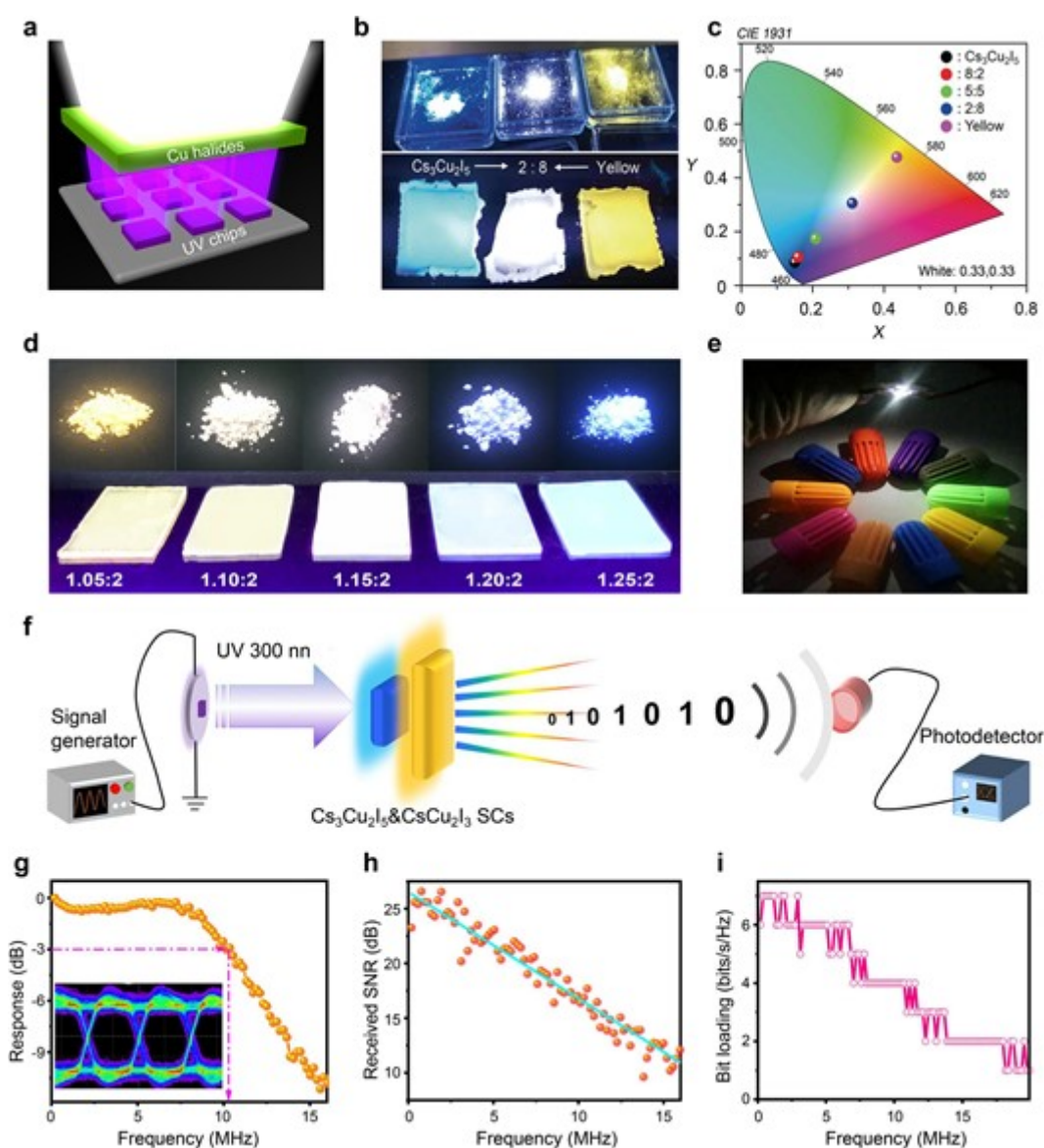


Figure 11. Phosphor-converted WLEDs based on TCHs. a) Illustration of the phosphor-converted WLEDs. b) Photographs of $\text{Cs}_3\text{Cu}_2\text{I}_5$, yellow-emitting phosphor, and their mixtures under UV light irradiation. c) CIE color coordination of the powder mixtures. (b,c) Reproduced with permission.^[38] Copyright 2018, Wiley-VCH. d) Photographs of powders and films of the $\text{CsCu}_2\text{I}_3@/\text{Cs}_3\text{Cu}_2\text{I}_5$ composites with various CsI/CuI molar ratios under UV light excitation. e) A typical photograph of phosphor-converted WLEDs from $\text{CsCu}_2\text{I}_3@/\text{Cs}_3\text{Cu}_2\text{I}_5$ composites. (d,e) Reproduced with permission.^[35] Copyright 2021, Wiley-VCH. f) Schematic illustration of the visible light communication system by WLEDs. g) electrical-optical-electrical frequency responses, h) obtained

This article is protected by copyright. All rights reserved.

signal-to-noise ratios, and i) bit loading profiles employing orthogonal frequency division multiplexing modulation. (f–i) Reproduced with permission.^[122] Copyright 2021, Wiley-VCH.

Table 2. Summary of the device performances of the phosphor-converted WLEDs.

Active Layer	Pump source	CIE (x, y)	CCT (K)	CRI	Lifetime (h)	Ref.
$[(C_3H_7)_4N]_2Cu_2I_4$	UV (315 nm)	(0.33, 0.35)	5684	92.2	>5	[68]
$(C_{16}H_{36}N)CuI_2$	UV (275 nm)	(0.28, 0.30)	–	78	–	[64]
Cs–Cu–I	UV (310 nm)	(0.33, 0.33)	5495	–	>100	[117]
KCB-DMSO- $Cs_3Cu_2Br_5$ - $Cs_3Cu_2Cl_5$	UV (310 nm)	(0.33, 0.34)	5800	97	–	[116]
$Cs_3Cu_2Br_5$ -red phosphor	UV (310 nm)	(0.30, 0.30)	–	97.5	–	[87]
$Cs_3Cu_2Cl_5$ - $CsCu_2Cl_3$	UV (290 nm)	(0.33, 0.33)	5285	94	>60	[173]
$CsCu_2I_3@Cs_3Cu_2I_5$	UV (310 nm)	(0.33, 0.33)	8477	91.6	–	[35]
(TPA) CuI_2	UV (365 nm)	(0.31, 0.33)	6574	91.3	–	[94]
$Cs_3Cu_2Cl_5$ - $CaAlSiN_3:Eu^{2+}$	UV (310 nm)	(0.34, 0.37)	5049	94	–	[141]
$Cs_3Cu_2Cl_5$ - $BaMgAl_{10}O_{17}:Eu^{2+}$ - $(Sr,Ca)AlSiN_3:Eu^{2+}$	UV (365 nm)	(0.35, 0.36)	4203	96	–	[188]
MA_2CuCl_3	UV (310 nm)	(0.44, 0.50)	3552	88	>1	[71]
$Cs_5Cu_3Cl_7I$ - $CsCu_2I_3$	UV (310nm)	(0.33, 0.39)	5430	77.8	–	[59]
$Cs_5Cu_3Cl_7I$ - $CaAlSiN_3:Eu^{2+}$	UV (310 nm)	(0.34, 0.36)	5033	89.2	–	[59]
$CsCu_2I_3@Cs_3Cu_2I_5$	UV (307 nm)	(0.29, 0.31)	–	–	–	[138]
$CsCu_2I_3$ - $Cs_3Cu_2I_5$	UV (300 nm)	(0.33, 0.33)	5436	91	>1350	[122]
$Cs_3Cu_2I_5:Mn^{2+}$ -BAM: Eu^{2+}	UV (385 nm)	(0.30, 0.35)	6828	77.9	–	[209]
$CsCu_2I_3$ - $Cs_3Cu_2I_5$	UV (280 nm)	(0.35, 0.35)	–	–	–	[203]
$CsCu_2I_3$ - $Cs_3Cu_2I_5$	UV (310 nm)	(0.32, 0.33)	5877	88.4	>100	[195]
$CsCu_2I_3@anthracene$	UV (310 nm)	(0.31, 0.31)	6718	83	>60	[50]
(DTA) $_2Cu_2I_4$ - $Cs_3Cu_2I_5$	UV (310 nm)	(0.34, 0.44)	–	85.7	>6	[69]
$Cs_3Cu_2I_5$ - $(Ba,Sr)_2SiO_4:Eu^{2+}$ - $CaAlSiN_3:Eu^{2+}$	UV (310 nm)	(0.34, 0.34)	5075	90.2	–	[200]

This article is protected by copyright. All rights reserved.

CsCu ₂ I ₃ @Cs ₃ Cu ₂ I ₅	UV (365 nm)	(0.32, 0.33)	6109	92	>40	[204]
Cs ₃ Cu ₂ I ₅ -(Sr,Ba) ₂ SiO ₄ :Eu	UV (280 nm)	(0.30, 0.33)	–	–	>300	[137]
Cs ₃ Cu ₂ I ₃ -BaMgAl ₁₀ O ₁₇ :Eu ²⁺	UV (365 nm)	(0.27, 0.31)	10000	–	>150	[126]
Cs ₃ Cu ₂ I ₅ -Cs ₃ Cu ₂ Cl ₅	UV (310 nm)	(0.27, 0.38)	–	–	–	[172]
CsCu ₂ I ₃ -Cs ₃ Cu ₂ I ₅	UV (310 nm)	(0.35, 0.35)	4798	–	>36	[217]

7.2. Electroluminescent LEDs

Another attractive application of highly emitting TCHs with eco-friendly features is electroluminescence (EL) based LED.^[31] The working mechanism and important parameters of EL-based LEDs need to be specifically considered. Generally, a standard LED is composed of a cathode, an n-type electron transport layer (ETL), an emitter layer (EML), p-type hole transport layer (HTL), and an anode.^[30] Under a forward voltage, the holes and electrons will be injected respectively from HTLs and ETLs, and then the radiative recombination occurs to emit photons at the EML, as seen in **Figure 12a**. The energy level alignments of typical materials used as HTLs, TCH-based EMLs, and ETLs are given in Figure 12b. The device performances of LEDs are usually determined by the following key parameters, such as turn-on voltage (V_{on}), luminance (L), external quantum efficiency (EQE), current efficiency (CE), and lifetime.^[20] As the most important indicator of energy conversion efficiency of LED, EQE is defined as the proportion of the number of photons of LEDs to the injected electrons, which is always less than 1.0.^[23] It can be expressed by the following equation:^[229]

$$EQE = IQE \times \eta_o = \eta_I \times \eta_R \times \eta_o \quad (3)$$

where IQE refers to the internal quantum efficiency, η_o represents the optical extraction efficiency, η_I is the charge injection efficiency, and η_R is the exciton radiative recombination efficiency.^[30] The IQE is deemed as the ratios of the number of photons generated by emitters to the number of injected electrons, which is equal to the product of η_I and η_R .^[27] TCH emitters own the suitable optoelectronic properties including high PLQY and ideal η_R factor, endowing them a new-generation candidate for fabricating LEDs. In this connection, there are many representative works that worthy of our attention, as summarized in **Table 3**.

In 2018, Hosono and co-workers fabricated blue-emitting LEDs based on Cs₃Cu₂I₅ films with an inverted device structure of ITO/ZSO/Cs₃Cu₂I₅/NPD/MoO_x/Ag.^[38] This device has a relatively high V_{on} of ≈ 6.0 V and the peak luminance could realize ≈ 10 cd m⁻². They analyzed that the poor device

performances can be ascribed to the non-ideal energy alignments of the bands, confirmed by the large ionization potential of ≈ 6.5 eV and small electron affinity of ≈ 2.7 eV for the $\text{Cs}_3\text{Cu}_2\text{I}_5$ emitter. Since then, many related work on optimization approaches have been carried out to fabricate better-performing LEDs. Our group reported the deep-blue LEDs with better performances, with the EQE and maximum luminance reached 1.12% and 262.6 cd m^{-2} , respectively, by employing efficient $\text{Cs}_3\text{Cu}_2\text{I}_5$ NCs as the emitter and selecting appropriate HTLs and ETLs.^[140] The fabricated LED produces a bright deep-blue EL located at 445 nm, corresponding to a CIE color coordinate at (0.16, 0.07), which meets the standard blue NTSC. Surprisingly, such LED demonstrates a long-term operation stability with record half-lifetimes of ≈ 108 h (Figure 12c), which is far superior to most of their Pb-based counterparts. The exceptional stability may result from the intrinsic resistance of the $\text{Cs}_3\text{Cu}_2\text{I}_5$ NCs against the oxygen/moisture and heat recession, as well as imperceptible electrical-field-induced ion migration. Another report from Wu's group reported the fabrication of deep-blue LEDs from $\text{Cs}_3\text{Cu}_2\text{I}_5$ films, where all active layers were prepared by the thermal evaporation method.^[104] The corresponding devices exhibit a relatively low V_{on} of 3.6 V with an EQE of 0.1% and a peak luminance of $\approx 70 \text{ cd m}^{-2}$. Although the device performances remain highly unsatisfactory and need to be improved, this study lays the foundation for manufacturing LEDs based on TCHs through thermal evaporation technique.

In the past three years, electrically driven LEDs based on CsCu_2I_3 material have also developed in full swing. Considering the intrinsic color instability and lead-toxicity of lead-based mixed-halide yellow LEDs, our group successfully fabricated highly stable yellow LEDs using CsCu_2I_3 films as the emitters.^[88] With this strategy, broadband yellow EL spectra at ≈ 550 nm were achieved with peak EQE and luminance of 0.17% and 47.5 cd m^{-2} , respectively (Figure 12d). More importantly, the resulting device demonstrates good working stability operating at RT and high temperature of 60°C , exhibiting the half-lifetimes of 310 and 130 min, respectively, which mainly profits from the significant stability of CsCu_2I_3 against heat and moisture/oxygen. Note that the reduced lifetime of devices at 60°C may be caused by the rised potential of thermal-induced non-radiative recombination. Subsequently, CsCu_2I_3 -based yellow LEDs with a relatively low V_{on} of 2.9 V and a maximum luminance of 10 cd m^{-2} were fabricated through a thermal evaporation technique by Liu and co-workers^[165] Experimental and theoretical investigations have notarized that CsCu_2I_3 possesses a large bandgap (> 3.5 eV) along with a deep valence band level (> 6.0 eV), which results in wide carrier injection barriers with unmatched energy band alignment. Therefore, some higher requirements are

This article is protected by copyright. All rights reserved.

proposed for the device configuration design of balanced carrier injection process. In a recent study, a stepwise “energy ladder” multilayer of PEDOT:PSS/poly[N,N’-bis(4-butylphenyl)-N,N’-bisphenylbenzidine] (Poly-TPD)/poly(9-vinylcarbazole) (PVK) as HTLs to enhance the hole injection and charge carrier recombination was proposed by Ma et al., and an enhanced performance of CsCu₂I₃-based LEDs was achieved.^[154] Specifically, the optimized LED achieves a peak luminance of 219.6 cd m⁻², a maximum EQE of 0.49%, and a half-lifetime of 48.5 min.

Besides, the intrinsic broadband emission of TCHs provides an additional possibility for realizing direct electroluminescent WLEDs. In this connection, there are a few representative reports that deserve discussions herein. For instance, Zhu’s group designed WLEDs made of the mixed-phase composite films of CsCu₂I₃ and Cs₃Cu₂I₅ by the solvent treatment.^[193] In this system, individual luminescence from coexisting yellow-emitting CsCu₂I₃ and blue-emitting Cs₃Cu₂I₅ would not affect each other. The as-fabricated WLEDs demonstrated a small V_{on} of 2.9 V, showing two EL peaks at 460 and 571 nm with a peak luminance of 352.3 cd m⁻². However, the peak EQE of device reaches only 0.053%, which may be due to the carrier trapped defects in the active emitter. Analogously, by assembling two broadband emitting STEs from CsCu₂I₃ and Cs₃Cu₂I₅, our group reported the cold/warm tunable WLEDs based on the CsCu₂I₃@Cs₃Cu₂I₅ composites films.^[35] By adjusting the ratio of two phases, a battery of white light devices ranging from cold-white to pure-white to warm-white were achieved. Accordingly, the CIE color coordinate and CCT of three WLEDs were (0.28, 0.29)/9024 K, (0.32, 0.33)/6109 K, and (0.38, 0.42)/4264 K, respectively. What is more, the resulting WLEDs realize a record CRI of 91.6, an EQE of 0.15%, and a long half-lifetime of 238.5 min. Despite these efforts and advances, the above two reports are still based on the two-component strategy, which could not take into account both color stability and color rendering, especially under high bias voltages. Thus, a highly-promising method is to seek single-component emitters with broadband white light covering the entire visible spectra. Compared with the multicomponent WLEDs, such strategy not only vastly simplifies the device configuration but also addresses the self-absorption and color drift troubles. Lately, single-component warm WLEDs based on an ultrabroadband MA₂CuCl₃ emitter covering visible range from 400 to 800 nm were reported by Liu’s group.^[71] In their case, the suitable energy level structures were exploited, where 4,4’-bis(carbazol-9-yl)biphenyl (CBP)-incorporated PVK served as the HTL and electron blocking layer due to the suitable electron affinity and valence band position. The fabricated WLEDs produce a peak EQE of 0.035% and

luminance of 54 cd m^{-2} ; meanwhile, the devices possess a good EL spectra stability within a bias voltage range of 7–13 V (Figure 12e).

From the positive progresses discussed above, one can observe that the preliminary trials based on TCH emitters in electroluminescent LEDs are encouraging, as such emitters can concurrently resolve the lead toxicity and color instability of lead-halide perovskite LEDs. However, we have to admit that the EQE, luminance, and V_{on} of the above LEDs still lag behind that of lead-halide perovskites and are certainly far below the industrial requirements. In this regard, several strategies to enhance EL performance have recently been reported. For example, Wang et al. proposed an organic additive (Tween) modification strategy for high-performance WLEDs made of the mixed-phase CsCu_2I_3 and $\text{Cs}_3\text{Cu}_2\text{I}_5$ system.^[96] The authors found that the chemical interaction between the Cs^+ and Tween is the key to making efficient devices through multiple effects, including improved crystallinity, enhanced surface potential, promoted charge carrier injection, and suppressed defects of the active emitters. This strategy boosts the EQE of the proposed WLEDs to 3.1% with a high luminance of 1570 cd m^{-2} at a voltage of 5.4 V, as shown in Figure 12f. Ingeniously, against the shortcomings of serious defect-related non-radiative losses and inefficient charge transport characteristics of CsCu_2I_3 emitters, the concept of trap passivation and hole-injection promotion synergistic effects was put forward by our group.^[95] After the incorporation of PVK into CsCu_2I_3 , the Cu_{Cs} and Cu_{I} anti-site defects were greatly passivated, showing a significantly enhanced radiative recombination within the CsCu_2I_3 emitters. Meanwhile, the energy band alignment of CsCu_2I_3 emitter was well regulated to vastly promote the hole injection, and the hole transport capacity of the emitter was equally enhanced. Thanks to these synergistic roles, the resulting yellow LEDs deliver a peak EQE of 1.35% and a robust half-lifetime of 14.6 h (Figure 12g). By adopting a host–dopant strategy learned from organic LED by Seo et al.,^[151] the performance of CsCu_2I_3 -based LED was further improved to a higher level. The host–dopant active emitters composed of tri(m-pyridin-3-ylphenyl)benzene, 1,3,5-tris(3-pyridyl-3-phenyl)benzene (TmPyPB) host and CsCu_2I_3 dopant exhibit an enhanced PLQY of 84.8% and an elevated carrier radiative recombination rate of $3.38 \times 10^6 \text{ s}^{-1}$, which are 26 times and 20 times higher than those of the neat CsCu_2I_3 films, respectively. With the further improvement in charge transport balance employing the co-host systems, the resulting device reaches a record EQE of 7.4% and an operation lifetime of 20 h at the original luminance of 100 cd m^{-2} (Figure 12h). This breakthrough brings enormous confidence to achieve high-efficiency TCH-based LEDs. Logically, the strategy of using a host-dopant doping is promising for those TCH emitters, because these emitters usually suffer from

This article is protected by copyright. All rights reserved.

very poor charge transport abilities. Doping with an organic host with much higher carrier mobility can be considered as an effective way to overcome the limitation of these emitters. In this regard, this strategy in principle should be a general approach for the STEs materials beyond CsCu_2I_3 .

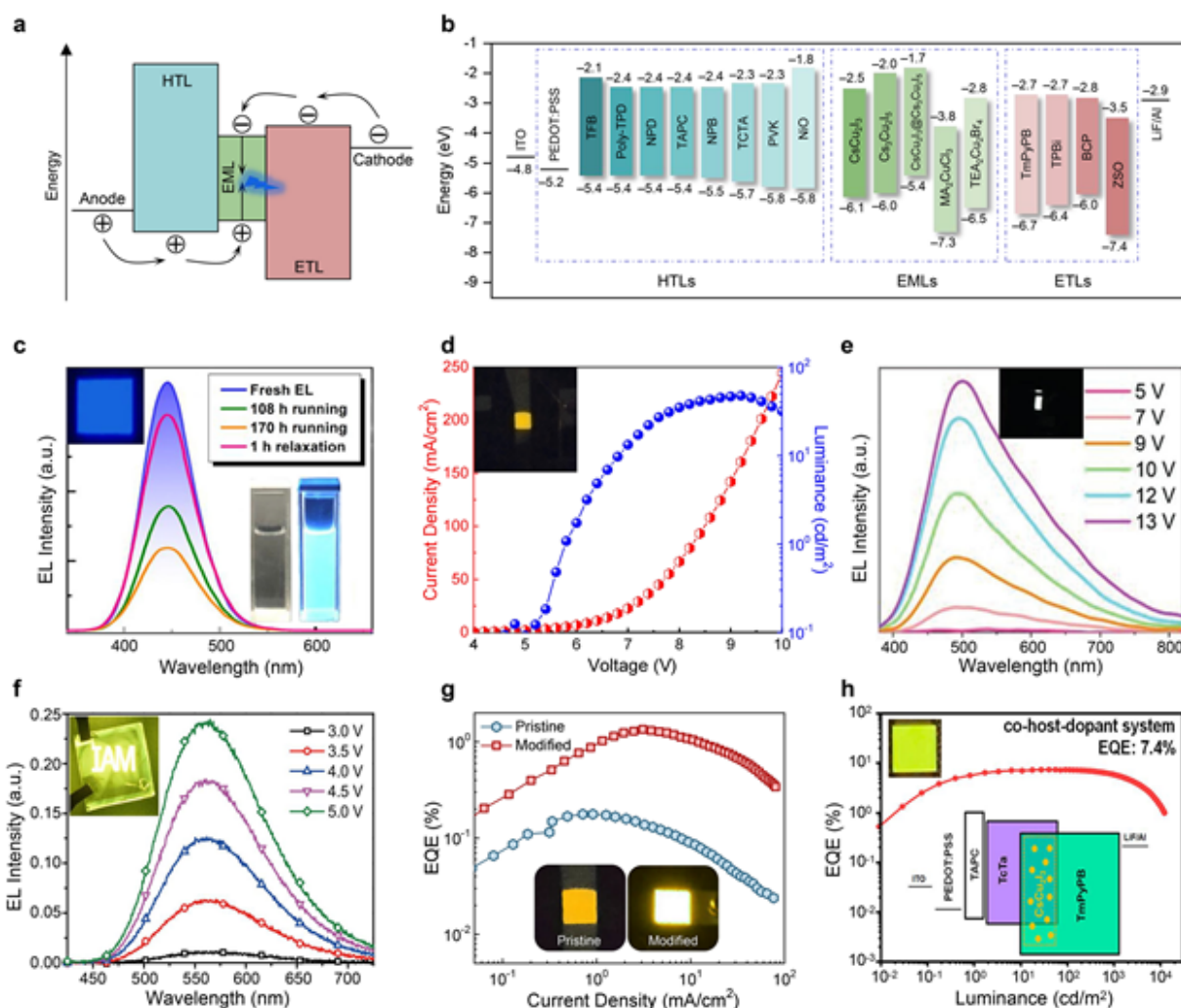


Figure 12. TCHs for electroluminescent LEDs. a) Schematic energy band diagram and working mechanisms of an electroluminescent LED. b) Energy levels for different HTLs, ETLs, and TCHs emitters. c) EL spectra of the $\text{Cs}_3\text{Cu}_2\text{I}_5$ NCs-based blue LED tested various aging conditions. (c) Reproduced with permission.^[140] Copyright 2020, American Chemical Society. d) $J-V-L$ curves of yellow LEDs from CsCu_2I_3 emitters. (d) Reproduced with permission.^[88] Copyright 2020, American Chemical Society. e) EL spectra of the MA_2CuCl_3 -based white LEDs under different voltages. (e) Reproduced with permission.^[71] Copyright 2022, Wiley-VCH. f) EL spectra of the Cs-Cu-I-based

This article is protected by copyright. All rights reserved.

white LEDs under different voltages. (f) Reproduced with permission.^[96] Copyright 2021, Springer Nature. g) EQE versus current density of the control and PVK-treated LEDs. (g) Reproduced with permission.^[95] Copyright 2022, Wiley-VCH. h) EQE versus luminance of the CsCu₂I₃-based yellow LEDs. (h) Reproduced with permission.^[151] Copyright 2021, American Chemical Society.

Figure 13a illustrates the development trends of electroluminescent LEDs based on TCH emitters since 2019, revealing that the EQE has increased markedly from less than 0.1% to more than 7% in just four years, which paints a bright future for lighting and display applications. Despite this, the performances of TCHs-based LEDs are still inferior to the well-developed lead-halide perovskites.^[30] The obvious disparities urge us to find out the underlying problems that limit the performance of LEDs. As discussed above, the EQE of LED is generally determined by the fraction of excitons for radiative recombination, charge injection efficiency and light outcoupling efficiency. Generally, the outcoupling efficiency is demonstrated to a theoretical efficiency of 20–30%, which leads to the theoretical limitation value of EQE to 20–30% for a standard LED. While, the current peak EQE of TCH-based devices is less than 10%, thus it allows us to set aside the effect from light outcoupling.^[229] Therefore, the dominating factors concerned herein should be the charge carrier injection efficiency and exciton radiative recombination. Based on the discussion of the above progresses, we reasonably inferred that the performance of device is mainly decided by multiple factors, such as PLQYs, non-radiative losses, and electrical properties of TCHs. Besides, a deeply understanding of the inherent mechanisms is also indispensable.^[95] Note that the above considerations are not independent for achieving efficient LEDs. For example, poor crystallization may lead to inferior film morphology with defects, further inhibiting charge carrier transport in emitter and inducing depressed PLQY.^[96] It should be mentioned that the poor electrical properties of TCH emitters are primarily responsible for inefficient LEDs due to the worse charge transport caused by the large effective carrier mass and the difficult charge injection (Figure 13b). In response to the above challenges, several directions toward high-efficiency TCHs-based LEDs are proposed: i) understanding the intrinsic properties of TCHs, ii) improving the radiative recombination of TCHs, iii) enhancing the electrical properties of the TCHs, and iv) optimizing the device architecture (Figure 13c). With these efforts, we firmly believe that the device performance of TCH-based LEDs is promised to get improved shortly.

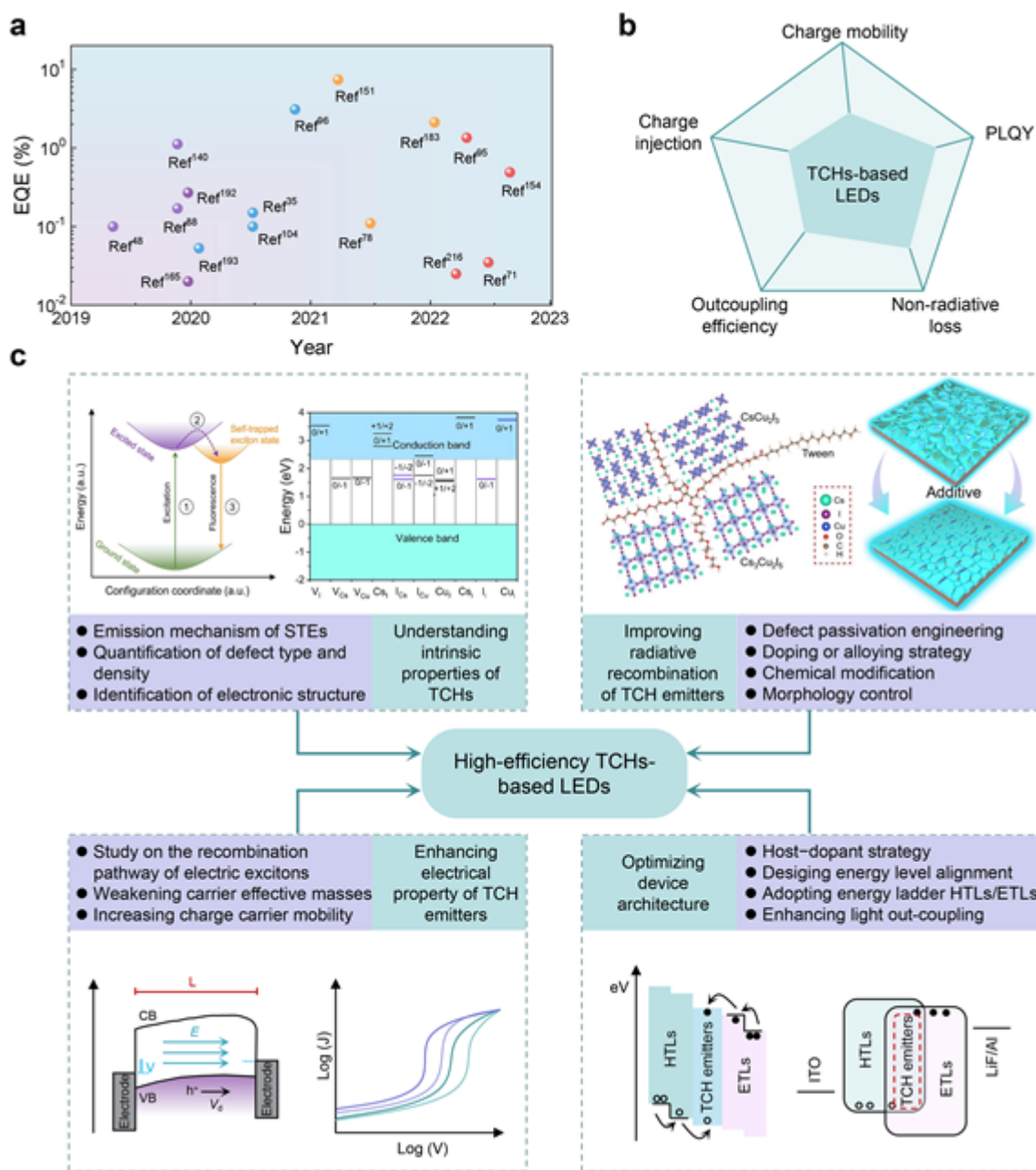


Figure 13. Current progress and possible improvement strategies of TCHs-based LEDs. a) EQE evolution of TCHs-based LEDs from 2019 to 2022. b) Radar diagram showing the challenges of LEDs based on TCHs. Dark green shadow indicates the strength of the property. c) Possible strategies for high-efficiency TCH-based LEDs, including understanding inherent characters of TCHs, improving radiative recombination of the TCHs, enhancing electrical property of the TCHs, and optimizing device architecture. The upper left image in (c) was reproduced with permission.^[80]

This article is protected by copyright. All rights reserved.

Copyright 2020, Springer Nature. The upper right image in (c) was reproduced with permission.^[96]

Copyright 2021, Springer Nature.

Table 3. Summary of the device performances of the electroluminescent LEDs based on the TCHs emitters.

EML	Device structures	λ_{\max}^a (nm)	FWHM (nm)	Lu^b (cd m^{-2})	EQE (%)	t_R^c (min)	Ref.
Cs ₃ Cu ₂ I ₅ films	ZSO/EML/NPD/MoO _x /Ag	440	≈70	10	–	–	[38]
Cs ₃ Cu ₂ I ₅ films	PEDOT:PSS:PFI/EML/TPBi/LiF/Al	436	≈75	140	0.27	–	[192]
Cs ₃ Cu ₂ I ₅ films	MoO ₃ /EML/LiF/HAT–CN/NPB/Al	≈438	58	70	0.1	–	[104]
Cs ₃ Cu ₂ I ₅ NCs	NiO/EML/TPBi/LiF/Al	≈445	≈70	263.2	1.12	6480@6.7 V	[140]
CsCu ₂ I ₃ films	PEDOT:PSS/poly-TPD/EML/TPBi/LiF/Al	550	≈100	47.5	0.17	310@6.0 V	[88]
CsCu ₂ I ₃ films	MoO ₃ /TAPC/EML/TmPyPB/LiF/Al	≈554	≈120	10	0.1	–	[48]
CsCu ₂ I ₃ films	NiO/EML/TPBi/LiF/Al	≈560	≈180	10	0.02	–	[165]
CsCu ₂ I ₃ films	PEDOT:PSS/TAPC/TCTA/EML/TmPyPB/LiF/Al	578	132	15879	7.4	1200@4.0 V	[151]
CsCu ₂ I ₃ films	PEDOT:PSS/poly-TPD/PVK/EML/TmPyPB/LiF/Al	550	≈100	357.8	1.35	876@3 mA cm ⁻²	[95]
CsCu ₂ I ₃ films	Al/MoO _x /TAPC/TCTA/EML/TmPyPB/LiF/MAA	593	59	14767	2.12	–	[183]
CsCu ₂ I ₃ films	PEDOT:PSS/poly-TPD/PVK/EML/TmPyPB/LiF/Al	≈550	≈100	219.6	0.49	48.5@4.5 V	[154]
CsCu ₂ I ₃ films	PEDOT:PSS/EML/TPBi/LiF/Al	≈600	≈245	29.3	0.025	–	[216]
CsCu ₂ I ₃ @Cs ₃ Cu ₂ I ₅ films	PEDOT:PSS/EML/TmPyPB/LiF/Al	440@565	121	1570	3.1	–	[96]
CsCu ₂ I ₃ @Cs ₃ Cu ₂ I ₅ films	PEDOT:PSS/poly-TPD/PVK/EML/TPBi/LiF/Al	446@550	85@115	145	0.15	238.5@7.0 V	[35]
CsCu ₂ I ₃ @Cs ₃ Cu ₂ I ₅	PEDOT:PSS/V–NPB/EML/SPPO13/LiF/Al	460@571	80@110	352.3	0.053	–	[193]

This article is protected by copyright. All rights reserved.

films								
MA ₂ CuCl ₃ films	PEDOT:PSS/PVK/EML/TPBi/LiF/Al	≈500	≈160	54	0.035	–		[71]
TEA ₂ Cu ₂ Br ₄ films	PEDOT:PSS/EML/TPBi/LiF/Al	432	92	85	0.11	1200@4.3 V		[78]

^{a)} λ_{\max} : Peak position; ^{b)}Lu: Luminance; ^{c)} t_R : Running time.

7.3. Anti-Counterfeiting

As we all know, counterfeiting poses a huge menace to the global economy and results in great economic losses to both society and individuals.^[42,136,178] Therefore, development of anti-counterfeiting technique is imminently required and certainly a worthwhile subject. In general, anti-counterfeiting is accomplished by verifying the true information, which can be either hidden or public.^[76] In the decoding process, the retrieved information can be represented by the fluorescent color and intensity in patterns that vary in both space and time domains. The key factor of anti-counterfeiting technique is the capacity to decrypt secretive information under especial condition, in which encoding material is important carriers carrying confidential information.^[42]

TCH materials with superior optical properties, convenient fabrication, and rich structural properties are expected to be explored as anti-counterfeiting candidates. For instance, Rogach and co-workers utilized the blue-emitting Cs₃Cu₂I₅ as the fluorescent inks to fabricate anti-counterfeiting patterns.^[36] **Figure 14a** shows the schematic process of drawing a lotus picture on paper with a pen using Cs₃Cu₂I₅ precursor solution as the ink. This lotus picture is achromatous under sunshine, but turns blue fluorescence under UV lamp irradiation (310 nm). This illustrates that a simple solvent evaporation process can be used for Cs₃Cu₂I₅ based anti-counterfeiting and encryption applications. Moreover, they found that the blue emission color and intensity of the patterns barely changed using the ink that stored in air for 35 days, indicating that the fluorescent inks and written patterns possess a high stability. Following this work, Gao et al. used Cs₃Cu₂I₅ NCs solution as security and smart fluorescent inks for anti-counterfeiting applications.^[137] In their case, the Cs₃Cu₂I₅ NCs solution was printed as inks onto nonluminous paper to encrypt information by inkjet printing, which was invisible in sunlight. By illuminating with UV lamp, the patterns of blue “dolphin” was revealed. Thus, the UV light could be employed as the switch to control the decryption processes of the secretive information.

The anti-counterfeiting techniques based only on the optical characteristics of Cs₃Cu₂I₅ are not sufficiently effective in protecting information and are easy to clone. Based on the recognition of the

This article is protected by copyright. All rights reserved.

rotative phase transition between CsCu_2I_3 and $\text{Cs}_3\text{Cu}_2\text{I}_5$, our group developed a multiple encryption anti-counterfeiting technique based on hydrochromic $\text{Cs}_3\text{Cu}_2\text{I}_5$ NCs, which could crisply distinguish and verify information after humidity decryption.^[136] It was found that the soluble CsI in water results in a transformation from $\text{Cs}_3\text{Cu}_2\text{I}_5$ to CsCu_2I_3 , and CsI can also insert into CsCu_2I_3 to form the stable $\text{Cs}_3\text{Cu}_2\text{I}_5$ after water evaporation (Figure 14b). Thus, an advanced anti-counterfeiting pattern composed of hydrochromic $\text{Cs}_3\text{Cu}_2\text{I}_5$ NCs and water-resistant $\text{Cs}_3\text{Cu}_2\text{I}_5$ @PMMA was fabricated, and the process of encryption and decryption was shown in Figure 14c. After water decryption, the yellow and blue emission patterns carrying confidential information were fleetly recognized. After water evaporation, the patterns were encrypted as useless information with full blue fluorescence (Figure 14d). Importantly, the anti-counterfeiting pattern possesses good stability in multiple encryption/decryption, which facilitates balanced anti-counterfeiting information accessibility and improved information security. Later, Feng et al. explored the CsX solution-driven reversible $\text{Cs}_3\text{Cu}_2\text{I}_5$ fluorescent discoloration for anti-counterfeiting applications.^[42] Figure 14e presents the encryption and decryption process utilizing water and the CsX solutions, respectively. When the paper carrying the pattern was soaked in water for only a few seconds, a rapid change in fluorescence from blue to yellow was observed, corresponding to the encryption stage. Subsequently, the paper was soaked in CsX solution and the logo pattern gradually reverted to their fluorescent emission, representing the decryption process. Using CsCl or CsI solution, the emission was restored to the cyan or blue, respectively, which allows the $\text{Cs}_3\text{Cu}_2\text{I}_5$ image to perform with multicolor reversible fluorochrome.

Although exciting advances have been realized, the research on luminescent TCH materials for anti-counterfeiting is still in the laboratory development stage, and the practical application remains a huge challenge. For example, the luminescence efficiency of CsCu_2I_3 is not high enough, with PLQY less than 30%, so the resulting patterns face the issues of poor visibility after decryption, which hinders the accurate decryption of confidential information. Enhancing the fluorescence brightness and PLQY of such materials is the foremost mission in practical anti-counterfeiting applications. Moreover, under unremitting external stimulation or treatment, the TCH material may be disintegrated, which would markedly influence the application of their fluorescence properties in anti-counterfeiting. Therefore, developing new strategy to improve the stability of TCHs, meanwhile, with no effect on the responsive performance is necessary.

This article is protected by copyright. All rights reserved.

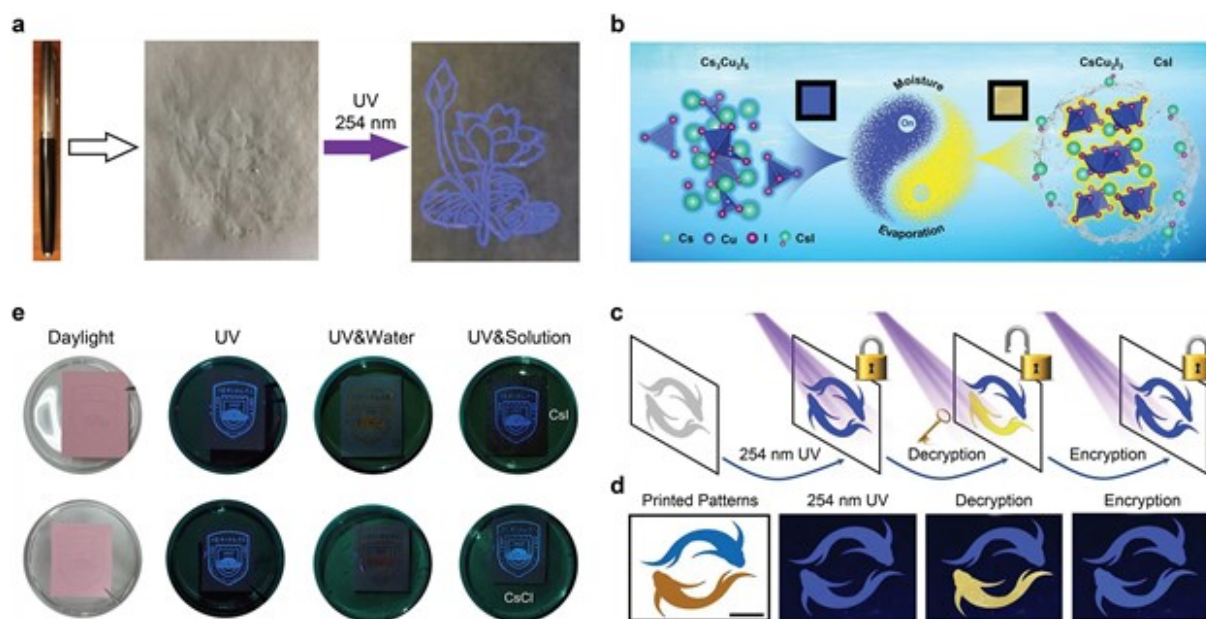


Figure 14. Anti-counterfeiting applications based on TCHs. a) Preparation process of anti-counterfeiting pattern based on the $\text{Cs}_3\text{Cu}_2\text{I}_5$ ink. (a) Reproduced with permission.^[36] Copyright 2020, Wiley-VCH. b) Schematically illustrated diagram of the reversible transition between $\text{Cs}_3\text{Cu}_2\text{I}_5$ and CsCu_2I_3 . c) Schematically illustrated diagram of encryption and decryption based on $\text{Cs}_3\text{Cu}_2\text{I}_5$ ink. d) Fluorescence images of decrypted and encrypted processes. (b–d) Reproduced with permission.^[136] Copyright 2021, Wiley-VCH. e) Fluorescence images of the logo university before and after decryption process. (e) Reproduced with permission.^[42] Copyright 2022, American Chemical Society.

7.4. X-Ray Scintillators

Since the discovery of high-energy X-ray and other radiation rays, their detection has become particularly crucial and urgent because of the widespread applications of the rays in medical science, materials imaging, and space application scenes.^[174,210] Radiation scintillators own advantages over direct X-ray detector in the way they first transferred high-energy X-ray to visible light, and then transformed to electrical signal employing the continuous photomultipliers.^[67,189] The efficient scintillators usually need some pivotal parameters, such as large light yield, high absorption coefficient, fast decay speed and response, excellent spatial resolution, and a linear relationship between light intensity and photon energy of incident rays.^[30]

TCHs are highly-promising X-ray scintillation candidates, considering that their properties match the demands of X-ray scintillators well, including large Stokes shifts with negligible self-absorption,

highly-localized emission centers, and high absorption coefficient. As an example, Lian and co-workers reported the use of 0D $\text{Cs}_3\text{Cu}_2\text{I}_5$ NCs as X-ray scintillators with large light yield and splendid stability (**Figure 15a–c**).^[153] Upon X-ray excitation, the $\text{Cs}_3\text{Cu}_2\text{I}_5$ NCs exhibit bright blue RL with a perfect linearity in the high range of X-ray dose rate and a high light yield of ≈ 79279 photons MeV^{-1} , which is better than that of the commercial CsI(Tl) scintillator (≈ 54000 photons MeV^{-1}) and LYSO:Ce scintillator (≈ 33200 photons MeV^{-1}). X-ray imaging measurements illustrated that $\text{Cs}_3\text{Cu}_2\text{I}_5$ NCs-based scintillators can offer a visualization tool for X-ray imaging with a high spatial resolution of 0.32 mm. Analogously, Niu and co-workers extended the application of Rb_2CuBr_3 to X-ray scintillators with a large RL light yield of 91056 photons MeV^{-1} .^[90] The superior performance comes from the ultrahigh PLQY (98.6%) of Rb_2CuBr_3 and the negligible self-absorption. Moreover, a low detection limit of Rb_2CuBr_3 (121.5 nGy s^{-1}) was detected, which is far lower than the required values for routine medical diagnosis (5.5 $\mu\text{Gy s}^{-1}$), laying a good foundation for low-dose medical radiography. Later, the same group reported another TCH, K_2CuBr_3 , as X-ray scintillators with ultra-low intrinsic radioactivity compared to Rb_2CuBr_3 , which exhibited an appreciable light yield of 23806 photons MeV^{-1} and a low detection limit of 132.8 nGy s^{-1} .^[114] Therefore, such 213-type TCHs not only have sensational scintillation performances for low dose X-ray imaging, but also avoid the serious issue induced by high toxicity of Pb or Tl ion.

According to reports, doping strategies can greatly improve the scintillation performance of TCHs. On the one hand, doping can repair lattice defects, thus inhibiting non-radiative recombination loss and increasing scintillation light yield.^[210] On the other hand, depending on the energy transfer processes, the energy level of transition-metal or rare-earth doping ion could serve as the extra luminescence center, which usually exhibits a relatively longer emission wavelength than the corresponding host, resulting in a significant increase in the transmittance of scintillator accompanied by less light scattering, which is important to reach high-definition X-ray imaging.^[189] In a recent report, Tl^+ was successfully doped into the host lattice of $\text{Cs}_3\text{Cu}_2\text{I}_5$ for the growth of crystal ingots, and an ultra-bright and efficient scintillator was developed for X-ray detection.^[176] Under X-ray radiation, the $\text{Cs}_3\text{Cu}_2\text{I}_5:\text{Tl}^+$ scintillators exhibit an improved PLQY of 79.2%, and their RL spectra include a STE emission located at 440 nm as well as a Tl^+ -centre emission located at 510 nm at RT. With Tl^+ doping, a superhigh light yield of 150000 photons MeV^{-1} was achieved, which is about five times that of the undoped sample. Moreover, the X-ray detection limitation could be decreased from 103.6 nGy s^{-1} for undoped products to 66.3 nGy s^{-1} for Tl^+ doped products. However, the toxicity of

Tl dopants contradicts the concept of environmental protection and safety. In other work, Wu et al. prepared an In⁺-doped Cs₃Cu₂I₅ scintillator with superior X-ray scintillation performance and proved their eminent X-ray imaging ability.^[210] It was found that the RL spectra of Cs₃Cu₂I₅:In⁺ consist of a STE emission at 460 nm and an In⁺ luminescence center at 620 nm, and the PLQY of Cs₃Cu₂I₅:In⁺ increases to 88.4% compared to the undoped counterpart (68.1%). Profiting from the large PLQY, the Cs₃Cu₂I₅:In⁺ scintillator reached a superior scintillation light yield of 53000 photons MeV⁻¹ with the low detection limitation of 96.2 nGy s⁻¹, which is better than the undoped scintillator, and the X-ray imaging resolution is up to 18 lp mm⁻¹. The enhancement could be related to the reduction of non-radiative recombination ratio because of extra efficient radiative recombination at In center.

For X-ray imaging, flexible X-ray scintillators could reach higher imaging quality on non-planar objects than rigid scintillators, because they could be molded into the desirable shapes to easily render objects.^[155] Moreover, the flexible scintillator is compatible with non-uniform X-ray under complicated scenes, which could eliminate the halo induced by uneven spatial distribution of X-ray dose on the object, thus ensuring efficient and precise illness screenings.^[201] Mohammed and co-workers fabricated a flexible, large-area X-ray scintillation screen with an area of 400 cm² based on the Cs₃Cu₂I₅-polydimethylsiloxane (Cs₃Cu₂I₅-PDMS) films.^[230] The Cs₃Cu₂I₅-PDMS films with a thickness of 300 μm exhibit no physical damages and mechanical deformations due to the rubbery nature of PDMS, as shown in Figure 15d. The performances of the resulting scintillators are remarkable in terms of a decent linear response to X-ray dose rate, a good light yield of ≈48800 photons MeV⁻¹, and a low detection limitation of 48.6 nGy s⁻¹. Profiting from the superior X-ray scintillation performance, the flexible Cs₃Cu₂I₅-PDMS films were further employed for X-ray imaging. As shown in Figure 15e,f, the interior collocation of the honeycomb structure cannot be observed with our eyes, but can be presented clearly by X-ray imaging, indicating a high-resolution imaging capacity with an excellent spatial resolution of 17 lp mm⁻¹. Soon afterwards, Liu and co-workers fabricated flexible Cs₃Cu₂I₅-PDMS films with the area of 400 cm², which present good mechanical tolerance, near-unity PLQY, excellent unity, and heat and water resistance.^[155] They demonstrated that the flexible scintillator screens can deliver a large scintillation yield of 123736 photons MeV⁻¹ and an eminent spatial resolution of 6.8 lp mm⁻¹ in X-ray imaging, and an excellent stability under steady X-ray illumination. Such flexible scintillator screens with good scintillation performance indicates its potential application in portable and wearable devices.

This article is protected by copyright. All rights reserved.

As X-ray imaging usually requires thick films of micrometer or even millimeter scales, one recent mainstream trend has been chasing thicker films, while ignoring nanoscale internal structure design. Aiming at obtaining high-quality scintillator thick films, Zhang et al. employed the close-space sublimation strategy to prepare CsCu₂I₃ thick films with oriented structures for the X-ray imaging applications.^[101] With this strategy, large-area CsCu₂I₃ thick films with the standing nanorod array were successfully fabricated. Such array offers an oriented optical channel, which whittles the internal light losses and enhances the efficiency of transferring photon to complementary metal oxide semiconductor (CMOS) panels (Figure 15g). This integrated CsCu₂I₃ detector exhibits an outstanding stability under continuous high-dose irradiation and reaches an ultrahigh spatial resolution of 7.5 lp mm⁻¹ (Figure 15h). These results certify a hopeful prospect of CsCu₂I₃ thick films with oriented structure in high-performance and low-cost disease screening.

Generally, the STE processes may bring grievous afterglow behavior with slow carrier recombination rate and long scintillation lifetime of microseconds or longer, which is detrimental to high-speed computer tomography scanning imaging. Liu and co-workers demonstrated a novel hybrid X-ray detector that combines the indirect-type Cs₃Cu₂I₅ scintillator with the direct-type MAPbI₃ semiconductor through low-cost rapid tableting processes.^[41] The response velocity of the resulting devices to X-ray is immensely reduced by ≈30 times, realizing 36.6 ns, which is attributed to the fast energy transfer from Cs₃Cu₂I₅ and MAPbI₃, enabling fast X-ray detection capability. Besides, Cs₃Cu₂I₅ occurs at the grain boundaries of MAPbI₃, restraining the route of ion migration, making the detection limitation of the hybrid detector 1.5 times lower than that of direct MAPbI₃ and 10 times smaller than that of indirect Cs₃Cu₂I₅ scintillator (Figure 15i,j). In addition, the direct/indirect hybrid detectors without any encapsulation also show improved operation stability in the ambient conditions. The above observations confirm that such hybrid X-ray detector combines the advantages of an indirect scintillator and a direct semiconductor, and could serve as a splendid complementary for the extant X-ray detector.

As a whole, TCH materials as X-ray scintillators for detection and imaging have demonstrated remarkable merits and achievements (Figure 15k and **Table 4**). Future work will focus more on improving the performance of scintillators by shrinking the scintillation lifetime to reach faster response and reducing the bandgap to obtain higher light yield. Moreover, more efforts should be devoted for other high-energy detections, such as neutron and γ -ray scintillators.

This article is protected by copyright. All rights reserved.

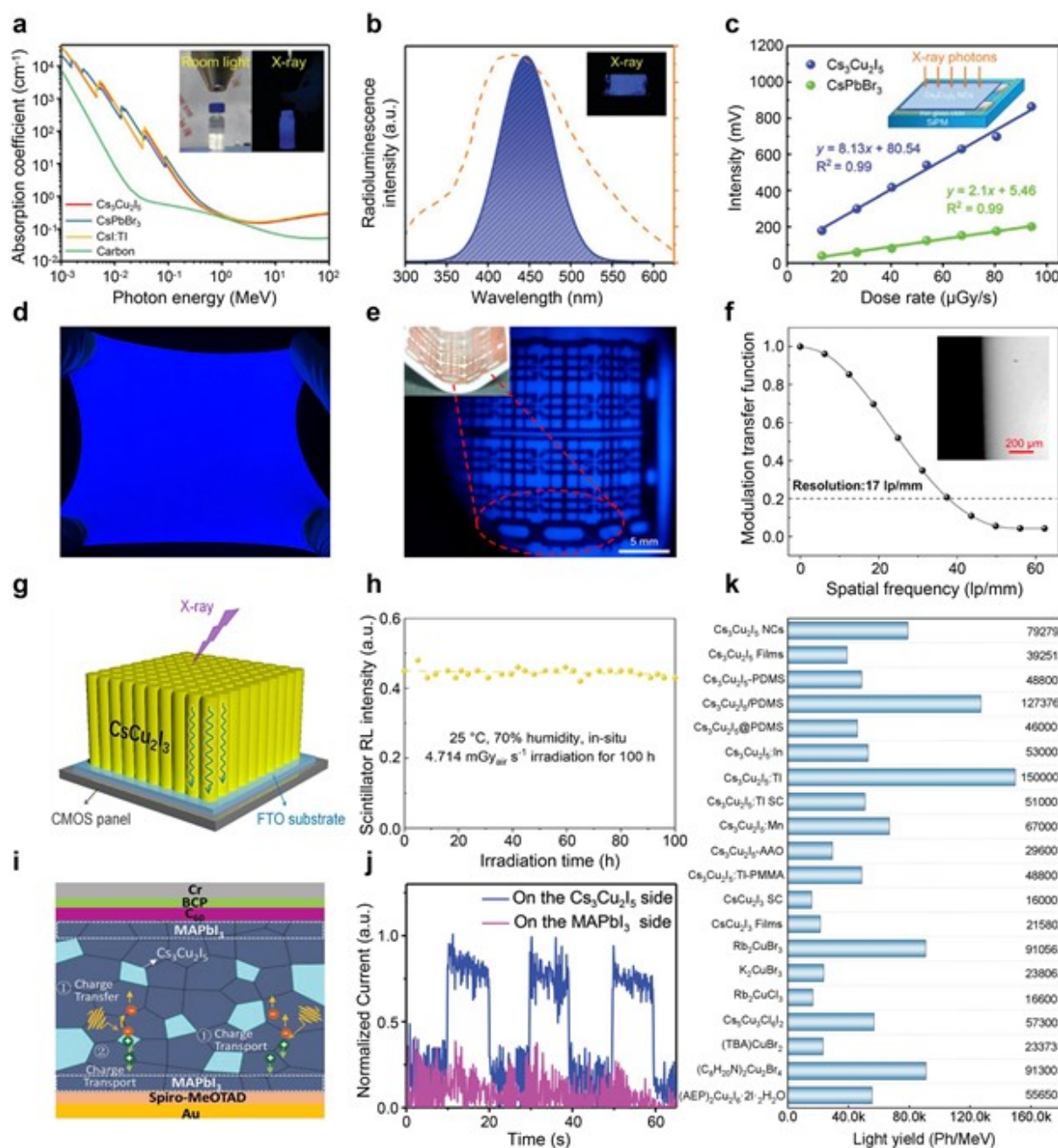


Figure 15. X-ray scintillators based on the TCHs. a) X-ray absorption coefficients of $\text{Cs}_3\text{Cu}_2\text{I}_5$, CsPbBr_3 , CsI:Tl and carbon dots versus photon energy. b) RL spectra of $\text{Cs}_3\text{Cu}_2\text{I}_5$ NC films under X-ray excitation (50 keV) and the curve of photon detection efficiency of SiPM. c) Response intensity of $\text{Cs}_3\text{Cu}_2\text{I}_5$ NC and CsPbBr_3 NC films versus X-ray dose rate. (a–c) Reproduced with permission.^[153] Copyright 2020, Wiley-VCH. d) Photographs of the $\text{Cs}_3\text{Cu}_2\text{I}_5$ -PDMS flexible films. e) X-ray image of

This article is protected by copyright. All rights reserved.

flexible copper grids taken by 50 μm $\text{Cs}_3\text{Cu}_2\text{I}_5$ -PDMS films under bending states. f) Regulation transfer function of the flexible films. (d–f) Reproduced with permission.^[230] Copyright 2022, American Chemical Society. g) Schematic of CsCu_2I_3 scintillator detector. h) Stability test of the CsCu_2I_3 scintillator under high-dose irradiation. (g,h) Reproduced with permission.^[101] Copyright 2021, American Chemical Society. i) Schematic diagram illustrating two types of charge transport paths based on the hybrid devices. j) Photocurrent on/off signals of light illuminated from sides of CsCu_2I_3 and MAPbI_3 . (i,j) Reproduced with permission.^[41] Copyright 2022, Wiley-VCH. k) Summary of the light yields of some typical TCH scintillators.

Table 4. Summary of the X-ray scintillation performances based on TCH scintillators.

Scintillators	Attributes	Light yield (photons MeV^{-1})	Detection limit (nGy s^{-1})	Spatial resolution (lp mm^{-1})	Radiation stability (min)	Ref.
$\text{Cs}_3\text{Cu}_2\text{I}_5$	Rigid	79279	–	–	–	[153]
$\text{Cs}_3\text{Cu}_2\text{I}_5$	Rigid	39251	815	100	90 (0.2 mGy s^{-1})	[226]
$\text{Cs}_3\text{Cu}_2\text{I}_5$ -PDMS	Flexible	48800	48.6	17	–	[230]
$\text{Cs}_3\text{Cu}_2\text{I}_5$ -PDMS	Flexible	127376	–	6.8	60 ($183.8 \mu\text{Gy s}^{-1}$)	[155]
$\text{Cs}_3\text{Cu}_2\text{I}_5$ -PDMS	Flexible	46000	96.54	8.6	–	[220]
$\text{Cs}_3\text{Cu}_2\text{I}_5:\text{In}^+$	Rigid	53000	96.2	18	–	[210]
$\text{Cs}_3\text{Cu}_2\text{I}_5:\text{Mn}$	Rigid	67000	–	–	–	[97]
$\text{Cs}_3\text{Cu}_2\text{I}_5:\text{TI}$	Rigid	150000	–	–	–	[176]
$\text{Cs}_3\text{Cu}_2\text{I}_5:\text{TI}$	Rigid	51000	–	–	–	[189]
$\text{Cs}_3\text{Cu}_2\text{I}_5:\text{TI}$ -PMMA	Flexible	48800	305	16.3	720 (2 mGy s^{-1})	[143]
$\text{Cs}_3\text{Cu}_2\text{I}_5$ -AAO	Rigid	31700	10	10.4	–	[175]
$\text{Cs}_3\text{Cu}_2\text{Cl}_5$	Rigid	59900	–	4	–	[174]
$\text{Cs}_3\text{Cu}_2\text{Cl}_5$	Rigid	34000	81.7	9.6	80 (174.6 Gy s^{-1})	[218]
CsCu_2I_3	Rigid	16000	–	–	–	[190]
CsCu_2I_3	Rigid	21580	–	7.5	6000 (4.7 mGy s^{-1})	[101]
Rb_2CuBr_3	Rigid	91056	121.5	–	–	[90]
Rb_2CuCl_3	Rigid	16600	88.5	–	–	[121]

This article is protected by copyright. All rights reserved.

K_2CuBr_3	Rigid	23806	132.8	–	–	[114]
$\text{Cs}_5\text{Cu}_3\text{Cl}_6\text{I}_2$	Rigid	57000	71.9	9.0	–	[58]
(TBA)CuBr ₂ -PVDF	Flexible	24134	–	–	–	[73]
$(\text{C}_8\text{H}_{20}\text{N})_2\text{Cu}_2\text{Br}_4$	Rigid	91300	52.1	9.54	–	[67]

7.5. Photodetectors

Photodetectors are fundamental optoelectronics components that absorb photons and convert them instantly into electrical impulses.^[44,45,89] Photodetectors play an important role in optical communications, remote sensing, chemical and biological detection, missile warning, and imaging, etc. Because of the advantages of large absorption coefficients, long carrier recombination lifetime, and easy solution fabrication, TCH materials are attracting increasing interest for photodetectors,^[161,215] and many breakthroughs in this field have been witnessed. Currently, TCH-based photodetectors with various operating modes have been successfully fabricated, such as photodiodes, photoconductors, and phototransistors. The photodetection performances (on/off photocurrent ratio, photoresponsivity, specific detectivity, and response speed) have already reached the competitive level with those based on traditional optical sensing materials and commercial silicon.

In 2019, Luo and co-workers demonstrated a sensitive UV photodetector composed of $\text{Cs}_3\text{Cu}_2\text{I}_5$ films.^[215] They found that the as-fabricated device exhibits nearly no sensitivity to visible light but shows noteworthy sensitivity to 365 nm and 265 nm UV light, which is attributed to the inherent wide bandgap (3.8 eV) of the $\text{Cs}_3\text{Cu}_2\text{I}_5$ active layer. Optoelectronic analysis reveals a decent responsivity of 64.9 mA W^{-1} with a specific detectivity of 6.9×10^{11} Jones, and a response speed of 26.2/49.9 ms for rise/fall time. Moreover, the studied photodetector could function as a resultful image sensor that could expediently record UV image with goodish resolution. Lately, our team successfully fabricated a spectrum-selective UV photodetector made up of $\text{Cs}_3\text{Cu}_2\text{I}_5/\text{GaN}$ heterojunction by employing the charge collection narrowing notion (**Figure 16a**).^[180] By adjusting the bias voltages and absorber thickness, a narrow spectral response “window” of 300–370 nm was observed, in which the response range presents a decreasing tendency with the increase of thickness (Figure 16b). Except the data of the basic device parameters like on/off photocurrent ratio (1.2×10^5), responsivity (0.28 A W^{-1}), specific detectivity (1.2×10^{12} Jones), and response speeds (95/130 μs , 800 Hz), the proposed photodetector exhibits a remarkable environmental and heat tolerance. Even at a high temperature of 373 K for operating 300 h, the device still maintains a good responsivity with a very small decay of

This article is protected by copyright. All rights reserved.

10%. Moreover, with an optically assisted displacement platform, a UV imaging was realized by using the such photodetectors as the sensing pixels (Figure 16c). Unlike the 0D structure of $\text{Cs}_3\text{Cu}_2\text{I}_5$, the chain-like 1D CsCu_2I_3 shows an emblematic 1D electronic dimensionality, which can be employed as the absorber for polarization-sensitive optical detection, leading to a linear polarization sensitivity. Lately, the same group reported polarization-sensitive and flexible UV photodetectors by combining the external morphology anisotropy and inherent anisotropy of the asymmetric structure of CsCu_2I_3 NWs,^[182] as illustrated in Figure 16d, and a record photocurrent anisotropy ratio of 3.16 was achieved (Figure 16f), which is the recorded value of perovskite-based polarization photodetectors. Due to the flexible and transmutable structure frame of CsCu_2I_3 NWs, the device also exhibits conspicuous bending durability and operation stability (Figure 16e), which can withstand wide angle bending (0° – 160°) and repeated bending cycles (≈ 1000 times).

Understanding the potential relationship between photoelectric performance and electronic structure is essential for achieving efficient photodetectors. We studied the crystal-facet-dependent photoresponse based on the 1D CsCu_2I_3 SCs.^[89] The (010) and (110) crystal planes of the CsCu_2I_3 SCs were deposited with Ag electrodes to investigate the photoresponse capability, as seen in Figure 16g. The results reveal that (010) plane presents a lower dark current and a higher on–off ratio compared to the (110) planes, indicating their priority in the photodetector response (Figure 16h,i). Homoplastically, the photodetector with coplaner and sandwich structures, corresponding to (100) and (001) directions, shows disparate electric conductivity. This is because of the fact that the anisotropic carrier mobility is related to high electron density and strong confinement of the (110) crystal plane. Accordingly, the on/off ratio is anisotropic with 1.6 and 24 for (001) and (100) direction, respectively, and the response time shows a decreasing characteristic. Wang et al. also investigated the photodetector performance of randomly oriented (110) planes and preferentially oriented (221) planes of CsCu_2I_3 films caused by antisolvent polarity.^[161] In the former case, the edge-sharing 1D $[\text{Cu}_2\text{I}_3]^-$ chains are completely parallel to the substrates, while in the latter case, the $[\text{Cu}_2\text{I}_3]^-$ chains intersect with the substrates at an angle of 30° , which enhances the charge transport. Therefore, the response speed of the photodetector was decreased from 2.7 ms to 860 μs . Similarly, Mo and co-workers used the 1D CsCu_2I_3 SCs to fabricate UV photodetectors with a planar metal-semiconductor-metal structure of $\text{Ni}/\text{CsCu}_2\text{I}_3/\text{Ni}$, which exhibits a fast response rise time of 50.4 ms and a fall time of 244.8 ms under 340 nm illumination.^[126]

This article is protected by copyright. All rights reserved.

Besides, CsCu₂I₃ material with p-type conductivity has also been employed as a charge carrier extraction layer to enhance the device performance. For instance, a vertical p- CsCu₂I₃/n-Ca₂Nb_{3-x}Ta_xO₁₀ heterojunction photodetector is fabricated recently,^[45] in which the CsCu₂I₃ films with a large bandgap of 3.51 eV serve as the hole transport layers (Figure 16j). The heterojunction photodetector shows an outstanding UV light detection performance with a high rectification ratio of 16136, as shown in Figure 16k. Meanwhile, a high EQE of 40400% and a large responsivity of 81.3 A W⁻¹ under 250 nm illumination were achieved, respectively. The resulting photodetector can also be integrated on a flexible poly-ethylene terephthalate (PET) substrate to prepare large-scale flexible photodetector, which can withstand 5000 times of bending while maintaining 80% of the original photocurrent. Moreover, an 8 × 8 array stimulated with UV light is fabricated to present their potential for imaging sensor, as shown in Figure 16l. These results verify that the CsCu₂I₃ is hopeful materials for high-efficiency photodetectors.

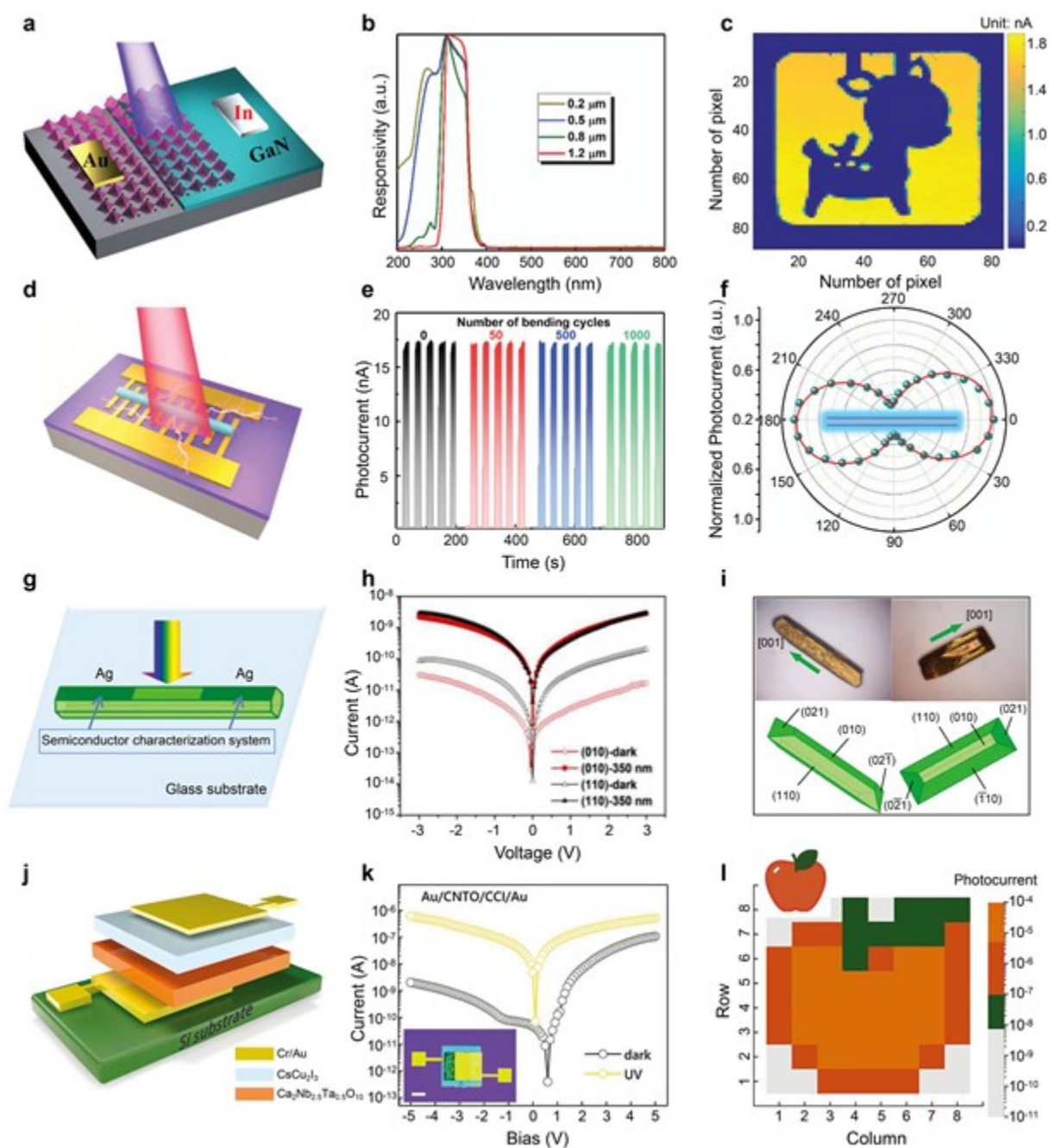


Figure 16. Photodetectors based on the TCHs. a) Schematic diagram of the $\text{Cs}_3\text{Cu}_2\text{I}_5/\text{GaN}$ heterojunction photodetectors. b) Response spectra of the photodetector with different thicknesses of $\text{Cs}_3\text{Cu}_2\text{I}_5$ absorber. c) High-resolution imaging results of a “deer” pattern. (a–c) Reproduced with permission.^[180] Copyright 2020, Royal Society of Chemistry. d) Illustration of photodetectors made of one CsCu_2I_3 nanowire. e) $I-t$ curves of the flexible photodetectors at various bending cycles. f)

This article is protected by copyright. All rights reserved.

Polarization dependence of the photocurrent for CsCu₂I₃-based photodetector. (d–f) Reproduced with permission.^[182] Copyright 2020, Royal Society of Chemistry. g) Schematic diagram of the CsCu₂I₃ SC-based photodetector. h) I – V curves of devices from (110) and (010) crystal planes of CsCu₂I₃. i) Optical microscopy images of CsCu₂I₃ SC with rod-shaped morphology. (g–i) Reproduced with permission.^[89] Copyright 2020, Wiley-VCH. j) Schematic diagram of Au/p-CsCu₂I₃/n-Ca₂Nb_{3-x}Ta_xO₁₀/Au structured photodetector. k) I – V curves of the photodetectors under dark and UV light excitation. l) Photocurrent mapping of UV imaging arrays. (j–l) Reproduced with permission.^[45] Copyright 2022, Wiley-VCH.

Although these developments are encouraging, the performance of TCH-based photodetector is still far from meeting the requirements of practical applications,^[26] and there are still many remaining challenges and potential breakthroughs. For instance, the notorious defects in surface or interior of materials and the low carrier mobility of TCHs restrict the efficient transport of photogenerated charge carriers seriously.^[28] To resolve these issues, detailed investigations on the charge carrier kinetics are required to offer well-thought-out conceptions for understanding the mechanisms of defects in the materials. On this basis, more theoretical and experimental studies are needed to improve the overall performance of TCH-based photodetectors.

7.6. Sensors

The changes of optical and electrical properties of TCH materials under stimulations, for instance, various gases, volatile organic solvents, heat, and moisture, make them a potential candidate for different types of sensors.^[86,120,202] Among the TCH materials, K₂CuBr₃ is deemed as a hopeful moisture sensitive material because of its sensitive surface peculiarities and solution processability. Chang et al. fabricated hypersensitized humidity sensors based on K₂CuBr₃ MWs and demonstrated its application in human respiratory monitoring (**Figure 17a**).^[202] The humidity test results show that the proposed humidity sensor realized a logarithmic linearity in the humidity ranges from 11% to 95% RH, and presented fast response/recovery response (10.63 s/4.31 s) and a good repeatability (Figure 17b). Moreover, the sensor was employed for real-world human respiratory monitoring, capturing the status of nasal respiration, oral respiration, normal respiration, and apnea (Figure 17c). The humidity sensing mechanism based on K₂CuBr₃ MWs can be described as: when the sensor is in low RH condition, the water molecule is adsorbed on the K₂CuBr₃ MW through the chemical adsorption process and release free protons (H⁺). With the increase of humidity, the adsorbed water molecule forms continuous water layers, and hydrated protons (H₃O⁺) are formed through the reaction of H₂O +

This article is protected by copyright. All rights reserved.

$H^+ \rightarrow H_3O^+$. When the sensor is exposed to high RH, the water molecule is adsorbed on the K_2CuBr_3 through physical adsorption process. Such reaction of multiple absorption processes results in a high humidity response of the sensor. In 2021, Huang and co-workers studied the effects of surface ligand on the impedance change-based humidity sensing performances of $Cs_3Cu_2Br_5$ by using electrochemical impedance spectroscopy.^[120] The proposed sensors exhibit low hysteresis, good repeatability, and decent stability under different humidity conditions (12–95%). They found that short-chain ligand is more conducive to reaching porous films with stronger water adsorption, resulting in a boosted humidity sensing performances.

TCH semiconductor materials could also serve as potential candidates for gas sensors, due to their prominent semiconducting properties. Lee et al. developed a novel type of gasochromic gas sensor utilizing the reversible phase transition between $CsCu_2I_3$ and $Cs_3Cu_2I_5$ with disparate characteristics.^[86] The phase transformation was attributed to the destruction/formation of Cu–Cu and Cs–I bonds during the hydroxyl attachment/desorption, enabling them to be used as sensors for detecting water and hydroxyl. The most polar water has the strongest attraction to Cu^+ and I^- ions, thus promoting the occurrence of phase transition. When hydroxyl gas was detected, the multi-mode sensors redshift the emission spectra from 445 to 575 nm, while the humidity sensor confirms that the response time is less than 5 s for breathing and less than 30 s for air recovery (Figure 17d). It is worth noting that except for the hydroxyl gas, the optical response of the device is basically unchanged under various gas conditions, such as H_2 , O_2 , CO_2 , and NO (Figure 17e), indicating that the gasochromic sensor has a substantial selectivity towards the hydroxyl groups. Also, the sensor remained $\approx 90\%$ of its original responsivity over one year, showing a remarkable stability.

Since the sensors study on TCHs is still in its infancy, there are some contradictions in the derived sensing mechanisms. TCHs sharing a similar composition may conduct quite different reaction processes owing to the different surface state or dimensional size.^[26] Therefore, a deeper understanding of TCHs involved reaction mechanisms is essential and there is much room for development.

7.7. Memristors

In addition to the aforementioned optoelectronic applications, TCH materials are also used for the resistive memory devices, i.e., memristors.^[115,167,222,225] The memristors made up of $Cs_3Cu_2I_5$ active layer with the typical sandwich-like structure of $Ag/Cs_3Cu_2I_5/Au$ were demonstrated by Zeng et al.^[115]

To enhance the stability of the devices, they introduced PMMA as an isolation layer between top Ag electrode and $\text{Cs}_3\text{Cu}_2\text{I}_5$ films. The resulting memristors produce bipolar resistive switching performance with a high on/off ratio (10^2), a low operating voltage ($< \pm 1$ V), a stable patience (100 cycles), and a long-term retention ($> 10^4$ s). Most importantly, this work has been checked for their long-term depression and long-term potentiation properties, resulting in a biological synaptic activity recognition rate of 94%. Following this work, Park et al. reported a flexible and transparent memristor based on an ITO/PEDOT:PSS/ $\text{Cs}_3\text{Cu}_2\text{I}_5$ /Au structure for artificial synapses (Figure 17f).^[196] Resistance as high as 243 M Ω was reached upon a writing pulse, resulting in an energy consumption of 10.48×10^{-18} J μm^{-2} , which in turn meets the minimum resistance required for 10^6 arrays parallel operation. They verified an interfacial resistive switch of the Schottky junction between Au and p-type $\text{Cu}_3\text{Cs}_2\text{I}_5$. The asymmetric carrier transport and migration of iodide vacancies play a key role in controlling conductance, because the effective hole mass is three times the effective electron mass, which results in a high resistance (Figure 17g). Bending tolerance tests indicate that the recognition rate of the studied device remains above 90% of the initial value upon bending, indicating a hopeful and potential candidate for stable and high-performance flexible artificial synapses.

In whole, the TCHs-based memristors possess significant virtues of high on/off ratio, low operating voltage, and low power dissipation, and excel in optoelectronic control system. Moreover, the multifunctional resistive switching features have facilitated its further applications in high-density information storage. In addition, due to the low temperature fabrication technique of TCH materials, flexible memristors with stable characters under various bending states have been explored. However, the endurance of an overwhelming majority of TCHs-based memristors is less than 10^3 cycles, far lower than that of conventional metal oxide memristors.^[225] A thorough understanding of the resistance switching mechanism and the reason for cycling failure is the key to improving the reliability. Moreover, considering the environmental sensitivity and state retention of TCHs-based memristors, it is recommended to reasonably evaluate the retention cycles at high humidity, high temperature, and high oxygen environment.

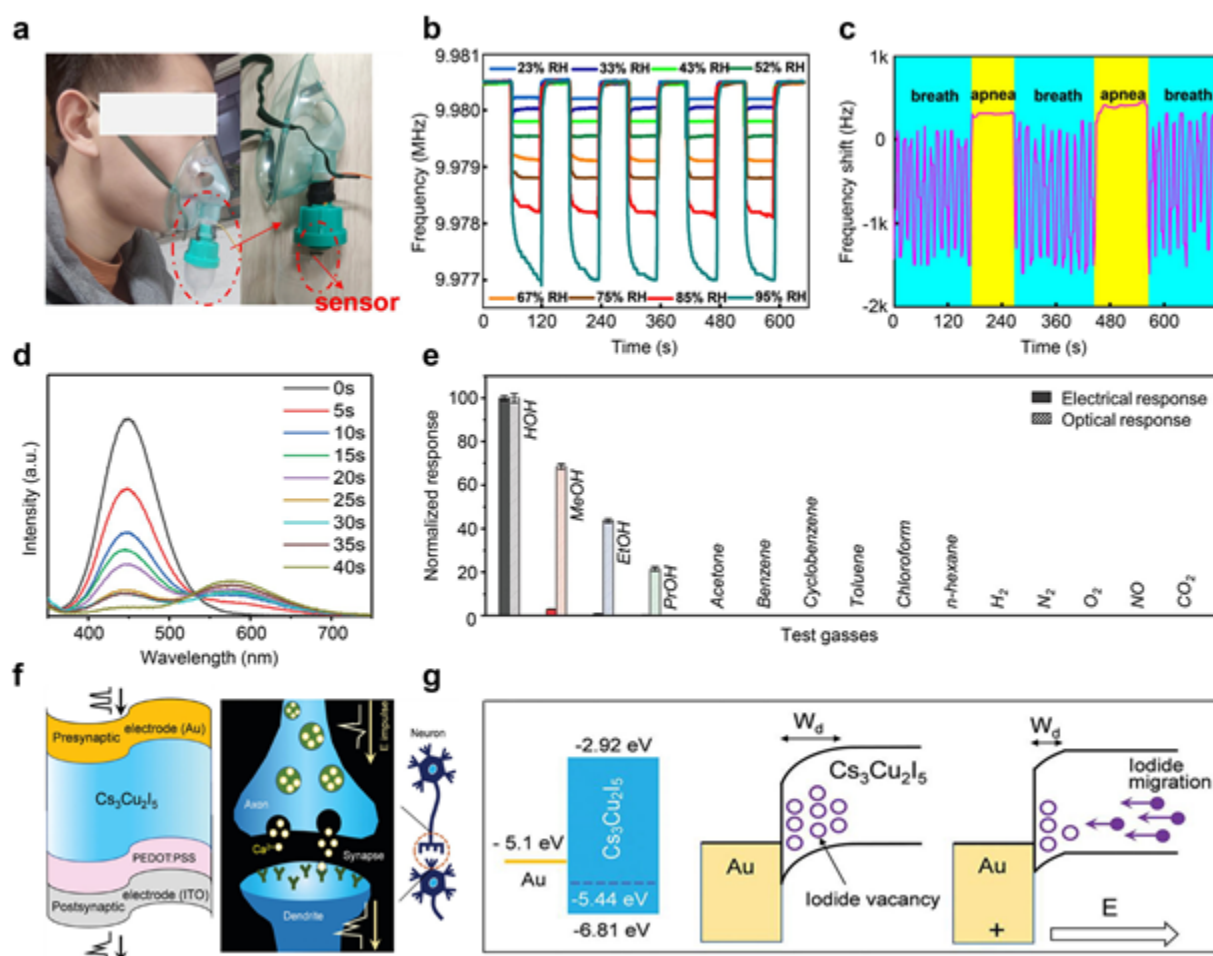


Figure 17. Sensors and memristors based on TCHs. a) Photograph of the breath measurement of K_2CuBr_3 -based humidity sensor. b) Repeatability of humidity sensors exposed to different relative humidity. c) Response of normal breathing and apnea. (a–c) Reproduced with permission.^[202] Copyright 2022, Elsevier. d) Gasochromic PL spectra of the sensor based on $Cs_3Cu_2I_5$ SCs. e) Gas selectivity of the sensor based on the $Cs_3Cu_2I_5$ films. (d,e) Reproduced with permission.^[86] Copyright 2022, Wiley-VCH. f) Schematic diagram of the $Cs_3Cu_2I_5$ -based flexible memristors for artificial synapses. g) Working mechanism of the memristor device. (f,g) Reproduced with permission.^[196] Copyright 2021, Royal Society of Chemistry.

8. Conclusions and Prospects

The rapid development and research of TCH materials could be described as a “gold rush”. Within five years after their discovery, TCHs materials have shown their great potential in versatile

applications, and their basic features have demonstrated remarkable benefits. We herein reviewed the recent research progress on TCH materials, including their structural diversity, synthesis strategy, optical properties, stability, and related optoelectronic applications. The nontoxic features as well as the novel structures lead to outstanding optoelectronic properties, such as high absorption cross-sections with UV excitation, highly efficient Stokes-shifted broadband emission, high PLQY at visible wavelengths, negligible self-absorption, as well as enhanced stability. The above excellent properties have enabled potential applications in a variety of optoelectronic devices, including phosphor-converted WLEDs, electroluminescent LEDs, anti-counterfeiting, X-ray scintillators, photodetectors, sensors, and memristors. Despite significant successes and progresses, more opportunities on both material nature understandings and optoelectronic applications are still waiting to be discovered before such materials reaching commercial feasibility. In addition to the examples given in this review, the current challenges and possible future development directions in the field of TCHs include, but are not limited to, the following:

1) Although TCH materials containing multifarious all-inorganic and organic-inorganic hybrid systems in various states have been developed, most of them can only be prepared by trial and error and the formation of crystal structures seems to be random. Therefore, it is essential to establish a reasonable relationship between synthetic control and structural characteristics to guide the synthesis of these materials. Moreover, the synthetic control of such materials has not yet reached the identical level as that of conventional organic and inorganic materials. To achieve such precise control, developing computational approaches to predict the forming processes of TCH materials may be useful. The combination of diverse compositions and various connection types between the adjacent copper-halide polyhedrons provides a good deal of basic metal halide frames for the constitution of TCHs with adjustable electronic structure, but the rules between them are still quite vague. Thus, more studies are required to describe the relationship between the functional copper-halide polyhedrons and the resulting crystal structures, as well as their electronic structure properties.

2) Although preliminary mechanism studies have demonstrated that the radiative recombination of STEs is deemed to be the primary reason of broadband PL with large Stokes shifts, more viewpoints concerning how the STE forms, what the relationships between STE-excited states, structural deformation and electron-phonon coupling is, and the specific recombination processes from STEs need to be further explored. An important challenge is that we can hardly observe the occurrences and

evolutions of the STEs directly, but can only infer from the measured optoelectronic characteristics. Thus, the further researches are necessary to determine the origin of PL and reveal the excitonic behaviors in excited states, including exciton delocalization, exciton localization and self-trapping. Combined with the femtosecond time-resolved spectroscopy, 4D ultrafast electron microscopy, theoretical calculation and other advanced technologies, the mystery for the photophysical process is expected to be clarified, which also helps to precisely judge and regulate the properties of materials, and is of great significance to develop similar materials with target properties.

3) Although colorful TCHs have been explored, there is still a considerable gap in the coverage and control range of emission spectrum compared with lead-halide perovskites. Based on the current reports, the emission spectrum of most TCHs only covers part of visible light, presenting broadband emission in violet, blue, green or yellow regions, that is, there are certain challenges in achieving red and near-infrared emission, which may limit their broad applications. The reason for the lack of low energy emitters is not well understood currently. To find redder materials, either materials with a smaller ground state bandgap must be found, or they must be able to withstand larger distortions to induce deeper self-trapping states. Another strategy is through introducing additional emitting centers that show ionic luminescence into the host lattice to reach red or even near-infrared emission. As a case, doping In^+ ions in the blue-emitting $\text{Cs}_3\text{Cu}_2\text{I}_5$ can achieve a red emission located at 620 nm with an admirable PLQY.^[210] Besides, the fundamental physical cognition of such TCH materials is still quite limited. For example, PL spectroscopy remains the main function that has been extensively studied so far, while other properties, such as magnetic and electronic properties, have not been fully studied. For this purpose, there is a requirement to further go after multidisciplinary study beyond the current state-of-the-art to promote their further development.

4) The stability of TCH materials needs to be further enhanced because they fall far short of commercial requirements. This is partly because the ionic properties similar to the perovskites with soft lattices and low formation energy, making them easy to disintegrate under environmental and harsh conditions. Heat, oxygen, and moisture are main factors that degrade the TCH materials. Many materials presented herein are oxygen- and moisture-sensitive to varying degrees, lasting anywhere from a few minutes to a few months in atmospheric environment, resulting in the degradation of their PLQY or decay into other products. Some of these adverse impacts could be alleviated by coating inert fillers with inorganic or hydrophobic organic layers, or simply by operating in blunt or vacuum

atmosphere. In terms of thermal degradation, strategies that could enhance their thermal tolerance without negatively influencing their optoelectronic performances are raring. Our current understandings show that the development of materials with rigid structures and effective doping or alloying strategies are expected to improve their thermal stability.

5) The bulk/surface defects of TCH materials have impeded their applications in optoelectronic devices. For optical properties, the defects can be regarded as non-radiative recombination centers, resulting in the reduction of the PLQY and emission attenuation. For electrical properties, the charge carriers are trapped and quenched by the defects, leading to a reduced carrier mobility and shortened carrier lifetime. Studying the role of defects through theoretical calculations, especially intrinsic point defects, is the primary task. To effectively passivate the defects experimentally, many tactics of optimization on the growth conditions and structures have been developed to enhance the crystal quality, such as additive engineering, surface passivation, post treatment, and composition engineering. To be honest, the current progresses in defect engineering of TCH materials are still preliminary, and more efforts are needed to uncover the passivation mechanisms, which is expected to set off a wave of research in the future.

6) The low electronic dimensionality of TCH materials is the main culprit for their large electron/hole effective masses, low charge carrier mobilities, short carrier lifetime, and high charge trapping density. This cloud has plagued the system for a long time, and only a handful of research groups have explored their inner roots. Learned from the well-established experience of lead-halide perovskites, doping or alloying may be a promising pathway for modulating the electronic dimensionality of TCHs. The energy band of TCHs with low electronic dimensionality is characterized by the localized VBM formed by Cu 3d orbital and halide np orbitals, which gives rise to a large effective mass of holes. Therefore, the effect of doping or alloying on the charge wave function, especially the hole wave function, needs to be determined in detail by theoretical calculation in advance, which is conducive to ensuring the effectiveness of the strategy. Of course, the amounts of dopant should be prudently controlled in the experimental operation and the doping as well as materials growth need to be proceeded as slowly as possible to guarantee the success doping or alloying.

7) Performances of TCHs-based optoelectronic devices need to be further enhanced. For phosphor-converted WLEDs, the mismatch between the optimal excitation wavelengths of the emitters and the

excitation wavelength of commercial blue or UV chips results in inferior luminous efficiency, despite the extreme high PLQY of the emitters. To this end, one possible tactic is to explore other element doping or alloying to regulate the electronic structure (or state) to adjust the excitation spectra of the emitters. The performance of electroluminescent LEDs is restricted by two main aspects, e.g., poor active emitter quality and inefficient charge carrier transport/injection. Coordinated theoretical calculations are needed to uncover the crystallization mechanisms and carrier kinetics, so as to combine with experiment efforts to enhance the films quality with few defects. For instance, CsCu₂I₃ films are usually susceptible to uncontrolled and fast crystallization that can lead to inferior crystal quality.^[95] This could be countered by methods like introducing suitable organic additives for the intermediate phase formation to promote controlled and homogeneous nucleation. To improve the charge carrier injection from electrodes into the emitters, selecting applicable HTLs and ETLs or introducing additional ETL/HTL functional layer as bridges are potential solutions to minish the injection barriers and boost the EL efficiency. Apart from the carrier function layer optimization strategies, the device performance can also be enhanced by the defect passivation engineering, surface/interface engineering, and host-dopant strategy. TCH materials have demonstrated great achievements as ideal X-ray scintillators, while their scintillation lifetime should be further shortened to reach fast-response and high-sensitivity imaging applications. Certain photodetector applications are still hampered by common challenges related to high photoresponsivity, large specific detectivity, fast response speed, operation stability, etc., of the TCH absorbers. Structural morphology has been demonstrated to be an instrumental parameter for determining the device performance, which must be perfected, equal emphases have to be placed on interfacial engineering to realize high performance in the usual device architecture. Moreover, considering the exquisite structure and property adjustability of TCH materials, new functionalities and applications, such as anti-counterfeiting, sensors, and memristors, still need to be further explored.

With increasing enthusiasm on exploring TCH materials across all structural systems and studying their feasibility in not only optical and electrical properties but also in a vast array of optoelectronic applications, they can achieve many goals to emerge as the low-cost, nontoxic, sustainable, “wonder” semiconductors of the new era. We hope that this review will assist readers in comprehending the advances of research on TCH materials, solving the remaining issues, and developing high-performance novel TCHs-based devices for practical applications.

This article is protected by copyright. All rights reserved.

AUTHOR INFORMATION

Corresponding Author

*E-mail: (Z.S.) shizf@zzu.edu.cn

*E-mail: (X.F.) xshfang@fudan.edu.cn

Notes

The authors declare no competing financial interest.

ACKNOWLEDGMENTS

The work is financially supported by the National Key R&D Program of China (No. 2022YFB2803900), National Natural Science Foundation of China (Nos. 12074347, 12004346, and 61935009), Science Foundation for Distinguished Young Scholars of Henan Province (No. 212300410019), and Support Program for Scientific and Technological Innovation Teams of Higher Education in Henan Province (No. 231RTSTHN012).

Received: ((will be filled in by the editorial staff))

Revised: ((will be filled in by the editorial staff))

Published online: ((will be filled in by the editorial staff))

- [1] A. Kojima, K. Teshima, Y. Shirai, T. Miyasaka, *J. Am. Chem. Soc.* **2009**, *131*, 6050.
- [2] M. De Bastiani, A. J. Mirabelli, Y. Hou, F. Gota, E. Aydin, T. G. Allen, J. Troughton, A. S. Subbiah, F. H. Isikgor, J. Liu, L. Xu, B. Chen, E. Van Kerschaver, D. Baran, B. Fraboni, M. F. Salvador, U. W. Paetzold, E. H. Sargent, S. De Wolf, *Nat. Energy* **2021**, *6*, 167.
- [3] Z. Ni, C. Bao, Y. Liu, Q. Jiang, W. Q. Wu, S. Chen, X. Dai, B. Chen, B. Hartweg, Z. Yu, Z. Holman, J. Huang, *Science* **2020**, *367*, 1352.
- [4] D. H. Kang, N. G. Park, *Adv. Mater.* **2019**, *31*, 1805214.
- [5] Z. Li, B. Li, X. Wu, S. A. Sheppard, S. Zhang, D. Gao, N. J. Long, Z. Zhu, *Science* **2022**, *376*, 416.
- [6] N. Li, X. Niu, L. Li, H. Wang, Z. Huang, Y. Zhang, Y. Chen, X. Zhang, C. Zhu, H. Zai, Y. Bai, S. Ma, H. Liu, X. Liu, Z. Guo, G. Liu, R. Fan, H. Chen, J. Wang, Y. Lun, X. Wang, J. Hong, H. Xie, D. S. Jakob, X. G. Xu, Q. Chen, H. Zhou, *Science* **2021**, *373*, 561.
- [7] P. Liu, N. Han, W. Wang, R. Ran, W. Zhou, Z. Shao, *Adv. Mater.* **2021**, *33*, 2002582.
- [8] H. Min, D. Y. Lee, J. Kim, G. Kim, K. S. Lee, J. Kim, M. J. Paik, Y. K. Kim, K. S. Kim, M. G. Kim, T. J. Shin, S. Il Seok, *Nature* **2021**, *598*, 444.
- [9] D. Ma, K. Lin, Y. Dong, H. Choubisa, A. H. Proppe, D. Wu, Y. K. Wang, B. Chen, P. Li, J. Z. Fan, F. Yuan, A. Johnston, Y. Liu, Y. Kang, Z. H. Lu, Z. Wei, E. H. Sargent, *Nature* **2021**, *599*, 594.
- [10] Z. Shi, S. Li, Y. Li, H. Ji, X. Li, D. Wu, T. Xu, Y. Chen, Y. Tian, Y. Zhang, C. Shan, G. Du, *ACS Nano* **2018**, *12*, 1462.
- [11] Z. Shi, Y. Li, S. Li, X. Li, D. Wu, T. Xu, Y. Tian, Y. Chen, Y. Zhang, B. Zhang, *Adv. Funct. Mater.* **2018**, *28*, 1707031.
- [12] J. Chen, J. Wang, X. Xu, J. Li, J. Song, S. Lan, S. Liu, B. Cai, B. Han, J. T. Pecht, D. Ginger, H. Zeng, *Nat. Photonics* **2021**, *15*, 238.
- [13] Z. K. Tan, R. S. Moghaddam, M. L. Lai, P. Docampo, R. Higler, F. Deschler, M. Price, A. Sadhanala, L. M. Pazos, D. Credginton, F. Hanusch, T. Bein, H. J. Snaith, R. H. Friend, *Nat. Nanotechnol.* **2014**, *9*, 687.
- [14] J. Zhang, T. Zhang, Z. Ma, F. Yuan, X. Zhou, H. Wang, Z. Liu, J. Qing, H. Chen, X. Jian, S. Su, J. Xie, Z. Shi, L. Hou, C. Shan, *Adv. Mater.* **2022**, 2209002.
- [15] Z. Chu, Y. Zhao, F. Ma, C. X. Zhang, H. Deng, F. Gao, Q. Ye, J. Meng, Z. Yin, X. Zhang, J. You, *Nat. Commun.* **2020**, *11*, 4165.
- [16] Y. Cao, N. Wang, H. Tian, J. Guo, Y. Wei, H. Chen, Y. Miao, W. Zou, K. Pan, Y. He, H. Cao, Y. Ke, M. Xu, Y. Wang, M. Yang, K. Du, Z. Fu, D. Kong, D. Dai, Y. Jin, G. Li, H. Li, Q. Peng, J. Wang, W. Huang, *Nature* **2018**, *562*, 249.
- [17] J. S. Kim, J. M. Heo, G. S. Park, S. J. Woo, C. Cho, H. J. Yun, D. H. Kim, J. Park, S. C. Lee, S. H. Park, E. Yon, N. C. Greenham, T. W. Lee, *Nature* **2022**, *611*, 688.
- [18] Z. Ma, Z. Shi, D. Yang, F. Zhang, S. Li, L. Wang, D. Wu, Y. Zhang, G. Na, L. Zhang, X. Li, Y. Zhang, C. Shan, *ACS Energy Lett.* **2019**, *5*, 385.

- [19] P. Du, J. Li, L. Wang, L. Sun, X. Wang, X. Xu, L. Yang, J. Pang, W. Liang, J. Luo, Y. Ma, J. Tang, *Nat. Commun.* **2021**, *12*, 4751.
- [20] Q. A. Akkerman, G. Raino, M. V. Kovalenko, L. Manna, *Nat. Mater.* **2018**, *17*, 394.
- [21] Z.-Z. Ma, Z.-F. Shi, L.-T. Wang, F. Zhang, D. Wu, D.-W. Yang, X. Chen, Y. Zhang, C.-X. Shan, X.-J. Li, *Nanoscale* **2020**, *12*, 3637.
- [22] C. Sun, Y. Jiang, M. Cui, L. Qiao, J. Wei, Y. Huang, L. Zhang, T. He, S. Li, H.-Y. Hsu, C. Qin, R. Long, M. Yuan, *Nat. Commun.* **2021**, *12*, 2207.
- [23] Z. Guo, J. Li, R. Pan, J. Cheng, R. Chen, T. He, *Nanoscale* **2020**, *12*, 15560.
- [24] Y. Hui, S. Chen, R. Lin, W. Zheng, F. Huang, *Mater. Chem. Front.* **2021**, *5*, 7088.
- [25] X. Chen, M. Jia, W. Xu, G. Pan, J. Zhu, Y. Tian, D. Wu, X. Jian, Z. Shi, *Adv. Optical Mater.* **2023**, *11*, 2202153.
- [26] Y. Li, Z. Zhou, N. Tewari, M. Ng, P. Geng, D. Chen, P. K. Ko, M. Qammar, L. Guo, J. E. Halpert, *Mater. Chem. Front.* **2021**, *5*, 4796.
- [27] J. Yin, Q. Lei, Y. Han, O. M. Bakr, O. F. Mohammed, *Phys. Status Solidi RRL* **2021**, *15*, 2100138.
- [28] B. Zhang, X. Wu, S. Zhou, G. Liang, Q. Hu, *Front. Optoelectron.* **2021**, *14*, 459.
- [29] Z. Ma, L. Wang, X. Ji, X. Chen, Z. Shi, *J. Phys. Chem. Lett.* **2020**, *11*, 5517.
- [30] Q. Guo, X. Zhao, B. Song, J. Luo, J. Tang, *Adv. Mater.* **2022**, *34*, 2201008.
- [31] F. Zhang, Z. Ma, Z. Shi, X. Chen, D. Wu, X. Li, C. Shan, *Energy Mater. Adv.* **2021**, *2021*, 5198145.
- [32] M. D. Smith, H. I. Karunadasa, *Acc. Chem. Res.* **2018**, *51*, 619.
- [33] Y. Liu, A. Nag, L. Manna, Z. Xia, *Angew. Chem., Int. Ed.* **2021**, *60*, 11592.
- [34] J. Luo, X. Wang, S. Li, J. Liu, Y. Guo, G. Niu, L. Yao, Y. Fu, L. Gao, Q. Dong, C. Zhao, M. Leng, F. Ma, W. Liang, L. Wang, S. Jin, J. Han, L. Zhang, J. Etheridge, J. Wang, Y. Yan, E. H. Sargent, J. Tang, *Nature* **2018**, *563*, 541.
- [35] Z. Ma, Z. Shi, D. Yang, Y. Li, F. Zhang, L. Wang, X. Chen, D. Wu, Y. Tian, Y. Zhang, L. Zhang, X. Li, C. Shan, *Adv. Mater.* **2021**, *33*, 2001367.
- [36] F. Zhang, Z. Zhao, B. Chen, H. Zheng, L. Huang, Y. Liu, Y. Wang, A. L. Rogach, *Adv. Optical Mater.* **2020**, *8*, 1901723.
- [37] J.-J. Yan, J.-L. Ma, M.-Y. Zhang, R.-T. Yang, X. Chen, D. Wu, Y.-T. Tian, X.-J. Li, Z.-F. Shi, *J. Mater. Chem. C* **2021**, *9*, 12535.
- [38] T. Jun, K. Sim, S. Iimura, M. Sasase, H. Kamioka, J. Kim, H. Hosono, *Adv. Mater.* **2018**, *30*, 1804547.
- [39] P. Ran, L. Yang, T. Jiang, X. Xu, J. Hui, Y. Su, C. Kuang, X. Liu, Y. M. Yang, *Adv. Mater.* **2022**, *34*, 2205458.
- [40] F. Zhang, D. Yang, Z. Shi, C. Qin, M. Cui, Z. Ma, L. Wang, M. Wang, X. Ji, X. Chen, D. Wu, X. Li, L. Zhang, C. Shan, *Nano Today* **2021**, *38*, 101153.

This article is protected by copyright. All rights reserved.

- [41] L. Liu, W. Li, X. Feng, C. Guo, H. Zhang, H. Wei, B. Yang, *Adv. Sci.* **2022**, *9*, 2103735.
- [42] J. Feng, J. Wang, D. Wang, M. Han, G. Qian, F. Wu, Q. Lin, Z. Hu, *ACS Appl. Electron. Mater.* **2022**, *4*, 225.
- [43] R. Roccanova, A. Yangui, H. Nhalil, H. Shi, M.-H. Du, B. Saparov, *ACS Appl. Electron. Mater.* **2019**, *1*, 269.
- [44] Q. Wang, C. Wang, Z. Wang, X. Sun, M. N. Nikl, X. OuYang, Y. Wu, *J. Phys. Chem. Lett.* **2022**, *13*, 9066.
- [45] J. Chen, X. Liu, Z. Li, F. Cao, X. Lu, X. S. Fang, *Adv. Funct. Mater.* **2022**, *32*, 2201066.
- [46] Z. Sun, X. Chen, W. Yin, *J. Semicond.* **2020**, *41*, 052201.
- [47] M.-H. Du, *ACS Energy Lett.* **2020**, *5*, 464.
- [48] R. Roccanova, A. Yangui, G. Seo, T. D. Creason, Y. Wu, D. Y. Kim, M.-H. Du, B. Saparov, *ACS Mater. Lett.* **2019**, *1*, 459.
- [49] J. Yang, W. Kang, Z. Liu, M. Pi, L. B. Luo, C. Li, H. Lin, Z. Luo, J. Du, M. Zhou, X. Tang, *J. Phys. Chem. Lett.* **2020**, *11*, 6880.
- [50] W. Liu, K. W. Na, H. Lin, Z. Dai, J. Xu, S. Su, Z. Tang, S. Wang, *J. Phys. Chem. C* **2021**, *125*, 13076.
- [51] P. Sebastia-Luna, J. Navarro-Alapont, M. Sessolo, F. Palazon, H. J. Bolink, *Chem. Mater.* **2019**, *31*, 10205.
- [52] K.-X. Xu, Z. Zhou, J. Zhang, *J. Phys. Chem. Lett.* **2023**, *14*, 32.
- [53] K. Kundu, P. Dutta, P. Acharyya, K. Biswas, *J. Phys. Chem. C* **2021**, *125*, 4720.
- [54] T. D. Creason, A. Yangui, R. Roccanova, A. Strom, M. H. Du, B. Saparov, *Adv. Optical. Mater.* **2019**, *8*, 1901338.
- [55] T. D. Creason, T. M. McWhorter, Z. Bell, M. H. Du, B. Saparov, *Chem. Mater.* **2020**, *32*, 6197.
- [56] J. Li, T. Inoshita, T. Ying, A. Ooishi, J. Kim, H. Hosono, *Adv. Mater.* **2020**, *32*, 2002945.
- [57] J. Duan, J. Xi, B. Jiao, J. Dai, Y. Zu, Z. Wu, *J. Mater. Chem. C* **2022**, *10*, 11323.
- [58] X. Niu, J. Xiao, B. Lou, Z. Yan, Q. Zhou, T. Lin, C. Ma, X. Han, *Ceram. Int.* **2022**, *48*, 30788.
- [59] Y. Ren, S. Lü, *Chem. Eng. J.* **2021**, *417*, 129223.
- [60] P. Yang, G. N. Liu, B. D. Liu, X. D. Liu, Y. B. Lou, J. X. Chen, Y. X. Zhao, *Chem. Commun.* **2018**, *54*, 11638.
- [61] H.-B. Zhao, J.-F. Liao, Y. Teng, H.-Y. Chen, D.-B. Kuang, *ACS Appl. Mater. Interfaces* **2022**, *14*, 43354.
- [62] S. Fang, H. Li, Y. Xie, H. Li, Y. Wang, Y. Shi, *Small* **2021**, *17*, 2103831.
- [63] H. Peng, X. Wang, Y. Tian, B. Zou, F. Yang, T. Huang, C. Peng, S. Yao, Z. Yu, Q. Yao, G. Rao, J. Wang, *ACS Appl. Mater. Interfaces* **2021**, *13*, 13443.

- [64] L. Lian, P. Zhang, G. Liang, S. Wang, X. Wang, Y. Wang, X. Zhang, J. Gao, D. Zhang, L. Gao, H. Song, R. Chen, X. Lan, W. Liang, G. Niu, J. Tang, J. Zhang, *ACS Appl. Mater. Interfaces* **2021**, *13*, 22749.
- [65] F. Zhang, Y. Zhou, Z. Chen, M. Wang, Z. Ma, X. Chen, M. Jia, D. Wu, J. Xiao, X. Li, Y. Zhang, Z. Shi, C. Shan, *Adv. Mater.* **2022**, *34*, 2204801.
- [66] L. Wang, H. Sun, C. Sun, D. Xu, J. Tao, T. Wei, Z. H. Zhang, Y. Zhang, Z. Wang, W. Bi, *Dalton Trans.* **2021**, *50*, 2766.
- [67] B. Su, J. Jin, K. Han, Z. Xia, *Adv. Funct. Mater.* **2023**, *33*, 2210735.
- [68] H. Peng, Y. Tian, X. Wang, T. Huang, Z. Yu, Y. Zhao, T. Dong, J. Wang, B. Zou, *ACS Appl. Mater. Interfaces* **2022**, *14*, 12395.
- [69] F. Liu, D. Mondal, K. Zhang, Y. Zhang, K. Huang, D. Wang, W. Yang, P. Mahadevan, R. Xie, *Mater. Adv.* **2021**, *2*, 3744.
- [70] I. W. Gilley, T. D. Creason, T. M. McWhorter, B. Saporov, *Adv. Photonics Res.* **2022**, *3*, 2200172.
- [71] X. Meng, S. Ji, Q. Wang, X. Wang, T. Bai, R. Zhang, B. Yang, Y. Li, Z. Shao, J. Jiang, K.-L. Han, F. Liu, *Adv. Sci.* **2022**, *9*, 2203596.
- [72] L. Lian, T. Zhang, H. Ding, P. Zhang, X. Zhang, Y.-B. Zhao, J. Gao, D. Zhang, Y. S. Zhao, J. Zhang, *ACS Materials Lett.* **2022**, *4*, 1446.
- [73] L. Y. Lian, X. Wang, P. Zhang, J. S. Zhu, X. W. Zhang, J. B. Gao, S. Wang, G. J. Liang, D. L. Zhang, L. Gao, H. S. Song, R. Chen, X. Z. Lan, W. X. Liang, G. D. Niu, J. Tang, J. B. Zhang, *J. Phys. Chem. Lett.* **2021**, *12*, 6919.
- [74] S. Li, J. Xu, Z. Li, Z. Zeng, W. Li, M. Cui, C. Qin, Y. Du, *Chem. Mater.* **2020**, *32*, 6525.
- [75] J. Huang, Y. Peng, J. Jin, M. S. Molokeev, X. Yang, Z. Xia, *J. Phys. Chem. Lett.* **2021**, *12*, 12345.
- [76] J. H. Wei, Y. W. Yu, J. B. Luo, Z. Z. Zhang, D. B. Kuang, *Adv. Optical Mater.* **2022**, *10*, 2200724.
- [77] A. Merker, M. Scholz, M. Morgenroth, T. Lenzer, K. Oum, *J. Phys. Chem. Lett.* **2021**, *12*, 2736.
- [78] X. Liu, F. Yuan, C. Zhu, J. Li, X. Lv, G. Xing, Q. Wei, G. Wang, J. Dai, H. Dong, J. Xu, B. Jiao, Z. Wu, *Nano Energy* **2022**, *91*, 106664.
- [79] Y. Yin, Y. Wang, Q. Sun, Y. Yang, Y. Wang, Z. Yang, W.-J. Yin, *J. Phys. Chem. Lett.* **2022**, *13*, 4177.
- [80] Z. Lan, J. Meng, K. Zheng, I. E. Castelli, *J. Phys. Chem. C* **2021**, *125*, 1592.
- [81] R. Lin, Q. Guo, Q. Zhu, Y. Zhu, W. Zheng, F. Huang, *Adv. Mater.* **2019**, *31*, 1905079.
- [82] R. Lin, Q. Zhu, Q. Guo, Y. Zhu, W. Zheng, F. Huang, *J. Phys. Chem. C* **2020**, *124*, 20469.
- [83] E. P. Booker, J. T. Griffiths, L. Eyre, C. Ducati, N. C. Greenham, N. J. L. K. Davis, *J. Phys. Chem. C* **2019**, *123*, 16951.
- [84] R. Li, R. Wang, Y. Yuan, J. Ding, Y. Cheng, Z. Zhang, W. Huang, *J. Phys. Chem. Lett.* **2021**, *12*, 317.
- [85] Z. Xing, Z. Zhou, G. Zhong, C. C. S. Chan, Y. Li, X. Zou, J. E. Halpert, H. Su, K. S. Wong, *Adv. Funct. Mater.* **2022**, *32*, 2207638.

This article is protected by copyright. All rights reserved.

- [86] D. Lee, S.-J. Lee, J. H. Kim, J. Park, Y.-C. Kang, M. Song, H. W. Lee, H. S. Kim, J. W. Choi, *Adv. Funct. Mater.* **2022**, *32*, 2202207.
- [87] X. Zheng, J. Huang, Y. Liu, T. Wang, S. Han, Z. Wang, B. Teng, S. Ji, *Adv. Photonics Res.* **2022**, *3*, 2100289.
- [88] Z. Ma, Z. Shi, C. Qin, M. Cui, D. Yang, X. Wang, L. Wang, X. Ji, X. Chen, J. Sun, D. Wu, Y. Zhang, X. J. Li, L. Zhang, C. Shan, *ACS Nano* **2020**, *14*, 4475.
- [89] Z. Li, Z. Li, Z. Shi, X. S. Fang, *Adv. Funct. Mater.* **2020**, *30*, 2002634.
- [90] B. Yang, L. Yin, G. Niu, J. H. Yuan, K. H. Xue, Z. Tan, X. S. Miao, M. Niu, X. Du, H. Song, E. Lifshitz, J. Tang, *Adv. Mater.* **2019**, *31*, 1904711.
- [91] H. Peng, S. Yao, Y. Guo, R. Zhi, X. Wang, F. Ge, Y. Tian, J. Wang, B. Zou, *J. Phys. Chem. Lett.* **2020**, *11*, 4703.
- [92] H. Peng, X. Wang, Y. Tian, T. Dong, Y. Xiao, T. Huang, Y. Guo, J. Wang, B. Zou, *J. Phys. Chem. Lett.* **2021**, *12*, 6639.
- [93] X. Liu, Y. Li, T. Liang, W. Liu, J. Fan, *J. Phys. Chem. Lett.* **2022**, *13*, 1373.
- [94] L. Lian, S. Wang, H. Ding, G. Liang, Y.-B. Zhao, H. Song, X. Lan, J. Gao, R. Chen, D. Zhang, J. Zhang, *Adv. Optical Mater.* **2021**, *10*, 2101640.
- [95] Z. Ma, X. Ji, M. Wang, F. Zhang, Z. Liu, D. Yang, M. Jia, X. Chen, D. Wu, Y. Zhang, X. Li, Z. Shi, C. Shan, *Adv. Sci.* **2022**, *9*, 2202408.
- [96] H. Chen, L. Zhu, C. Xue, P. Liu, X. Du, K. Wen, H. Zhang, L. Xu, C. Xiang, C. Lin, M. Qin, J. Zhang, T. Jiang, C. Yi, L. Cheng, C. Zhang, P. Yang, M. Niu, W. Xu, J. Lai, Y. Cao, J. Chang, H. Tian, Y. Jin, X. Lu, L. Jiang, N. Wang, W. Huang, J. Wang, *Nat. Commun.* **2021**, *12*, 1421.
- [97] X. Li, J. Chen, D. Yang, X. Chen, D. Geng, L. Jiang, Y. Wu, C. Meng, H. Zeng, *Nat. Commun.* **2021**, *12*, 3879.
- [98] C.-Y. Chen, Y.-I. Lin, P.-T. Lai, H.-C. Lin, G.-H. Tan, H.-W. Lin, R. D. Schaller, *Adv. Optical Mater.* **2022**, *10*, 2200005.
- [99] J. Lv, X. Lu, X. Li, M. Xu, J. Zhong, X. Zheng, Y. Shi, X. Zhang, Q. Zhang, *Small* **2022**, *18*, 2201715.
- [100] C.-X. Li, S.-B. Cho, D.-H. Kim, I.-K. Park, *Chem. Mater.* **2022**, *34*, 6921.
- [101] M. Zhang, J. Zhu, B. Yang, G. Niu, H. Wu, X. Zhao, L. Yin, T. Jin, X. Liang, J. Tang, *Nano Lett.* **2021**, *21*, 1392.
- [102] J. Ma, X. Xia, S. Yan, Y. Li, W. Liang, J. Yan, X. Chen, D. Wu, X. Li, Z. Shi, *ACS Appl. Mater. Interfaces* **2021**, *13*, 15409.
- [103] W. Liang, Z. Shi, Y. Li, J. Ma, S. Yin, X. Chen, D. Wu, Y. Tian, Y. Tian, Y. Zhang, X. Li, C. Shan, *ACS Appl. Mater. Interfaces* **2020**, *12*, 37363.
- [104] X. Liu, Y. Yu, F. Yuan, C. Zhao, H. Dong, B. Jiao, Z. Wu, *ACS Appl. Mater. Interfaces* **2020**, *12*, 52967.
- [105] T.-H. Le, S. Lee, H. Jo, M. Kim, J. Lee, M. Chang, H. Yoon, *ACS Appl. Nano Mater.* **2021**, *4*, 7621.

- [106] Y. Gu, X. Yao, H. Geng, G. Guan, M. Hu, M. Han, *ACS Appl. Mater. Interfaces* **2021**, *13*, 40798.
- [107] X. Xu, C. Fan, Z. Qi, S. Jiang, Q. Xiao, H. Liang, H. Duan, Q. Zhang, *ACS Appl. Nano Mater.* **2021**, *4*, 9625.
- [108] P. Vashishtha, T. J. N. Hooper, Y. Fang, D. Kathleen, D. Giovanni, M. Klein, T. C. Sum, S. G. Mhaisalkar, N. Mathews, T. White, *Nanoscale* **2021**, *13*, 59.
- [109] W. Q. Liang, Y. Li, J. L. Ma, Y. Wang, J. J. Yan, X. Chen, D. Wu, Y. T. Tian, X. J. Li, Z. F. Shi, *Nanoscale* **2020**, *12*, 17213.
- [110] Z. Zhou, Y. Li, Z. Xing, Z. Li, K. S. Wong, J. E. Halpert, *ACS Appl. Nano Mater* **2021**, *4*, 14188.
- [111] B. Wang, P. Li, Y. Zhou, Z. Deng, X. Ouyang, Q. Xu, *ACS Appl. Nano Mater.* **2022**, *5*, 9792.
- [112] Z. Jiang, H. Liu, J. Zou, Y. Huang, Z. Xu, C. Li, D. Liu, *ACS Appl. Mater. Interfaces* **2022**, *14*, 34937.
- [113] T. Li, J. Ma, X. Chen, J. Yan, M. Zhang, D. Wu, Y. Tian, X. Li, Z. Shi, *ACS Appl. Mater. Interfaces* **2021**, *13*, 49007.
- [114] W. Gao, G. Niu, L. Yin, B. Yang, J.-H. Yuan, D. Zhang, K.-H. Xue, X. Miao, Q. Hu, X. Du, J. Tang, *ACS Appl. Electron. Mater.* **2020**, *2*, 2242.
- [115] F. Zeng, Y. Guo, W. Hu, Y. Tan, X. Zhang, J. Feng, X. Tang, *ACS Appl. Mater. Interfaces* **2020**, *12*, 23094.
- [116] Y. Li, Z. Zhou, F. K. Sheong, Z. Xing, R. Lortz, K. S. Wong, H. H. Y. Sung, I. D. Williams, J. E. Halpert, *ACS Energy Lett.* **2021**, *6*, 4383.
- [117] X. Li, L. Zhang, Q. Zheng, Z. Zhou, S. He, D. Tian, A. Guo, C. Wang, S. Liu, X. Chu, C. Yang, F. Zhao, *ACS Appl. Nano Mater.* **2022**, *5*, 917.
- [118] X. Zhao, Y. Tao, J. Dong, Y. Fang, X. Song, Z. Yan, *ACS Appl. Mater. Interfaces* **2022**, *14*, 43490.
- [119] Q. Li, Z. Chen, B. Yang, L. Tan, B. Xu, J. Han, Y. Zhao, J. Tang, Z. Quan, *J. Am. Chem. Soc.* **2020**, *142*, 1786.
- [120] Y. Huang, C. Liang, D. Wu, Q. Chang, L. Liu, H. Liu, X. Tang, Y. He, J. Qiu, *J. Phys. Chem. Lett.* **2021**, *12*, 3401.
- [121] X. Zhao, G. Niu, J. Zhu, B. Yang, J.-H. Yuan, S. Li, W. Gao, Q. Hu, L. Yin, K.-H. J. T. Xue, *J. Phys. Chem. Lett.* **2020**, *11*, 1873.
- [122] B. Q. Wang, C. Chen, X. Yang, W. S. Cai, S. Y. Zhao, R. Li, W. Ma, J. Z. Chen, Z. G. Zang, *EcoMat* **2022**, *4*, 12184.
- [123] Q. Wei, T. Chang, R. Zeng, S. Cao, J. Zhao, X. Han, L. Wang, B. Zou, *J. Phys. Chem. Lett.* **2021**, *12*, 7091.
- [124] X. Xing, T. Tong, M. Mohebinia, D. Wang, Z. Ren, V. G. Hadjiev, Z. Wang, J. Bao, *J. Phys. Chem. Lett.* **2022**, *13*, 6447.
- [125] S.-S. Yan, Y.-C. Kong, Z.-H. Zhang, Z.-S. Wu, Z.-D. Lian, Y.-P. Zhao, S.-C. Su, L. Li, S.-P. Wang, K. W. Ng, *ACS Appl. Mater. Interfaces* **2022**, *14*, 49975.

This article is protected by copyright. All rights reserved.

- [126] X. M. Mo, T. Li, F. C. Huang, Z. X. Li, Y. L. Zhou, T. Lin, Y. F. Ouyang, X. M. Tao, C. F. Pan, *Nano Energy* **2021**, *81*, 105570.
- [127] Z. Li, C. Zuo, X. Liu, Z. Ma, Z. Shi, X. S. Fang, *Adv. Optical Mater.* **2022**, *10*, 2102315.
- [128] Y. Shi, D. Liang, Q. Mo, S. Lu, Z. Sun, H. Xiao, Q. Qian, Z. Zang, *Chem. Commun.* **2023**, *59*, 583.
- [129] Q. Yao, J. Li, X. Li, X. Zheng, Z. Wang, X. Tao, *Adv. Optical Mater.* **2022**, *10*, 2201161.
- [130] W. R. Gao, L. X. Yin, J. H. Yuan, K. H. Xue, G. D. Niu, B. Yang, Q. S. Hu, X. X. Liu, J. Tang, *Org. Electron.* **2020**, *86*, 105903.
- [131] D. Shen, X. Wang, X. Zhang, Y. Liu, Y. Shi, X. Li, X. Chen, Y. Zhang, *ACS Appl. Opt. Mater.* **2023**, *1*, 435.
- [132] B. Wang, Y. Tang, X. Yang, W. Cai, R. Li, W. Ma, S. Zhao, C. Chen, Z. Zang, *Nano Mater. Sci.* **2022**, doi: 10.1016/j.nanoms.2022.03.003.
- [133] X. Xu, S. Jiang, C. Fan, Q. Deng, L. Shen, Q. Zhang, *Adv. Optical Mater.* **2022**, *10*, 2201107.
- [134] Y. Li, J. Ma, W. Liang, Y. Tian, X. Li, D. Wu, Z. Shi, X. S. Fang, *Chem. Eng. J.* **2023**, *451*, 138531.
- [135] Y. Lu, G. Li, S. Fu, S. Fang, L. Li, *ACS Omega* **2021**, *6*, 544.
- [136] F. Zhang, W. Liang, L. Wang, Z. Ma, X. Ji, M. Wang, Y. Wang, X. Chen, D. Wu, X. Li, Y. Zhang, C. Shan, Z. Shi, *Adv. Funct. Mater.* **2021**, *31*, 2105771.
- [137] F. Gao, X. Zhu, Q. Feng, W. Zhong, W. Liu, H. Xu, Y. Liu, *Nano Energy* **2022**, *98*, 107270.
- [138] P. Vashishtha, G. V. Nutan, B. E. Griffith, Y. Fang, D. Giovanni, M. Jagadeeswararao, T. C. Sum, N. Mathews, S. G. Mhaisalkar, J. V. Hanna, T. White, *Chem. Mater.* **2019**, *31*, 9003.
- [139] P. Cheng, L. Sun, L. Feng, S. Yang, Y. Yang, D. Zheng, Y. Zhao, Y. Sang, R. Zhang, D. Wei, W. Deng, K. Han, *Angew. Chem., Int. Ed.* **2019**, *58*, 16087.
- [140] L. Wang, Z. Shi, Z. Ma, D. Yang, F. Zhang, X. Ji, M. Wang, X. Chen, G. Na, S. Chen, D. Wu, Y. Zhang, X. Li, L. Zhang, C. Shan, *Nano Lett.* **2020**, *20*, 3568.
- [141] S. Zhao, C. Chen, W. Cai, R. Li, H. Li, S. Jiang, M. Liu, Z. Zang, *Adv. Optical Mater.* **2021**, *9*, 2100307.
- [142] S. Chen, X. Mao, Q. Zhong, Q. Pan, J. Liu, J. Fu, D. Yang, J. Chen, L. Wang, Q. Zhang, M. Cao, *Adv. Optical Mater.* **2022**, *10*, 2200687.
- [143] X. Hu, P. Yan, P. Ran, L. Lu, J. Leng, Y. M. Yang, X. Li, *J. Phys. Chem. Lett.* **2022**, *13*, 2862.
- [144] X. Hu, Y. Li, Y. Wu, W. Chen, H. Zeng, X. Li, *Mater. Chem. Front.* **2021**, *5*, 6152.
- [145] Z. Luo, Q. Li, L. Zhang, X. Wu, L. Tan, C. Zou, Y. Liu, Z. Quan, *Small* **2020**, *16*, 1905226.
- [146] Y. Li, P. Vashishtha, Z. Zhou, Z. Li, S. B. Shivarudraiah, C. Ma, J. Liu, K. S. Wong, H. Su, J. E. Halpert, *Chem. Mater.* **2020**, *32*, 5515.
- [147] Y.-H. Cheng, R. Suzuki, N. Shinotsuka, H. Ebe, N. Oshita, R. Yamakado, T. Chiba, A. Masuhara, J. Kido, *Sci. Rep.* **2022**, *12*, 4620.
- [148] Y. Lu, S. Fang, G. Li, L. Li, *J. Alloy. Compd.* **2022**, *903*, 163924.

This article is protected by copyright. All rights reserved.

- [149] Y. Lee, J.-H. Cha, H. Kim, J. Y. Lee, M. W. Lee, H. S. Jang, D.-Y. Jung, *ACS Appl. Nano Mater.* **2022**, *5*, 18409.
- [150] J. E. Zhou, K. An, P. He, J. Yang, C. Zhou, Y. Luo, W. Kang, W. Hu, P. Feng, M. Zhou, X. S. Tang, *Adv. Optical Mater.* **2021**, *9*, 2002144.
- [151] G. Seo, H. Jung, T. D. Creason, V. Yeddu, M. Bamidele, E. Echeverria, J. Lee, D. McIlroy, B. Saparov, D. Y. Kim, *ACS Energy Lett.* **2021**, *6*, 2584.
- [152] S. Liu, H. Liu, G. Zhou, X. Li, S. Wang, *Chem. Eng. J.* **2022**, *427*, 131430.
- [153] L. Lian, M. Zheng, W. Zhang, L. Yin, X. Du, P. Zhang, X. Zhang, J. Gao, D. Zhang, L. Gao, G. Niu, H. Song, R. Chen, X. Lan, J. Tang, J. Zhang, *Adv. Sci.* **2020**, *7*, 2000195.
- [154] Z. Ma, S. Lin, X. Ji, X. Chen, D. Wu, Z. Shi, *J. Alloy. Compd.* **2023**, *930*, 167462.
- [155] N. Li, Y. Xiao, Y. Liu, Z. Yang, S. Liu, *Adv. Optical Mater.* **2022**, *10*, 2102232.
- [156] F. Zeng, Y. Guo, W. Hu, Y. Tan, X. Zhang, J. Yang, Q. Lin, Y. Peng, X. Tang, Z. Liu, Z. Yao, J. Du, *J. Lumin.* **2020**, *223*, 117178.
- [157] X. Zhou, L. Zhang, Y. Huang, Z. Zhou, W. Xing, J. Zhang, F. Zhou, D. Zhang, F. Zhao, *Adv. Optical Mater.* **2021**, *9*, 2100889.
- [158] T. Jun, T. Handa, K. Sim, S. Iimura, M. Sasase, J. Kim, Y. Kanemitsu, H. Hosono, *APL Mater.* **2019**, *7*, 111113.
- [159] Q. Liu, Y. He, J. Yan, Z. Chen, C. Zhao, H. Zhou, *J. Alloy. Compd.* **2023**, *933*, 167606.
- [160] J. Yang, W. Kang, Z. Liu, M. Pi, L. B. Luo, C. Li, H. Lin, Z. Luo, J. Du, M. Zhou, X. Tang, *J. Phys. Chem. Lett.* **2020**, *11*, 6880.
- [161] M. Li, C. Cao, W. Liu, N. Wang, C. Yi, R. Li, J. Wang, *J. Phys. Chem. Lett.* **2022**, *13*, 6462.
- [162] X. Zhao, A. Luo, Z. Lin, X. Zhong, Z. Zhu, Q. Lin, H. Su, *J. Alloy. Compd.* **2023**, *253*, 119434.
- [163] X. Wu, G. Liang, S. Wang, Y. Wang, H. Song, Z. Li, R. Zeng, Q. Hu, *ACS Appl. Electron. Mater.* **2022**, *4*, 3583.
- [164] Y. Gu, X. Yao, H. Geng, M. Long, G. Guan, M. Hu, M. Han, *ACS Appl. Electron. Mater.* **2022**, *4*, 663.
- [165] N. Liu, X. Zhao, M. Xia, G. Niu, Q. Guo, L. Gao, J. Tang, *J. Semicond.* **2020**, *41*, 052204.
- [166] X. Li, L. Zhang, X. Zhou, C. Wang, Z. Zhou, S. He, D. Tian, Z. Ren, C. Yang, F. Zhao, *Opt. Lett.* **2021**, *46*, 4252.
- [167] F. Zeng, Y. Tan, W. Hu, X. Tang, Z. Luo, Q. Huang, Y. Guo, X. Zhang, H. Yin, J. Feng, X. Zhao, B. Yang, *J. Phys. Chem. Lett.* **2021**, *12*, 1973.
- [168] X. Ji, Z. Ma, X. Chen, D. Wu, Y. Tian, Z. Shi, *J. Phys. Photonics* **2022**, *4*, 014001.
- [169] S. He, L. Zhang, D. Tian, Z. Zhou, A. Guo, B. Xia, Y. Zhu, F. Zhao, *J. Alloy. Compd.* **2023**, *937*, 168538.

- [170] C. Wang, F. Zhao, Z. Zhou, X. Li, S. He, M. Zhang, D. Zhang, L. Zhang, *J. Alloy. Compd.* **2022**, *905*, 164245.
- [171] R. Fan, S. Fang, C. Liang, Z. Liang, H. Zhong, *Photon. Res.* **2021**, *9*, 694.
- [172] L. Xie, B. Chen, F. Zhang, Z. Zhao, X. Wang, L. Shi, Y. Liu, L. Huang, R. Liu, B. Zou, Y. Wang, *Photon. Res.* **2020**, *8*, 768.
- [173] S. Zhao, Q. Mo, W. Cai, H. Wang, Z. Zang, *Photon. Res.* **2021**, *9*, 187.
- [174] Z. Wang, J. Guo, Q.-S. Lin, G. Rao, J. Zhao, C. Yang, W. He, C. Wang, Z. Zhang, *Adv. Optical Mater.* **2022**, 2202059.
- [175] X. Zhao, T. Jin, W. R. Gao, G. D. Niu, J. S. Zhu, B. X. Song, J. J. Luo, W. C. Pan, H. D. Wu, M. Y. Zhang, X. He, L. C. Fu, Z. G. Li, H. T. Zhao, J. Tang, *Adv. Optical Mater.* **2021**, *9*, 2101194.
- [176] S. Cheng, M. Nikl, A. Beitlerova, R. Kucerkova, X. Du, G. Niu, Y. Jia, J. Tang, G. Ren, Y. Wu, *Adv. Optical Mater.* **2021**, *9*, 2100460.
- [177] L. Y. Lian, M. Y. Zheng, P. Zhang, Z. Zheng, K. Du, W. Lei, J. B. Gao, G. D. Niu, D. L. Zhang, T. Y. Zhai, S. Y. Jin, J. Tang, X. W. Zhang, J. B. Zhang, *Chem. Mater.* **2020**, *32*, 3462.
- [178] X. Zhang, B. Zhou, X. Chen, W. W. Yu, *Inorg. Chem.* **2022**, *61*, 399.
- [179] P. Xiang, Q. Wei, C. Wang, P. Cai, Y. Tong, G. Tang, X. Sun, F. Yang, H. Shi, Z. Liu, L. Qin, *J. Mater. Chem. C* **2022**, *10*, 15400.
- [180] Y. Li, Z. Shi, W. Liang, L. Wang, S. Li, F. Zhang, Z. Ma, Y. Wang, Y. Tian, D. Wu, X. Li, Y. Zhang, C. Shan, X. S. Fang, *Mater. Horiz.* **2020**, *7*, 530.
- [181] C. Zou, Q. Liu, K. Chen, F. Chen, Z. Zhao, Y. Cao, C. Deng, X. Wang, X. Li, S. Zhan, F. Gao, S. Li, *Mater. Horiz.* **2022**, *9*, 1479.
- [182] Y. Li, Z. Shi, L. Wang, Y. Chen, W. Liang, D. Wu, X. Li, Y. Zhang, C. Shan, X. S. Fang, *Mater. Horiz.* **2020**, *7*, 1613.
- [183] F. Sun, T. Liu, P. Ran, X. Chen, T. Jiang, W. Shen, X. Liu, Y. Yang, *J. Phys. Chem. Lett.* **2022**, *13*, 3431.
- [184] G. K. Grandhi, N. S. M. Viswanath, H. B. Cho, J. H. Han, S. M. Kim, S. Choi, W. B. Im, *J. Phys. Chem. Lett.* **2020**, *11*, 7723.
- [185] R. Kentsch, M. Morgenroth, M. Scholz, K. Xu, J. S. Günne, T. Lenzer, K. Oum, *J. Phys. Chem. Lett.* **2020**, *11*, 4286.
- [186] Y. Hu, X. Yan, L. Zhou, P. Chen, Q. Pang, Y. Chen, *J. Phys. Chem. Lett.* **2022**, *13*, 10786.
- [187] Y.-K. Jung, S. Kim, Y. C. Kim, A. Walsh, *J. Phys. Chem. Lett.* **2021**, *12*, 8447.
- [188] W. Bai, S. Shi, T. Lin, T. Zhou, T. Xuan, R.-J. Xie, *Adv. Photonics Res.* **2021**, *2*, 2000158.
- [189] D. Yuan, *ACS Appl. Mater. Interfaces* **2020**, *12*, 38333.
- [190] S. Cheng, A. Beitlerova, R. Kucerkova, E. Mihokova, M. Nikl, Z. Zhou, G. Ren, Y. Wu, *ACS Appl. Mater. Interfaces* **2021**, *13*, 12198.

- [191] S. Li, F. Weng, P. Yang, X. Li, X. Cheng, L. Zhang, H. Wang, W. Zhang, Z. Zhang, K. Yang, *J. Alloy. Compd.* **2023**, 932, 167590.
- [192] H. Chen, J. M. Pina, F. Yuan, A. Johnston, D. Ma, B. Chen, Z. Li, A. Dumont, X. Li, Y. Liu, S. Hoogland, Z. Zajacz, Z. Lu, E. H. Sargent, *J. Phys. Chem. Lett.* **2020**, 11, 4326.
- [193] S. Liu, Y. Yue, X. Zhang, C. Wang, G. Yang, D. Zhu, *J. Mater. Chem. C* **2020**, 8, 8374.
- [194] R. Zhang, X. Mao, D. Zheng, Y. Yang, S. Yang, K. Han, *Laser Photonics Rev.* **2020**, 14, 2000027.
- [195] L. Wang, Z. Ma, F. Zhang, M. Wang, X. Chen, D. Wu, Y. Tian, X. Li, Z. Shi, *J. Mater. Chem. C* **2021**, 9, 6151.
- [196] J. M. Yang, Y. K. Jung, J. H. Lee, Y. C. Kim, S. Y. Kim, S. Seo, D. A. Park, J. H. Kim, S. Y. Jeong, I. T. Han, J. H. Park, A. Walsh, N. G. Park, *Nanoscale Horiz.* **2021**, 6, 987.
- [197] S. Li, Z. Shi, F. Zhang, L. Wang, Z. Ma, D. Yang, Z. Yao, D. Wu, T. Xu, Y. Tian, Y. Zhang, C. Shan, X. Li, *Chem. Mater.* **2019**, 31, 3917.
- [198] L. Manna, O. Bakr, S. Brovelli, H. Li, *Energy Mater. Adv.* **2022**, 2022, 9865891.
- [199] Y. Liu, M. Molokeev, Z. Xia, *Energy Mater. Adv.* **2021**, 2021, 2585274.
- [200] X. Huang, Q. Sun, B. Devakumar, *Mater. Today Chem.* **2020**, 17, 100288.
- [201] T. Jiang, J. Wang, L. Xie, C. Bai, M. Wang, Y. Wu, F. Zhang, Y. Zhao, B. Chen, Y. Wang, *ACS Appl. Nano Mater.* **2022**, 5, 508.
- [202] Q. Chang, D. Wu, Y. Huang, C. Liang, L. Liu, H. Liu, Y. He, Q. Huang, J. Qiu, X. Tang, *Sens. Actuators B: Chem.* **2022**, 367, 132112.
- [203] S. Fang, Y. Wang, H. Li, F. Fang, K. Jiang, Z. Liu, H. Li, Y. Shi, *J. Mater. Chem. C* **2020**, 8, 4895.
- [204] H. Zhang, L. Yang, H. Chen, W. Ma, R. Wang, G. Cao, *Mater. Chem. Front.* **2022**, 6, 1647.
- [205] Z. Zhao, X. Li, L. Xie, B. Chen, T. Jiang, J. Cao, F. Zhang, M. Wang, Y. Wu, H. Zheng, F. Zhang, Y. Wang, *J. Alloy. Compd.* **2022**, 241, 118482.
- [206] L. Xie, B. Chen, F. Zhang, Z. Zhao, T. Jiang, M. Wang, Y. Wu, L. Huang, W. Song, Y. Liu, Y. Wang, *J. Alloy. Compd.* **2021**, 239, 118333.
- [207] J. Qu, S. Xu, Y. Cui, C. Wang, *Chem. Eur. J.* **2022**, 28, e202200877.
- [208] Q. Wang, M. Nikl, S. Cheng, G. Ren, Y. Wu, *Phys. Status Solidi RRL* **2021**, 15, 2100422.
- [209] P. Du, L. Luo, W. Cheng, *J. Am. Ceram. Soc.* **2020**, 103, 1149.
- [210] Q. Wang, Q. Zhou, M. Nikl, J. W. Xiao, R. Kucerkova, A. Beitlerova, V. Babin, P. Prusa, V. Linhart, J. K. Wang, X. M. Wen, G. D. Niu, J. Tang, G. H. Ren, Y. T. Wu, *Adv. Optical Mater.* **2022**, 10, 2200304.
- [211] W. Fan, L. Xu, Z. Yang, Y. Liu, J. Song, *J. Mater. Chem. C* **2022**, doi: 10.1039/d2tc04057c.
- [212] X. Zhou, C. Wang, J. Luo, L. Zhang, F. Zhao, Q. Ke, *Chem. Eng. J.* **2022**, 450, 136364.
- [213] F. Huang, X. Mo, X. Li, M. Peng, Y. Zhou, X. Tao, Y. Ouyang, J. Zhao, *J. Lumin.* **2022**, 253, 119390.
- [214] J. Hui, P. Ran, Y. Su, L. Yang, X. Xu, T. Liu, Y. Yang, *J. Phys. Chem. C* **2022**, 126, 12882.

This article is protected by copyright. All rights reserved.

- [215] Z. X. Zhang, C. Li, Y. Lu, X. W. Tong, F. X. Liang, X. Y. Zhao, D. Wu, C. Xie, L. B. Luo, *J. Phys. Chem. Lett.* **2019**, *10*, 5343.
- [216] Y. Gu, X. Yao, M. Long, H. Geng, M. Hu, *Mater. Lett.* **2022**, *323*, 132607.
- [217] B. Wang, Y. Liu, Z. Deng, P. Li, W. Wang, X. Ouyang, Q. Xu, *Physica. B* **2022**, *633*, 413788.
- [218] Q. Zhou, J. Ren, J. Xiao, L. Lei, F. Liao, H. Di, C. Wang, L. Yang, Q. Chen, X. Yang, Y. Zhao, X. Han, *Nanoscale* **2021**, *13*, 19894.
- [219] W. Liang, L. Wang, Y. Li, F. Zhang, X. Chen, D. Wu, Y. Tian, X. Li, C. Shan, Z. Shi, *Mater Today Phys.* **2021**, *18*, 100398.
- [220] R. Duan, Z. Chen, D. Xiang, J. Si, X. Liu, *J. Lumin.* **2023**, *253*, 119482.
- [221] R. Lin, Y. Ding, W. Zheng, M. Jin, L. Chen, X. Ouyang, F. Huang, *Cell Reports Phys. Sci.* **2021**, *2*, 100437.
- [222] N. He, F. Ye, J. Liu, T. Sun, X. Wang, W. Hou, W. Shao, X. Wan, Y. Tong, F. Xu, Y. Sheng, *Adv. Electron. Mater.* **2022**, 2201038.
- [223] T. Li, X. Mo, C. Peng, Q. Lu, C. Qi, X. Tao, Y. Ouyang, Y. Zhou, *Chem. Commun.* **2019**, *55*, 4554.
- [224] Y. Liang, C. Xie, C.-Y. Dong, X.-W. Tong, W.-H. Yang, C.-Y. Wu, L.-B. Luo, *J. Mater. Chem. C* **2021**, *9*, 14897.
- [225] F. Huang, S. Ge, R. Wei, J. He, X. Ma, J. Tao, Q. Lu, X. Mo, C. Wang, C. Pan, *ACS Appl. Mater. Interfaces* **2022**, *14*, 43474.
- [226] H. Guo, Q. Zhao, P. Ran, J. Chen, Y. Zhu, Q. Jiang, Y. Tang, Z. Zhang, L. Song, C. Xu, S. Luo, Z. Shi, *Adv. Photonics Res.* **2022**, *3*, 2200197.
- [227] Y. Zhang, Y. He, Z. Tang, W. Yu, Z. Zhang, Z. Chen, L. Xiao, J.-J. Shi, S. Wang, B. Qu, *Small* **2022**, *18*, 2107161.
- [228] K. J. Kwak, J. H. Baek, D. E. Lee, I. H. Im, J. Kim, S. J. Kim, Y. J. Lee, J. Y. Kim, H. W. Jang, *Nano Lett.* **2022**, *22*, 6010.
- [229] Z. Shi, Y. Li, Y. Zhang, Y. Chen, X. Li, D. Wu, T. Xu, C. Shan, G. Du, *Nano Lett.* **2017**, *17*, 313.
- [230] Y. Zhou, X. Wang, T. He, H. Yang, C. Yang, B. Shao, L. Gutiérrez-Arzaluz, O. M. Bakr, Y. Zhang, O. F. Mohammed, *ACS Energy Lett.* **2022**, *7*, 844.
- [231] L. Gao, Q. Li, J. L. Sun, Q. Yan, *J. Phys. Chem. Lett.* **2023**, *14*, 1165.
- [232] Y. Li, Z. Zhou, F. K. Sheong, Z. Xing, K. S. Wong, H. H. Sung, I. D. Williams, J. E. Halpert, *Chem. Mater.* **2023**, *35*, 1318.
- [233] Z. Gao, C. Xu, H. Chen, Y. Tang, P. Lyu, L. Sun, *ACS Appl. Opt. Mater.* **2023**, *1*, 481.
- [234] Z. Yang, T. Wang, X. Xu, J. Yao, L. Xu, S. Wang, Y. Xu, J. Song, *J. Phys. Chem. Lett.* **2023**, *14*, 326.



Zhuangzhuang Ma received his bachelor degree in physics from Zaozhuang University in 2017. Presently, he is pursuing his Ph.D. under the supervision of Prof. Zhifeng Shi at School of Physics and Microelectronics, Zhengzhou University. His current research focuses on lead-free halide perovskite materials and their optoelectronic applications in light-emitting diodes.



Zhifeng Shi is currently a professor in School of Physics and Microelectronics, Zhengzhou University. He received his Ph.D. degree in Microelectronics and Solid-State Electronics at Jilin University in 2015. His scientific research concentrates on the synthesis and photophysics of semiconductor materials and their applications in optoelectronic devices. He has published over 90 peer-reviewed papers with more than 6000 citations. He was awarded the Youth Science and Technology Award of Henan Province and was selected into the National Young Talents Program.



This article is protected by copyright. All rights reserved.

Xiaosheng Fang received his Ph.D. degree from the Institute of Solid State Physics, Chinese Academy of Sciences, in 2006 under the supervision of Professor Lide Zhang. He worked as a Japan Society for the Promotion of Science (JSPS) postdoctoral fellow at the National Institute for Materials Science (NIMS), Japan, and then as an ICYS researcher within NIMS during 2006-2010. In 2010, he joined the Department of Materials Science, Fudan University as professor. His current research interests focus on semiconductors and the optoelectronic applications, especially on high performance photodetectors/phototransistors.

Ternary copper halides (TCHs) have generated considerable attention for the exceptional structure diversity and fascinating optoelectronic properties. The recent advances of currently explored TCHs are systemically summarized, regarding the crystal and electronic structure, synthesis strategy, photophysical mechanism, luminescence regulation, environmental stability, and their emerging applications. Moreover, current existing challenges and possible development directions are proposed for their further development.

Keyword

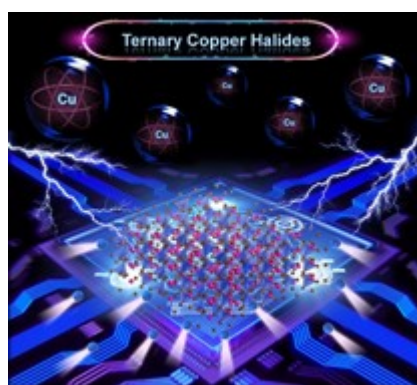
ternary copper halides, lead-free perovskites, optoelectronic properties, stability

Title

Recent Advances and Opportunities of Eco-Friendly Ternary Copper Halides: A New Superstar in Optoelectronic Applications

Z. Z. Ma, X. Z. Ji, S. L. Lin, X. Chen, D. Wu, X. J. Li, Y. Zhang, C. X. Shan, Z. F. Shi*, and X. S Fang*

ToC figure



This article is protected by copyright. All rights reserved.